Inelastic Scattering Dynamics of Ammonia with Small Molecules

Cassandra Amelia Rusher

Submitted for the degree of Doctor of Philosophy

Heriot-Watt University

Institute of Chemical Sciences

School of Engineering and Physical Sciences

September 2016

Abstract

Crossed molecular beam velocity map imaging (VMI) is employed to state-selectively record the NH_3 inelastic scattering products from collisions with a series of colliders; atomic Ar, diatomic D_2, and the polyatomics CH_4, C_2H_6 and $C(CH_3)_4$.

The differential cross sections (DCSs) presented for NH_3-Ar expand on the existing literature. The angular distribution of the scattering is found to exhibit a dependence on the angular momentum projection quantum number (k) of the NH_3 product state in addition to the known dependency on the total angular momentum quantum number (J). It is found that for increasing k the total scattering into sideways and backwards angles ($\theta \geq 60°$) decreases.

For the smallest molecular colliders D_2 and CH_4 co-excitation is observed. DCSs are presented for each NH_3 product state and evidence of separate D_2 co-excitation channels is obtained by a new extraction method for acquiring multiple DCSs from a single VMI image. The promotion of D_2 into the $J_{\mathrm{D_2}} = 3$ rotational level exhibits an unusual propensity for excitation at larger impact parameters. It is proposed that this is due to interactions at larger distances with attractive regions of the potential energy surface (PES), at smaller impact parameters the steeper gradient of the PES inhibits co-excitation.

The DCSs of NH_3 scattering with methane, ethane and neopentane exhibit a striking similarity across all three systems and when comparing individual NH_3 product states from a single collider. The DCSs are all dominated by forwards scattering angles ($\theta \leq 60°$) for all NH_3 collisional excitations. The dominant mechanism suggested is a "tug-of-war" type trajectory, however calculations are required for confirmation of this interaction.

Acknowledgements

There are many people who have supported me through my PhD. Firstly, I would like to thank my supervisor Stuart Greaves for all his help and support and for putting up with the sarcasm that occasionally cropped up these last 4 years, this would not have been possible without him. I would also like to thank him for the privilege of being his first PhD student, I think we've both learnt a lot along the way.

Recognition must go to David Hadden for the endless hours of discussion and analysis of current sporting events while running these experiments. His help has also been invaluable in developing the LabView programs used and designing new elements of the apparatus. The rest of the Spectroscopy and Dynamics group also have my appreciation for their helpful discussions and input throughout the last 4 years. They also have my thanks for the less helpful conversations that have made working within this group so enjoyable.

Thomas Sharples in particular has my thanks for all his help in the time prior to the Greaves' group expansion to more than 2 people in Edinburgh. As do Matthew Costen and Dave Townsend for letting me alter and use their photodissociation apparatus in the first year of my degree. Credit must also go to Aisling Stewart who helped in collecting the NH_3-D_2 data during her MChem project.

Acknowledgments must also go to Ondrej Tkáč and Andrew Orr-Ewing for hosting me at the University of Bristol on several occasions prior to the experimental apparatus moving to Edinburgh. I would also like to thank the EPSRC for my studentship which was funded under grant number EP/J002534.

Finally I'd like to thank my parents and family for their support and my partner for his never-ending confidence in me and dealing with a 400 mile commute.

Table of Contents

Table of Figures

Chapter 1 – Introduction

1.1 Reaction dynamics

Molecular and atomic collisions are occurring constantly; in the atmosphere, within a mug of tea or at the interface of a surface with its environment, such as skin to air. Collisions and the nature of the transfer of energy that occurs during them have been of interest to scientists, particularly chemists, since the early part of the 20th century as they are the fundamentals that underpin chemical reactions. Reaction dynamics attempts to describe the physical processes of individual collisions and any resultant chemical events[1] and to understand the underlying mechanisms of these events. In order to achieve this, a close relationship between theoretical techniques and experimental methods has developed. Beyond the very simple examples given, collisions are important, even those that do not result in an alteration to the chemical bonds. Thermal equilibrium is maintained through energy exchange during multiple collisions in both gas and liquid phases. This transfer of energy causes rotational and vibrational excitation into a distribution of quantum states, which in turn results in detectable characteristics such as the broadening of rotational and vibrational spectral lines.

Collisions are governed by the laws of conservation - conservation of energy and conservation of momentum. They are then categorized depending on how the conservation of energy law is adhered to. This can be observed in the nature of the products when compared to the parent molecules. Elastic collisions result in products that conserve the total kinetic energy (KE) of the colliders. They allow for a change in direction from the initial trajectory of the particle, providing the conservation of KE criterion is satisfied. For a collision defined as inelastic, it is the total energy (KE and internal energy) of the system that must be conserved, this allows for the initial KE to be dissipated into internal modes and exchanged between the colliding particles. The law governing conservation of momentum still applies to inelastic collisions. Inelastic collision, as a description, also includes any change in the chemical bonds of the molecule, although in situations where this occurs it is described as a reactive collision to differentiate from those that result only in a change of energy distribution. The focus of this thesis is inelastic scattering where the chemical identities of the molecules remain unaltered. More specifically the collisions of interest to this work are those that result in transfer of energy from translational motion into rotational excitation energy.

1.1.1 The Potential Energy Surface

Collisions can typically be described in terms of motion on a potential energy surface (PES) which can be determined from theoretical calculations using the characteristics of the system. This is a multidimensional function that maps the potential energy of the molecule depending on its geometry. Typically a single PES describes each electronic state of the molecule in relation to the evolving positions of the nuclei of the molecules and the nuclear-nuclear, electronic-nuclear and the electronic-electronic forces experienced. The energy of two atoms in a diatomic, and how it varies as they interact, can be depicted as a 1-D surface with relative ease. The potential energy of the molecule is described by plotting the distance between the nuclei against the nuclear-nuclear repulsion and the other electronic and nuclear interactions. These forces then appear as the peaks and troughs of the PES due to the changing attractive and repulsive nature of the interactions. This treatment of the system depends upon the Born-Oppenheimer approximation[2] which assumes that the nuclear motion of a molecule, i.e. vibrations (Ψ_{vib}) and rotations (Ψ_{rot}), can be treated separately to the electronic motion (Ψ_{ee}), resulting in the following molecular wavefunction:

$$\Psi_{\mathrm{total}} = \Psi_{\mathrm{ee}} \cdot \Psi_{\mathrm{vib}} \cdot \Psi_{\mathrm{rot}} \tag{1.1}$$

The nuclear motion is many orders of magnitude slower than the motion of the electron, as this is directly related to the mass of these particles. The difference is so great that nuclei can be considered stationary relative to any electronic motion and likewise the displacement of the electrons can be considered instantaneous compared to nuclear motion.

The Hamiltonian, ($\hat{H}$),[3, 4] describing the system includes a number of terms that define the intra-molecular interactions. These terms are for the kinetic energy of the nuclei, $\hat{T}_N$ and electrons, $\hat{T}_e$, and the Coulombic interactions, which include electron-electron, $\hat{V}_{ee}$, nuclei-nuclei, $\hat{V}_{NN}$ and electron-nuclei, $\hat{V}_{eN}$, potential energy terms:

$$\hat{H} = \hat{T}_N(R) + \hat{T}_e(r) + \hat{V}_{ee}(r) + \hat{V}_{NN}(R) + \hat{V}_{eN}(R,r) \tag{1.2}$$

where R and r are the nuclear and electronic displacement respectively. This Hamiltonian is therefore related to the molecular wavefunction, Ψ and its associated energy, E, via the time-independent Schrödinger equation:

$$\hat{H}\Psi(R;r) = E\Psi(R;r) \qquad 1.3$$

As the nuclear and electronic components are separable under the Born-Oppenheimer approximation, individual wavefunctions can be used to separately describe nuclear and electronic contributions to the molecular wavefunction that is used to approximate a solution to the Schrödinger equation for the system. As described above, nuclear motion is much slower than that of the electrons, resulting in the change in $\hat{T}_N$ being minimal between the geometries modelled to such an extent that under adiabatic conditions, it can be treated as a perturbation. Hence for fixed nuclear coordinates, the electronic Hamiltonian, $\hat{H}_e$, is;

$$\boldsymbol{\hat{H}_e(R;r) = \hat{T}_e(r) + \hat{V}_{ee}(r) + \hat{V}_{eN}(R,r)} \qquad 1.4$$

and its relationship to the molecular Hamiltonianis:

$$\boldsymbol{\hat{H} = \hat{T}_N(R) + \hat{H}_e(R;r)} \qquad 1.5$$

Therefore the electronic time-independent Schrödinger equation can be defined as

$$\hat{H}_e\Psi_i(R;r) = E_i\Psi_i(R;r) \qquad 1.6$$

in order to find the eigenfunctions of the electronic Hamiltonian. The PES derives from the solution of equation 1.6 for fixed nuclear coordinates of a molecule. The electronic energy will vary across multiple sets of nuclear coordinates. Achieving this is done using *ab initio* methods to calculate approximate solutions.

An interaction of such apparent simplicity as H + H_2 can also be described with a contour plot although in order to visualise a PES for a system of more than two atoms, it is necessary to produce only a two dimensional PES because this is the maximum that can be visualised on a 3-D graph despite the actual dimensionality of the system being greater. For *N* number of atoms, each molecule can be described by 3N coordinates, where the position of the centre of mass is specified by 3 coordinates and the orientation is defined by another 3 (or 2 if linear). This means that the PES needs to be a function of 3N-6 (or 3N-5) internal coordinates required to describe the actual structure of the molecule. These internal coordinates include the position coordinates for each atom i.e. bond length, bond angles and dihedral angles, which means that more dimensions are required than can be visualised with a graph. In order to calculate the PES for systems larger than three atoms, parameters such as the bond angles and bond lengths can be fixed because the increased dimensionality is too computationally demanding otherwise. This can reduce the accuracy of the calculated surface because molecules are perturbed by the changing electronic and nuclear interactions resulting from motions such as the vibrations and rotations which would be excluded by fixing the geometry.

In general, depending on the information required, it is possible to fix the surplus coordinates to allow for a 3-D surface to be calculated using *ab initio* methods. The contours of the surface depict the potential energy required by the particles to access that location on the PES. The topography consists of a series of peaks and valleys with varying gradients. Regions known as saddle points are the lowest energy point of a potential energy barrier situated between two valleys and must be overcome in order for the system to move between the low-energy well regions. The position of these barriers in a reaction channel determines the type of energetic excitation needed to overcome them, i.e. translational/vibrational etc. Meanwhile the quantity of energy required is determined by the height of the barrier. The resultant trajectories of the molecules across the surface are given by Polanyi's rules.[1,5]

The PES can be used by theoreticians to model the behaviours of the particles, using techniques such as classical and quasi-classical trajectory simulations and quantum scattering calculations. Such calculations attempt to predict the outcomes of collision events of a molecule with a specified initial state. For inelastic collisions, this is used to calculate the probability of excitation into the available rovibrational product states as well as the scattering trajectories of the products. The probability of the products of a given rovibrational state scattering into a given trajectory provide the theoretical differential cross sections (DCSs). The DCS is used to provide collisional energy transfer and velocity information of the scattering products. What the DCS is and how it is related to these parameters is discussed in the following section. The DCSs produced using quantum scattering calculations can then be compared to those obtained experimentally in order to test the accuracy of the PES.

1.1.2 Collisional Scattering

In order to understand scattering, it is first necessary to be able to define the collision in terms of the colliders involved and the available collision energy. Inelastic scattering is the result of redistribution of translational energy into internal energy modes, therefore defining the total available KE of the system is a necessity. Each particle will contribute a proportion of the total KE through:

$$K.E = K_1 + K_2 \tag{1.7}$$

where K_n is related to the lab frame velocity of each beam (v_n) and the mass of the appropriate particle (m_n):

$$K_n = \frac{1}{2} m_n v_n^2 \tag{1.8}$$

The motion of the particles in the lab frame has a centre of mass (CM) as portrayed in Figure 1.1. The velocity vector of the particles with respect to the CM, $\mathbf{v}_{\mathrm{CM}}$, is:

$$\mathbf{v}_{\mathrm{CM}} = \frac{m_1 v_1 + m_2 v_2}{m_1 + m_2} \tag{1.9}$$

The angular distribution that is detected in an experiment is a centre of mass frame description of the scattering which is independent of the arrangement of the experimental apparatus. As a result, it is necessary to convert from lab frame into the CM frame, the relationship of which is depicted in Figure 1.1. The diagram includes the vectors $\mathbf{u}_1$ and $\mathbf{u}_2$ which describe the CM frame velocities of the two colliding particles. These can be calculated from:

$$\mathbf{u}_1 = \mathbf{v}_1 - \mathbf{v}_{\mathbf{CM}} \tag{1.10}$$

$$\mathbf{u}_2 = \mathbf{v}_2 - \mathbf{v}_{\mathbf{CM}} \tag{1.11}$$

Based on a similar relationship to equation 1.6, the motion of the particles with respect to the CM can be used to find the kinetic energy associated with this motion, K_{CM}:

$$K_{CM} = \frac{1}{2}(m_1 + m_2)\mathbf{v}_{\mathrm{CM}}^2 \tag{1.12}$$

This is directly related to the momentum of the CM which must be conserved in the absence of an external force. The K_{CM} associated with the motion along the CM is unavailable for the collision. The remaining kinetic energy or collision energy, E_{coll}, is available for transfer in inelastic collisions. It is related to the motion along the vector that is positioned relative to the two molecular beams, shown in Figure 1.1, v_{rel} ($v_1 - v_2$) and the reduced mass, $\mu = \frac{m_1 m_2}{m_1 + m_2}$ and can be determined by:

$$E_{coll} = \frac{1}{2}\mu v_{rel}^2 \tag{1.13}$$

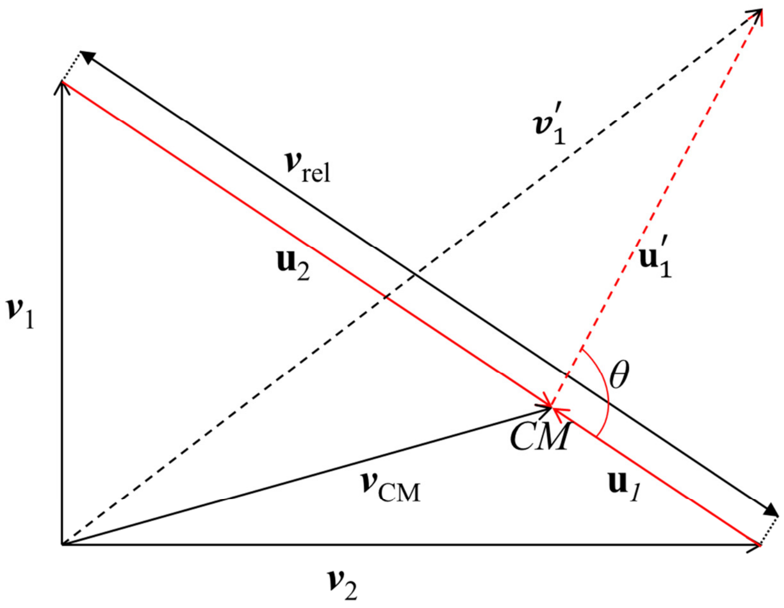

Figure 1.1 Lab frame ($\boldsymbol{v}$) to CM frame ($\mathbf{u}$) transformation, see text for definitions

From this the velocity of the scattered products in the CM frame ($\mathbf{u}_n'$) can be recovered from the equations describing conservation of momentum and energy. The total momentum in the CM frame is zero before and after collision. The energy post collision for an inelastic collision must account for the energy that is transferred into internal modes.

Once the collision energy and the scattering velocities are ascertained, the chance of the collision actually occurring needs to be defined. There are several assumptions that are made in order to determine this: [3]

a) Each collision must be an independent event between the colliders of interest. This assumes that particles do not interact with others during the collision besides the collision partner, i.e. no long range interactions such as van der Waals interactions occur between a particle undergoing a collision and an additional particle unconnected to the collision.

b) Multiple scattering events do not occur to a single particle of interest. See Chapter 2.5 for a description of how and why single collision conditions are maintained.

The collisional cross section, σ_c, can be considered the effective target area for the colliders, the radius of which is given by the impact parameter, b, the distance of closest approach of the colliders when there is no direct interaction.[6] For a collision described by simple collision theory to occur, it can be thought of as $b \leq r_A + r_B$, where r is the radii of particles A and B, see Figure 1.2. However in crossed molecular beam experiments the maximum value for b at which a collision will still occur, becomes a distance, b_{max}. In order to find the probability of a collision, it is necessary to consider the scattering cross section, σ_S, which is sometimes referred to as the integral cross section (ICS). The scattering cross section can be defined by:

$$\sigma_S = \pi {b_{max}}^2 \tag{1.14}$$

This is then related to the reaction probability P by integrating for all values of b and scattering angles, θ, hence σ_S becomes:

$$\boldsymbol{\sigma_S = \int_0^{2\pi} \int_0^{b_{max}} P(b) b \, db \, d\theta} \tag{1.15}$$

Collisions where $b = b_{max}$ can be described as glancing interactions whereas head-on collisions have $b = 0$. Interactions with low impact parameters are more direct collisions and therefore more likely to result in energy exchange or a reaction. The nature of the PES determines the comparative size of σ_S, and, because it is a measure of the probability, processes with large energy barriers will have small cross sections. Likewise collisions occurring on very attractive surfaces will have very large cross sections.

There is a relationship between b and the scattering angle, θ. Large values of b have a tendency to result in smaller deflections to the initial trajectory of the particle hence scattering is into forward angles, i.e. θ = 0°. Meanwhile, small values of b or head-on collisions are likely to result in a greater change to the initial trajectory of the particle hence larger scattering angles are observed, i.e. θ = 180°. This idealized scattering

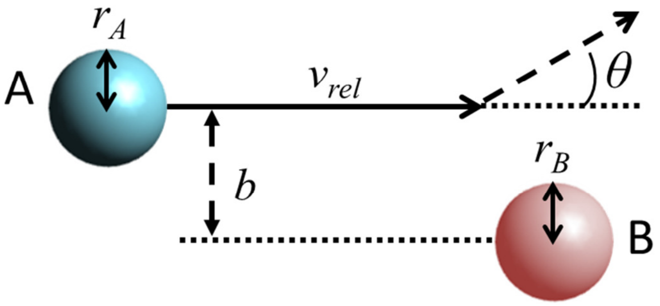

Figure 1.2 Schematic of a colliding system showing impact parameter (b), the relative velocity ($\boldsymbol{v}_{\text{rel}}$) the scattering angle ($\theta$) and the radii of the particles.

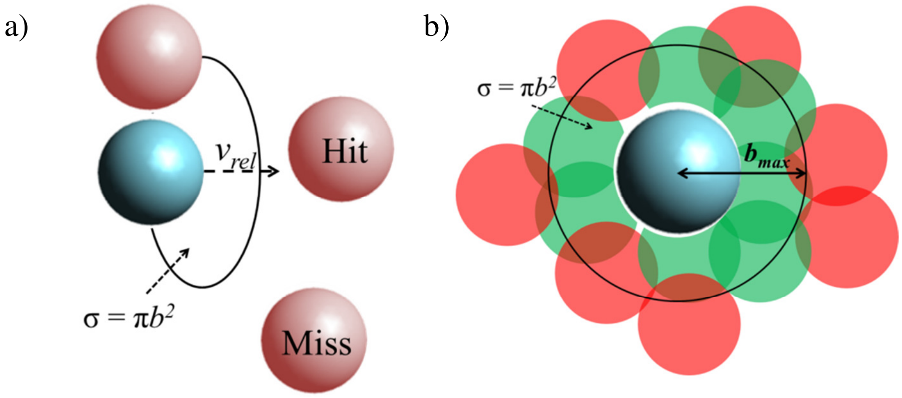

Figure 1.3 Cross section a) side on view, with direction of motion, v_{rel} noted b) view along v_{rel}, green is a hit, red is a miss.

behaviour is dependent upon modelling the particles as hard spheres. The relationship with the collision products is not linear and the range of scattering angles actually observed changes as the molecules involved become more complex and move away from the hard sphere model. However, the scattering angle remains illustrative of the impact parameter and can therefore provide information about the mechanism of the scattering process.

Related to the ICS, is the differential cross section (DCS), $\frac{d\sigma_S}{d\omega}$, which quantizes the angular dependence of σ_S. This is the property that can be measured experimentally and from this other parameters may be calculated. Its mathematical relationship to σ_S is;

$$P(\theta, \phi) = \frac{1}{\sigma_S}\frac{d\sigma_S}{d\omega} \tag{1.16}$$

where $P(\theta, \phi)$ describes the probability of scattering into a given angle, θ, typically defined as the plane of detection, ϕ is the azimuthal angle, and ω is the solid angle. The DCS describes the angular distribution with respect to the product flux for a particular θ and ϕ. Obtaining DCSs experimentally is the primary goal of this thesis in order to provide a description of the scattering of NH_3. The ICS (σ) is the intensity over all scattering angles and can be recovered by integrating the DCS or flux intensity over θ and ϕ.

1.2 Velocity-map Imaging

The original method for measuring experimental cross sections was the use of crossed molecular beams in conjunction with a rotatable quadrupole mass spectrometer.[7] This had the advantage of being a universal detection method, in that all particles are detected so scattering information about both colliders is obtained simultaneously. However, the disadvantages are that only one scattering angle can be measured at a time and the mass spectrometer detects everything in a single mass channel, irrespective of its quantum state. Although this technique is now used less frequently for crossed molecular beam scattering, it is commonly used for liquid surface scattering as it detects the products resulting from both reactive and inelastic interactions.[8-10]

Unlike the mass spectrometry techniques, velocity map imaging (VMI) measures the angular distribution for all angles simultaneously. Ions of a specific mass are measured according to their velocity, which is resolved based on the angular component in the plane of the detector (θ) and the azimuthal angle (ϕ). The ions detected are produced through the use of state selective ionisation methods such as resonance enhanced multiphoton ionisation (REMPI) allowing for DCSs to be produced for each product state. Ionization methods are described further in Chapter 2.3.2.

Many of the experimental components of this work have a long history; molecular beams,[11, 12] time-of-flight (ToF) mass spectrometry[13] and laser spectroscopy have been employed together since the 1960s. For VMI, as with many things, the developments in each individual technology were required and then for something to bring them together, in this case the improvement of detectors – specifically microchannel plates (MCPs) used in conjunction with phosphorescent screens. This combination resulted in a detector that is sensitive to the impact position of the particle. Chandler and Houston combined this type of detector with a ToF apparatus, resulting in the first ion imaging experiments of the photodissociation of CH_3I in 1987.[14] This allowed the velocity and the internal energy of the products to be obtained simultaneously.

The potential of ion imaging was quickly realised by other groups and it was developed into the experimental technique used in this thesis - VMI. Eppink and Parker[15] developed VMI from ion imaging, they were the first to use open electrodes (ion optics) to influence the behaviour of the ions. Figure 1.4 shows a schematic of a VMI apparatus and the arrangement of the ion imaging electrodes for comparison. VMI ion optics comprise of at least a repeller, extractor and a grounded electrode rather than the grid electrode set up of the ion imaging apparatus, there are typically additional electrodes between the extractor and grounded electrode to act as lenses to improve the focussing of the ions. Through the removal of the grid electrodes that are used in ToF

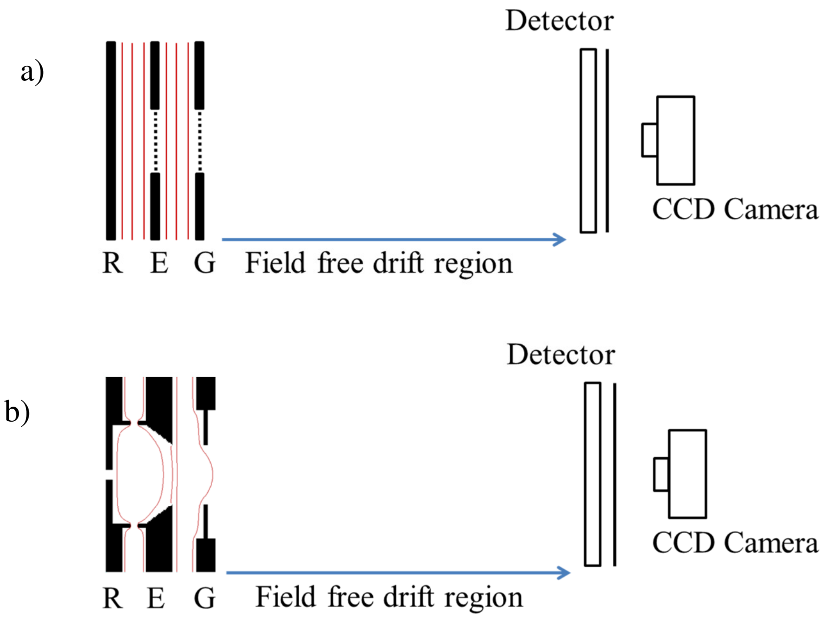

Figure 1.4 a) Ion imaging electrodes b) Typical VMI electrodes with example field lines, additional lens optics are often between E and G. R- repeller, E – extractor and G – ground.

mass spectrometry, subsequent ion imaging apparatus resolution is improved because the grids reduce transmission and deflect the trajectories of the ions. The use of flat, open, annular electrodes produces an inhomogeneous electric field which, when the voltages are correct, results in ions with the same mass and velocity being mapped to the same position on the detector. This occurs irrespective of the initial position within the ionization volume and is the main advantage of VMI, this technique works because each particle will experience the electric fields slightly differently. The electric fields are more curved and the contours of the potential are denser around the electrodes. When an ion that has been created away from the centre region between the repeller and extractor (see Figure 1.4) is accelerated towards the detector, it is more likely to interact with the high potential regions and will therefore experience greater deflection from the electrostatic forces than those ions formed centrally with the same velocity. The first experiment that was performed with VMI was the photodissociation of O_2.[15] The detected O^+ products are produced via numerous pathways resulting in a velocity map image that consists of a series of rings attributable to the kinetic energies of the product pathways. The relationship of the image properties with the characteristics of the ions is explained below. Photodissociation of O_2 has since become the standard experiment for characterising the experimental set-up, see Chapter 2.7.

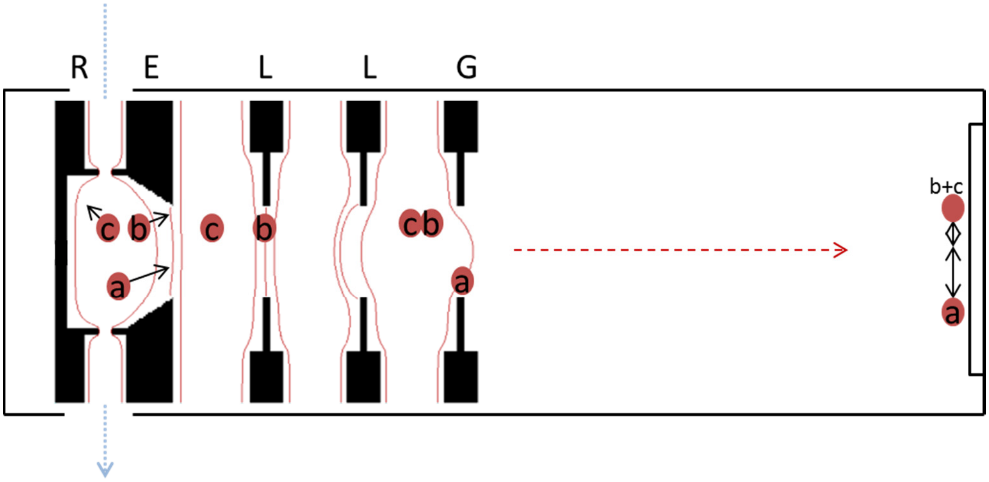

Figure 1.5 Diagram of velocity mapping. Ion a) has a velocity with a greater speed component than ions b & c and is therefore mapped to a different radius from the centre. centre.
Ions b) and c) have velocities with the same speed component but different directions. They are then mapped to the same radius from the centre of the image but would be detected at different positions around the ring. Blue arrow indicates laser intersection, red arrow is the ToF. R – repeller, E – extractor, L – lens electrode and G – ground electrode.

An ion's velocity has two components; speed and direction. As such this has two effects on the final mapped position of the ions. The radius of the particle's impact from centre of the imaged ring is linearly proportional to its speed in the CM-frame. The assumption that is made at this point, is that the ionization of the particle results in negligible ion recoil from the loss of the electron therefore altering the velocity distribution relative to the neutral species.[16] As $m_{electron} << m_{ion}$, this should be a valid assumption as the electron will therefore recoil with the majority of the kinetic energy as it is partitioned by mass. Despite this it has been found that,[16] depending on the REMPI process in question, what little ion recoil there is will be enough to cause it to be a limiting factor of the imaging resolution. The angular position with respect to the centre of the image (θ) at which the ion is detected, describes the angular component of the velocity in the plane of the detector (x,y axes). The ions detected will be described by a small range in ϕ which accounts for the contribution to the direction of propagation from the component along the ToF axis (z-axis).

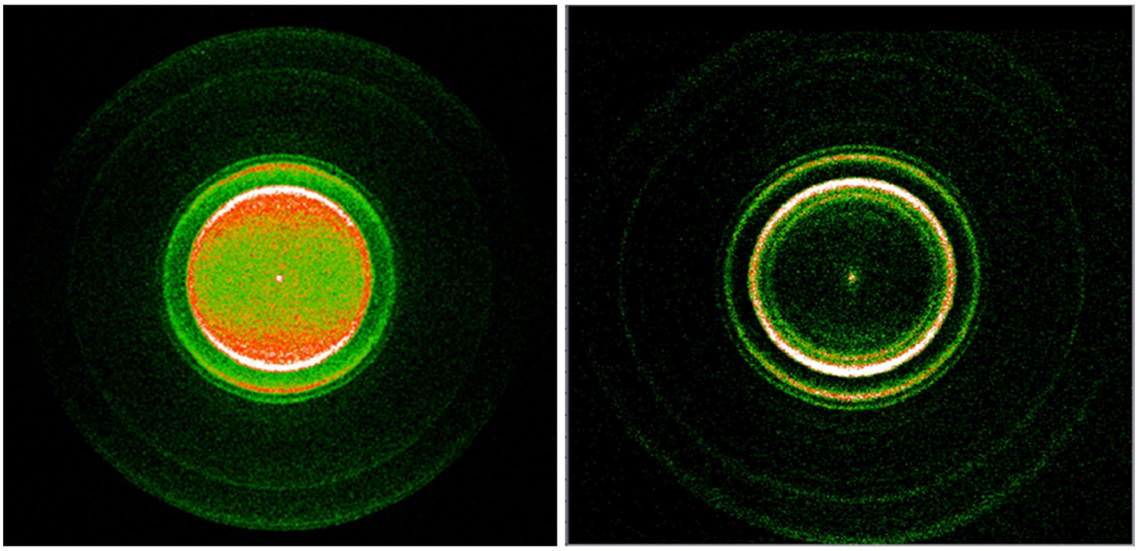

Figure 1.6 Left - Standard VMI image of O (^3P) from O_2 photodissociation at 224.99 nm. Right – 50 ns slice image of the same system.

1.2.1 Slice Imaging

In standard imaging the ion cloud will be accelerated in such a way that it will be compressed along the ToF axis and will therefore arrive at the detector over a minimal time period. With the correct electric fields, the ions moving away from the detector will arrive only a few nanoseconds after the ions that were originally moving towards it. An extraction method, such as Abel inversion or the onion-peeling method must then be applied to the image to obtain the 3-D distribution from the 2-D projection that is imaged. An alternative to this "pancaking" method is to use a slice imaging technique[17, 18] which provides a direct measurement of the scattering in the plane of the detector, without the need for subsequent application of an extraction method. To do this the ion packet must be stretched in the plane parallel along the ToF axis and the detector. Slicing also removes the restriction of requiring cylindrical symmetry resulting in a wider range of systems that can be imaged. Figure 1.6 demonstrates the differences between the "pancake" and "slice" images of the O_2 photodissociation system.

There are two methods for producing a sliced image, the less commonly used method involves pulsing on the repeller for a few hundred ns after ionization so the products have more time to move away from the point of formation.[18] This means that in the drift region the ion cloud focuses down to a minimum temporal distribution and then expands again prior to reaching the detector. The detector is then pulsed on for a few tens of ns so that it only images a slice of the broadened packet which typically has a time width of ~500 ns. In order to be able to extract a DCS the slice will be timed with the centre of the ion packet. However this method reintroduces the grid electrodes that were removed by Eppink and Parker[15] from the typical ion imaging arrangement, reducing the resolution of the images in the ways discussed in section 1.2.

The alternative method of achieving this temporal broadening of the ion cloud, developed by Townsend *et al.*[17] in 2002, is called DC-slice imaging and is now the more widely used method as it is easier to implement. Instead of pulsing on the extraction field, this method employs an additional electrode between the extractor and ground electrodes to apply an electric field gradient to the accelerated ions. This method uses much weaker acceleration voltages than standard VMI to allow for separation of the ions according to their direction of travel with respect to the ToF axis. The additional electrodes are then required to accelerate and velocity map the ions onto the detector. As with the previous method, a time gate is applied to the detector to correspond with the arrival time of the centre of the ion cloud so that only the slice is imaged. The very centre of the ion cloud is the point at which the scattered products have no angular component along the ToF axis, i.e. $z = 0$, $\phi = 0°$ and $180°$, however the detected ions will tend to include a small spread in contributions from z, with the amount depending upon the width of the time slice. Figure 1.7 contains a schematic of the effects of the relevant ion optic set ups used in both “pancake” or “standard” VMI and the DC slice imaging set up. The diagram specifically demonstrates the change in the ion cloud with respect to the ToF axis and the amount of the ion cloud that is recorded. The design of 4 electrodes used by the Suits group[17] has since been increased

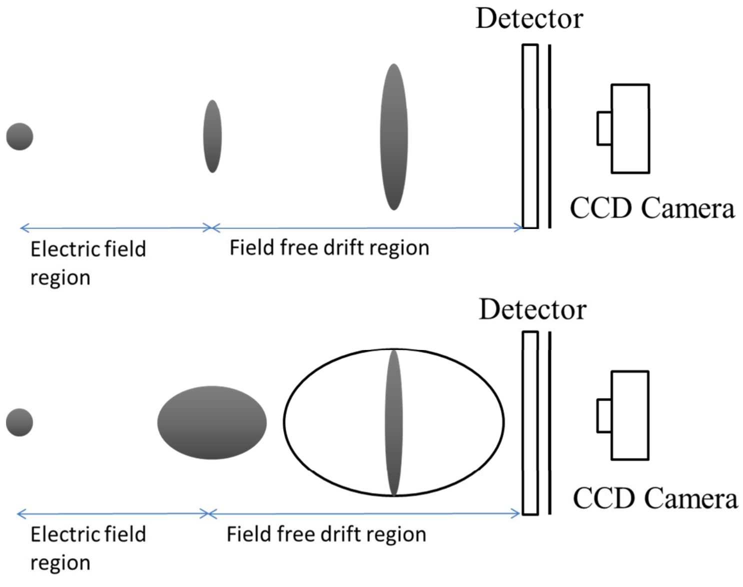

Figure 1.7 Standard VMI (top) vs Slice imaging (bottom), see text for details.

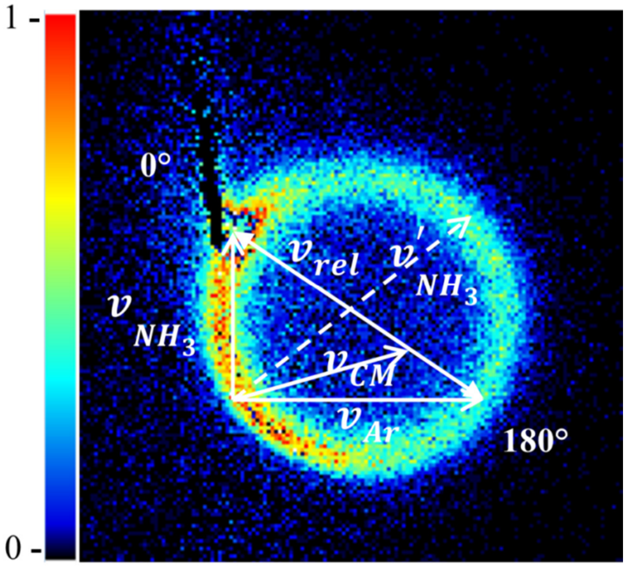

Figure 1.8 VMI image of the inelastic scattering of NH_3 + Ar with a Newton diagram overlaid.

in order to provide even more control over the potential gradient prior to the field free drift region. Lin *et al.*[19] proposed the use of up to 29 electrodes. This ion optics design has provided the basis for the experimental apparatus used in this thesis.

The recorded image is reflective of the lab frame product number density at the time of ionization rather than the total flux of collision products. The flux can be obtained by completing a density-to-flux transformation, as described in Chapter 2.8. Hence the intensity of any point in a raw experimental image, as shown in Figure 1.8, is proportional to the number of molecules with that lab velocity. After density-to-flux transformation the DCS is directly related to the angular distribution.

There are new systems in development that utilise VMI that could be applicable to the study of scattering processes, one example includes pixel imaging mass spectrometry, PImMS.[20, 21] This technique allows for an image to be recorded at multiple times during the ToF allowing for detection of scattering in many different mass channels or numerous slices of a single Newton sphere. The detection of multiple mass channels is advantageous to the detection of photofragments and reactive scattering and brings to VMI one of the advantages of mass spectrometry detection techniques. Multiple slices through a single Newton sphere allows for a full 3-D distribution to be obtained in a single experiment. Both mean that images that previously would have required many days of experimental time to collect separately can now be recorded as part of a single experiment.

1.3 Molecular beams

The image radius is directly related to the velocity of the products which in turn are indicative of the collision energy and the initial velocities of the colliders. As a result if the spread in initial velocities is large then this will have an equivalent effect on the spread in the image radius. Likewise if the distribution of initial velocities is minimised so is the spread of detected velocities in the image. Molecular beams are used to produce a collimated beam of molecules with a minimal spread in velocities and internal energy distribution so that the products detected are known to derive from a collision with as many defined parameters as possible. This means that the experimental DCSs can subsequently be related directly to the dynamics of the collisions.

The type of molecular beam that provides these conditions are produced using a supersonic expansion.[22] In order to do achieve this, the nozzle diameter must be small (< 1 mm) and the stagnation pressure of the gas prior to expansion must be such that the length of the mean free path is reduced to less than the nozzle diameter. It is also necessary for the gas expansion to occur from a high pressure region into a low pressure one, in order to prevent the expanding molecules undergoing thermalization with the new environment. Upon expansion many collisions take place as the molecules exit the nozzle and in the region immediately afterwards. Collisions that result in the velocity obtaining a directional component along the beam axis will allow the particles to leave the region around the nozzle. This results in the random motion of the expanding particles being converted into a highly directed molecular flow. The majority of internal energy is converted into translational motion, hence, the particles in the beam will exist in their electronic ground state and the lowest few rovibrational states depending upon the size of the molecule and the energetic spacing of these levels, particularly the vibrational levels. The translational temperature of the molecules can be cooled down to a few K and the velocity distribution will be minimised throughout the beam. In order to form a beam with a narrow angular distribution, a skimmer is typically placed downstream of the jet expansion. This will collimate the beam and reduce the number of effusive particles, which have a large velocity distribution, reaching the scattering centre in crossed beam experiments or the point of ionization in other set-ups and causing background noise. Collimation also reduces turbulence resulting from the shock wave structure generated from the supersonic motion of the molecules.[23]

The energy distribution that the products have at the point of detection, has typically been imparted by external factors, either through excitation by light or undergoing an inelastic collision. The high directionality of the molecular beam also means that any change in the direction is also due to the event under investigation. In VMI any deviation from the initial velocity and energy of the particle is directly relatable to the dynamics of the process being studied.

1.4 Inelastic scattering experiments

Initial work incorporating crossed molecular beam (CMB) methods originally utilised continuous beams in conjunction with mass spectrometry (MS) product detection. These traditionally used a rotatable mass spectrometer in order to measure the signal intensity across the range of possible scattering angles.[7] The success of this method in investigating collisional dynamics was fully acknowledged by the Nobel Prize in Chemistry that was awarded to Herschbach, Lee and Polanyi in 1986.

Velocity map imaging of inelastic collisions has been used to such an extent that there are collisions for particular benchmark systems, such as NO [24-30] and OH,[31-34] that have been explored in such detail that it is tempting to say that everything is known about them; although undoubtedly as techniques evolve further there is always more to learn. These systems have also proven to be incredibly useful in concurrently evolving theoretical methods.[24, 35, 36]

The OH radical has been studied with numerous colliders for both inelastic and reactive scattering. Its dynamics are of interest, as OH plays numerous roles in combustion, astrochemistry and it has a key role in atmospheric reactions in the destruction of O_3 and formation of hydrocarbon radicals through H-abstraction. For inelastic collisions, it has been used as a probe of both energy transfer in gas phase collisions[31, 32] and the structure of liquid surfaces.[37, 38] The NO radical has also had much experimental investigation and many theoretical DCSs have been published.[24] The collisions of NO(X) with Ar[25] have been used to study concepts such as the rotational alignment of the NO and how the hard shell nature of the interaction potential affects this property during a collision with Ar.[24] Recently collisions of electronically excited diatomics with rare gas atoms have been studied. The molecules investigated are NO(A $^2\Sigma^+$)[39-41] and OH(A $^2\Sigma^+$)[34, 42-44] for which the colliders include Ar, He and Kr.

1.4.1 Gas phase scattering with polyatomic molecules

The bulk of the literature investigating crossed molecular beam scattering of polyatomic molecules is heavily biased towards reactive scattering. The focus centres particularly on H-abstraction by small radicals for which the Suits' group has produced a large body of data in this field.[45-50] Their work includes investigations of the reactive collisions of Cl radicals with saturated and unsaturated hydrocarbons such as propane, butane, butene and pentene. They have found that the abstraction process proceeds by a number of pathways. One particular development has been the discovery of the roaming pathway for this process whereby the radical is frustrated post collision and roams around the molecule until it gains sufficient energy to abstract a H.[51-53]

The inelastic scattering of polyatomics molecules has focussed on the scattering of a single polyatomic with a rare gas species[54-57] due to the complexities discussed in Section 1.1.1 involved in generating a PES for larger systems. DCSs for bimolecular collisions have been reported, however, these concentrate on the scattering of two diatomic molecules, such as the work by Kirste *et al.* on NO + OH [58] and OH + H_2 [33] collisions. Although diatomic-diatomic molecular collisions are not studied in this thesis they provide the basis for the evolution of theoretical techniques to deal with two molecular systems, as this opens the possibility for excitation of both colliders. An example of this is found within the work of the Chandler group who have used VMI to characterise the inelastic scattering of the rotational ground state of HCl with rare gas colliders and the molecular systems of N_2 and CH_4.[59] They find that the DCSs of HCl + N_2 exhibit significantly more backwards scattering for HCl $J_{\mathrm{HCl}} = 4$ & 5 product states compared to the same product scattering from collisions with rare gases of a similar mass, i.e. Ar. The opposite trend is observed for HCl $J_{\mathrm{HCl}} = 2$ & 3 where the N_2 collisions result in more forwards scattering than the rare gas collisions. The scattering of HCl imaged from collisions with CH_4 is more forward scattered than the other systems investigated and also exhibits evidence of co-excitation of the CH_4.

There are a few existing examples of bimolecular collisions involving polyatomics with diatomics and the scattering of HCl + CH_4 mentioned previously is a rare example, particularly as the diatomic is not molecular hydrogen. H_2 is often chosen as it is the smallest molecule available; it is the logical place to move on to from atomic system colliders, as it is comparable to He. It is also a good place to begin molecule-molecule collisions as it is also easier to describe theoretically as it only has 2 electrons to account for unlike larger molecules. Parker and co-workers have studied the rotational excitation of H_2O[60, 61] and its deuterated analogues[60] HDO and D_2O through inelastic collisions with H_2 at collision energies between ~400 and 600 cm^{-1}. They present theoretical and experimental DCSs for the inelastic scattering of the three water isotopologues with H_2 which suggest that the PESs for these systems are a very good representation of the interactions. The majority of the scattering for all three systems is primarily into the forwards angles, which is found to favour collisions where the H_2 initial state is rotationally excited. The contributions into larger angles that appear in the DCSs are generated almost exclusively by collisions resulting from H_2 in the rotational ground state.

Our own group has previously investigated the inelastic scattering of methyl radicals and molecular hydrogen in various collisional combinations i.e CH_3 (CD_3) + H_2 (D_2).[62] This work is used as a comparison to the data presented in Chapter 4 and is described in greater depth there.

1.4.2 Scattering with NH_3

The attention of this thesis is focussed on the inelastic scattering of NH_3. The majority of the existing literature for crossed molecular beam experiments concern testing the PESs for collisions of NH_3 with numerous rare gas atoms, including He,[63-65] Ar[66-69] and Ne.[70] Meyer was the first to conduct crossed molecular beam experiments with NH_3 and He[64, 65] and Ar.[68, 69] These experiments studied head-on collisions with high collision energies using a complex ToF apparatus that uses parallel product detection, in conjunction with REMPI in order to obtain difference ToF spectra to produce fully state resolved ICSs and DCSs for the scattered NH_3. When compared to theoretical ICSs and DCSs calculated for the high energy conditions in use in the experimental data,[71] both NH_3-He and NH_3-Ar demonstrate good agreement between calculated and experimental cross sections. The authors are keen to highlight the differences in the NH_3-Ar scattering at different collision energies and stress the importance of comparing like-for-like. This is due to features that appear in the DCSs at collision energies of 1274 cm^{-1} that quickly disappear at lower energies, as the relative contributions of the repulsive and attractive parts of the potential change.

Since Meyer's work theoretical techniques have evolved resulting in improved accuracy of calculated PESs. The PESs for NH_3 collisions with a range of colliders have been calculated, however more recent experimental data has focussed on collisions involving the deuterated isotopologue, ND_3. This is a valid test of the PESs for NH_3-rare gas as the shape is expected to be the same with only minor adjustments required to account for the difference in the reduced mass of the system. Tkáč *et al.* have published experimental and theoretical DCSs for the scattering of ND_3 and rare gas colliders including He [63] and Ar.[66] The ND_3 experimental data is used as a test of the accuracy of the PESs for these collisions by comparing the extracted DCSs to those produced by quantum scattering calculations. The experimental and theoretical data indicates that the existing PESs are good predictors of the particle interactions for these systems by showing a strong correlation between the experimental and theoretical DCSs. This experimental data is obtained using a combination of initial state selection with a hexapole for the ND_3 molecular beam and VMI detection. The images and extracted DCSs reveal that ND_3-He exhibits more sideways and backwards scattering than the Ar collisions.[66] This is reflective of the forces that are dominating the collisions, ND_3-He collisions are found to occur on the repulsive regions of the PES whilst ND_3-Ar interactions occur on a more attractive surface. The use of a hexapole to select the initial state of the ND_3 has allowed for the effect of parity conserving and parity changing transitions on the DCSs of specific product states. The conclusion is that parity conserving transitions are favoured over parity changing transitions and theory suggests that many diffraction oscillations are expected in transitions of this nature. In addition it is found that there are differences between the different parity changing transitions i.e. $+ \rightarrow -$ vs $- \rightarrow +$ resulting from the energy splitting of the different inversion levels.[63, 72] In contrast to the DCSs of the parity conserving transitions, only a single sharply forward-scattered peak is predicted by theory, unfortunately the experimental data does not have sufficient resolution to observe the diffraction oscillations in the velocity map images. In addition to rare gas scattering there has also been experimental work reported that tests the PES for ND_3-H_2.[73] This provides a comparison for the data presented in this thesis in Chapter 4.

NH_3/ND_3 is an ideal candidate for use with techniques that allow for initial state selection such as hexapoles and Stark decelerators, as such it has been used for the study of low energy collisions. The existing work by Loreau *et al.*[74] is purely theoretical and uses the quantum close-coupling method to describe the scattering cross sections of NH_3 and ND_3 with rare gas atoms He, Ne, Ar, Kr and Xe at collision energies of 0.001 to 300 cm^{-1}. It is also the first reporting of the PES for NH_3-Kr and NH_3-Xe. The predicted cross sections exhibit numerous resonances that are assigned to either Feshbach resonances or those resulting from quasi-bound states.

1.5 Overview of Thesis

The central aim of this thesis is the experimental investigation of inelastic scattering of NH_3 from collisions with a range of collider species. The crossed molecular beam apparatus and experimental parameters are described in Chapter 2, including a discussion of the spectroscopy of NH_3 and the methods used to extract the DCSs from the raw experimental images. The collisions of NH_3-Ar are the subject of Chapter 3, building on the existing data with a discussion of the evolution of the DCSs according to the product state of the NH_3. The later chapters detail bimolecular collisions. The first of these, Chapter 4, focusses on the outcomes of collisions of NH_3 with a diatomic system, D_2, which adds to the current literature of polyatomic-diatomic collisions. It is the first discussion of this particular scattering system although existing work, by Tkáč *et al.,*[73] using the deuterated analogue provides some background. The data presented also offers a contrast between the scattering of symmetric top molecules that are closed-shell in nature (NH_3) and open-shell systems (CH_3/CD_3).[62] The final chapter of experimental results, Chapter 5, presents the first DCSs for polyatomic-polyatomic inelastic scattering. The focus is on NH_3 collisions with small primary hydrocarbons, the species used are methane, ethane and neopentane. These are all primary hydrogen containing molecules allowing direct comparisons to be made between the collisional systems. Chapter 6 is a brief discussion of the conclusions that have been drawn from the experimental work presented.

Chapter 2 – Experimental

2.1 Introduction

The experimental work that is described in this thesis is dependent on the combination of two techniques – molecular beams and velocity map imaging (VMI). VMI was described in Chapter 1. Molecular beams have been a common feature in experiments for the characterization of fundamental dynamics since their first use by Stern in the 1920s.[11, 12] A molecular beam is produced by the expansion of a gas from a higher pressure region into a low pressure region through a small orifice. In the expansion, the molecules move from a point and propagate forwards forming a conical distribution that can be skimmed to produce a collimated beam. In the throat of the expansion, the molecules undergo many collisions resulting in vibrational quenching and rotational cooling. A more detailed description of how this occurs is in Chapter 1.3.

The ability to produce a short gas packet using a pulsed nozzle has allowed for a shift towards experimental techniques that cannot withstand the gas volume produced by a continuous nozzle apparatus and for more selectivity in the nature of the molecules being investigated. The more control that is gained over the molecules of interest, the more that can be characterised and understood about the entire system. Hexapoles and Stark decelerators are an example of how far this control of molecular beams has been advanced.[36, 63, 75, 76] The experiments described in this thesis do not go as far as initial state selection, however, as is discussed in Section 2.4.2, only a few initial states are available. The other advantage of pulsed molecular beams is that they reduce the requirements for very large pumps and cryo-traps to maximise the efficiency of the removal of the background gas. This has allowed for vacuum chambers to be reduced in size. This is an aspect that has been particularly taken advantage of in the experimental apparatus described in this chapter.

Using VMI in conjunction with CMB allows for all scattering angles to be imaged simultaneously, when previously multiple sets of experiments would have been required to detect products at the complete range of angles. It also allows for use of laser based ionization schemes, such as resonance enhanced multiphoton ionization (REMPI), for product detection which provides an experiment the ability to be state-selective. Combining this with DC slice imaging, as described in Chapter 1.2.1, allows for further selectivity over the portion of the products detected, by only imaging a 2D distribution of those with (x, y, z=0) components relative to the plane of the detector. The experimental apparatus and analytical methods are detailed in this Chapter.

2.2 Experimental overview

The experimental setup used for the work described in this thesis is a crossed molecular beam velocity map imaging (CMB-VMI) machine designed by Dr Stuart Greaves. The chamber is designed to be especially compact in comparison to others of this type. This increases its portability for possible use at central facilities and most importantly to minimise the distance from nozzle to point of collision, therefore maximising the number of molecules available for collision. This design also provides a reduced volume to allow for efficient pumping in order to optimise single collision conditions. The performance of this chamber design was fully characterized in the thesis of Ondrej Tkáč [72] and subsequent publications.[62, 77, 78] However, the apparatus has since been moved from Bristol to Edinburgh and there have been replacements to some of the components, hence a full characterization is described herein.

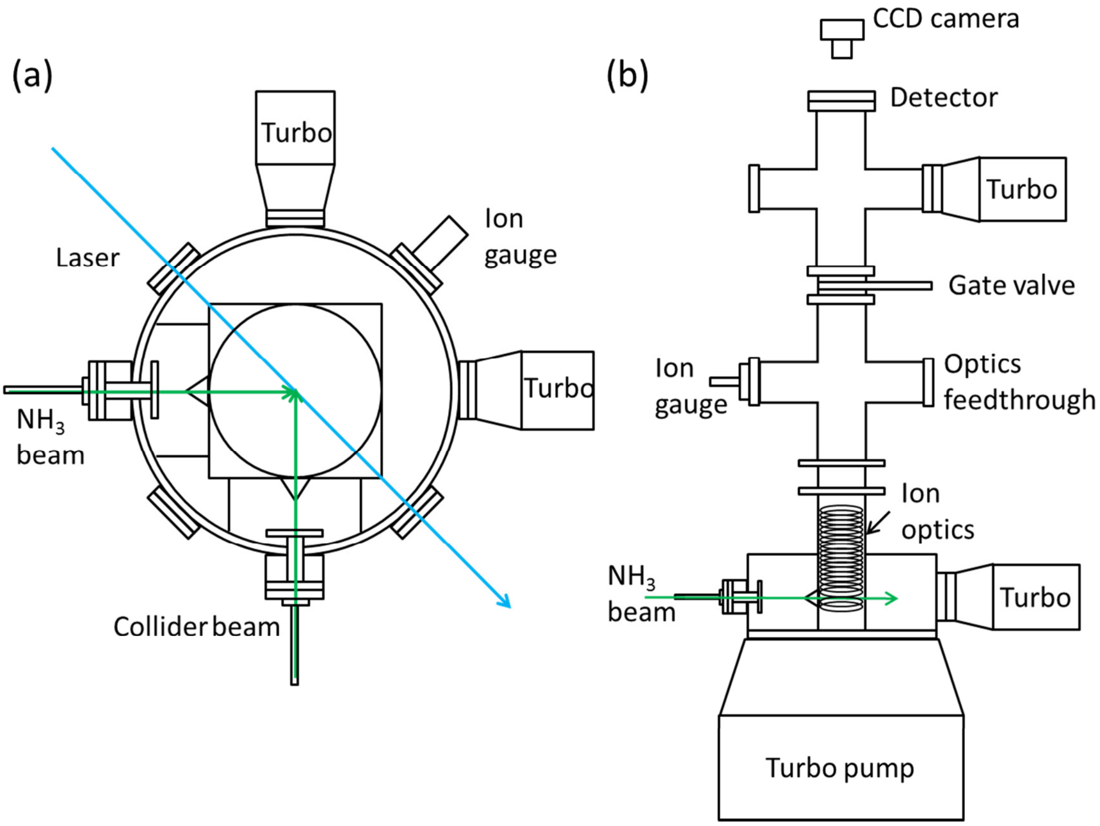

Figure 2.1 Schematics of the experimental apparatus. a) horizontal cut through the main chamber, through the plane of the molecular beams, including the paths of the molecular beams (green lines) and the ionization laser (blue line). b) vertical cut through of the entire apparatus parallel to the primary molecular beam marked in green.

Figure 2.1a is a schematic of the experimental apparatus used for the work in this thesis, presented as a cut through the plane of the molecular beams. The molecular beams expand into individual source regions before passing through a pair of skimmers into the main chamber and intersecting at 90° in the interaction region. The laser, which is used to state-selectively ionize the scattered products, intersects the primary molecular beam at an angle of 45° (and thus the second beam at 135°). The collision region is positioned in the centre of a stack of vertically mounted electrodes which are used to accelerate the nascent ions perpendicular to the molecular beams towards a position sensitive detector as shown in Figure 2.1b. The electric field produced by the electrodes differentiates the ions as described in Chapter 1.2, before a slice of the ion packet is recorded using the DC-slicing method. The ion imaging detector (Photek) consists of a pair of microchannel plates (MCPs) and a phosphor screen (P46) observed by a CCD camera (Basler A310f, 782 x 582 pixels) to record images of the ion hits. The impact of an ion generates an electron cascade in the MCPs, which are then accelerated on to the phosphor screen causing it to phosphoresce. The photons emitted by the screen are detected by the CCD camera. This records the 2-D position of the ions at the centre of the Newton sphere. A low-light silicon photomultiplier (SPM) (SensL) is used to collect the sum of the light from the phosphor screen and is connected to an oscilloscope (Lecroy WaveRunner) to allow the signal level to be monitored in real-time during image collection and enable REMPI spectra to be obtained for characterisation purposes.

The camera relays the ion hits back to a computer where a purpose-built LabView data acquisition program records their impact position and sums the total intensity for each camera pixel over a given number of shots. The data acquisition program also controls the firing of the nozzle of the collider beam in order to obtain an image of the background signal produced by the unscattered NH_3 in the chamber in the same acquisition cycle to the experimental data. Both nozzles fire for 50 shots before the collider nozzle is turned off for a further 50 shots. The single nozzle image is then subtracted from the total summed image in order to produce a final background subtracted image.

Physically, the chambers comprise of a spherical octagon which contains a separate cuboid where the collision region is situated. The source regions are also within the spherical octagon and are differentially pumped by a turbomolecular pump (Edwards nEXT 300D) mounted on the base. They are kept fully separate from the scattering region by baffles. The base pressure of the source regions is on the order of ~1×10^{-7} mbar whilst the interaction region has a base pressure at ~5×10^{-9} mbar. A pair of solenoid valves (General Valve Series 9) are used to produce a supersonic gas expansion in order to generate the molecular beams. The valves are pulsed at 20 Hz with pulse durations of ~180 μs. The supersonic expansion is then collimated by a skimmer mounted ~1.7 cm from nozzle 1 on the wall of the central cuboid and ~1.5 cm for nozzle 2. The positions of the nozzle faceplates are adjustable over a 0.2 cm to 4.3 cm range as they are mounted on posts extending from the central cuboid wall. The diameter of each nozzle orifice is 0.8 mm and the skimmers are 1 mm in diameter.

The distance from the entrance of the skimmers to the centre of the collision region is 3.69 cm. This short distance to the interaction region is one of the advantages of this small chamber setup as it increases the density of molecules in the interaction region without increasing the total volume of gas required maintaining efficient pumping. For the experiments described within this thesis the molecular beams, the NH_3 beam (Figure 2.1a) is always 3% NH_3 in Ar with a stagnation pressure of 4 bar. The collider beam (Figure 2.1a) is typically an expansion of either 4 bar pure Ar or D_2, or a gas mixture of 25% hydrocarbon (CH_4, C_2H_6 or $C(CH_3)_4$) in 4 bar He.

The operating pressure within the interaction region when the molecular beams are running is typically on the order of ~1×10^{-5} mbar. To minimise gas build up in the collision region there are two small turbo pumps (Pfeiffer HiPACE 80) mounted directly in the path of the molecular beams. There is an additional turbomolecular pump (Pfeiffer HiPACE 80) mounted on the side of the ToF tube to prevent gas build-up in the vicinity of the detector. All of the turbomolecular pumps are backed by a scroll pump (Edwards nXDS 15iC).

2.3 Spectroscopic techniques

2.3.1 REMPI

As previously mentioned the detector in the experimental set up consists of a pair of MCPs with a phosphor screen. In order to create the electron cascade within the MCPs that then causes the phosphor to phosphoresce, the impacting species need to have a high K.E, ionising the species of interest and accelerating it using electric fields are the methods used to impart this energy to the molecules of interest. The experiments described are investigating the collisions between neutral molecules and as such require an ionization step after collision, which is achieved using REMPI spectroscopy.

Photoionization is the use of one or more photons to impart enough energy to a molecule so that an electron is excited beyond molecular influence and is therefore ejected instead of undergoing relaxation, resulting in an electron deficient molecule, a cation. This is dependent on the energy of the photon(s) being equivalent to or greater than the amount required to electronically excite the species of interest beyond its ionization threshold.

$$AB + h\nu \; \rightarrow \; AB^{*} + h\nu \rightarrow AB^{+} + e^{-} \tag{2.1}$$

Ionization techniques can be characterized depending on the number of photons required to achieve ionization and how they interact with the molecules with respect to their spectroscopic properties.

- Single-photon ionization – as its name suggests this technique uses only a single photon to overcome the ionization potential (IP) (Figure 2.2a). However, for most small molecules the IP is above 8 eV, which requires high energy VUV light sources such as those used as synchrotron radiation in order to achieve electron ejection.
- Multiphoton ionization – again its name is self-explanatory in that it uses multiple photons to achieve ionization so lower energy photon sources such as lasers can be used as a photon source. The energy of the UV wavelengths being used in these experiments mean that this is a soft ionization technique, in that there will not be enough excess energy to result in fragmentation of the molecule.

Multiphoton ionization can be subdivided into two types; resonant and non-resonant. Non-resonant simply depends upon a molecule simultaneously absorbing several photons with a total energy to overcome the IP (Figure 2.2b). For this to occur, a high photon density is necessary, as this experimental setup uses a lens to focus the laser it is possible that at the focal point this mode of ionization may be accessible.

The nature of non-resonant multiphoton ionization means it has an influence upon the amount of background scatter that is detected, as anything that is present in the ionization volume may be ionized and reach the detector. This background will be

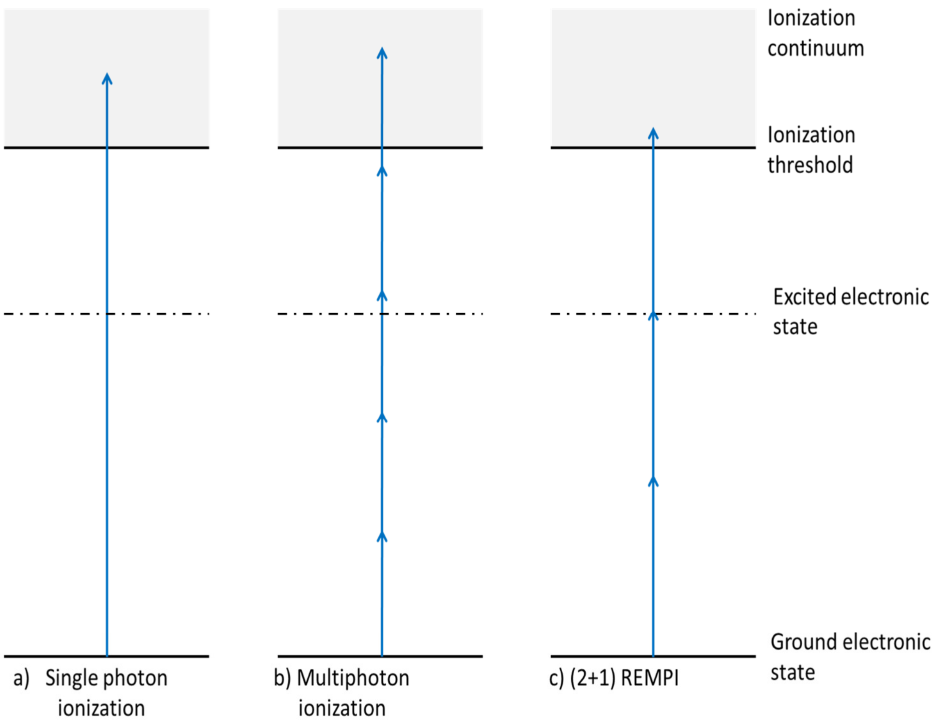

Figure 2.2 Ionization processes from the ground electronic state, a) single photon ionization, b) multiphoton ionization and c) (2+1) REMPI. The photons are represented by individual arrows, whose length represents their energy.

observed within the ToF-MS spectrum of the system and can then be reduced by DC-slice imaging if occurring at a different arrival times (e.g cluster ions) or will be mapped to different positions to the main scatter.

As shown in Figure 2.2, REMPI is a two-step process whereby one or more photons are used to initially excite the molecule to an intermediate electronically excited state before another photon of the same or different energy comes in to complete the ionization step. For molecules that occupy a rovibronic energy level that lies below the intermediate state with an energy gap that is the same as the incoming photons, the probability of ionization is dramatically increased. This resonance between the photon energies and the energy gap enhances the product state's detection probability because the ionization probability is increased by several orders of magnitude compared to non-resonant multiphoton ionization. Tuneable lasers are required in order to produce the photons of the wavelengths that are resonant with the energy gap of the states being investigated. The increased control over the photon energies permits the rotational and vibrational structure to be probed state-selectively.

2.3.2 Laser setup

The experiments discussed in this work depend upon the detection of NH_3, the ionization threshold of which is 10.02 eV.[79] The necessary energy is achieved using a focussed laser to allow for the use of a (2+1) REMPI scheme in the UV, at ~317 nm. The NH_3 collision products are ionised from the electronic ground state through the $\tilde{B}$ $^1E''(\nu_2 = 4)$ intermediate state.[80] The laser intersects the interaction region horizontally at 45° to the primary (NH_3) beam. The laser setup of this experiment comprises a tuneable dye laser (Sirah Cobra-Stretch) that is pumped by the 532 nm output of a pulsed Nd:YAG laser (Continuum Surelite SLI-20) operating at 20 Hz. The dye laser utilised the 532 nm light in conjunction with DCM dye in methanol, and a BBO doubling crystal to generate the required wavelength of 316 to 319 nm which a beam width of ~2 mm which is then focussed into the chamber using a 250 mm lens. The operating power of the probe laser is 0.75 mJ/pulse with a pulse duration of 7 ns with a linewidth prior to doubling of 0.0027 nm.

For the option of radical production, the nozzle mounting flange for beam 1 has 2 windows on with the nozzle faceplate holding 2 prisms so a laser can be brought in and applied to the throat of the expansion. Although not in use, the presence of the prisms can result in additional gas build up in the source region, Section 2.5 discusses this in more detail. As radical colliders are not used in the work described in this thesis the details of the actual set up are not discussed. Further information can be found in the work of Tkáč *et al.*[72, 78]

2.3.3 Spectroscopy of NH_3

The rotational spectroscopy of ammonia is very rich and complex but has been well-defined since the 1980s.[80] It is an oblate symmetric top molecule with a pyramidal structure that has C_{3v} symmetry. All molecules have 3 moments of inertia, I_A, I_B and I_C, the relationship of these to one another is dependent on the shape and size of the molecule. Symmetric tops have two moments of inertia that are equal and one that is different, for oblate tops such as NH_3 this is $I_A = I_B$ and $I_C > I_B$. As a result the rotational energy (E_J) can be described by the rotational term value (F_J), which is related to energy by E_J/hc;[81]

$$F_{Jk} = \tilde{B}J(J+1) + (\tilde{C} - \tilde{B})k^2 \qquad 2.2$$

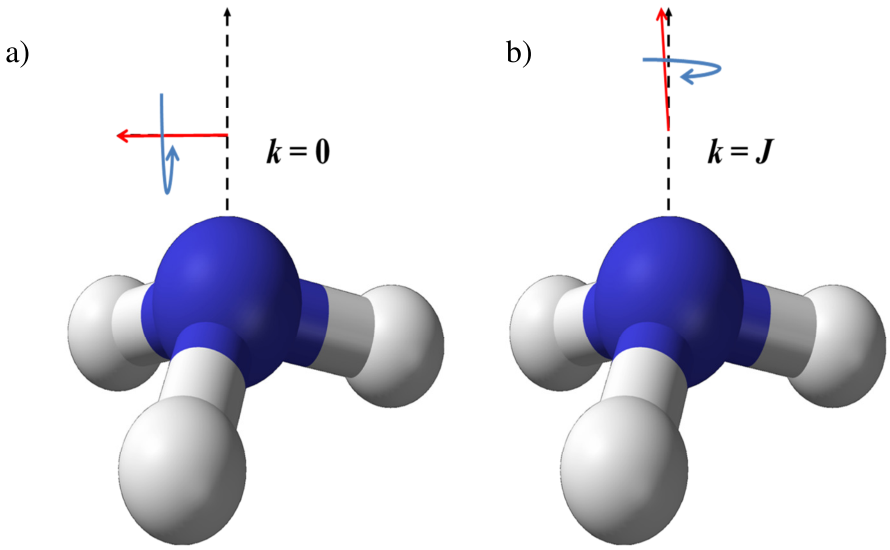

Figure 2.3 Diagrams demonstrating the alignment of the angular momentum vector (red arrow) of NH_3, with respect to the primary molecular axis (dashed black line). Examples are the two extremes a) $k = 0$ and b) $k = J$

Where $\tilde{B}$ and $\tilde{C}$ are the rotational constants (in cm^{-1}) derived from the moments of inertia, and J and k are quantum numbers which describe the nature of the rotation of the molecule. J is used to denote the total rotational angular momentum quantum number and k is the projection of J onto the principle axis of the molecule, i.e. the C_3 axis in NH_3. The quantum number k must be equal to integer values of $2J$+1, where the limiting values are $-J \leq k \leq J$. The extreme values of k are; $k = 0$ whereby the projection of the angular momentum is perpendicular with the principle axis and $k = \pm J$, where it becomes closer to parallel with the principle axis depending on the size of J (see Figure 2.3).

Figure 2.4 demonstrates the relationship between rotational quantum state, J_k and the primary molecular axis. The rotational angular momentum vector, **P,** describes the axis about which the molecule is rotating. The component along the primary molecular axis takes the values $k\hbar$ whilst its perpendicular component is described by $\sqrt{J(J+1)}\hbar$. From this, trigonometric identities can be used to describe the angle of **P** relative to the primary molecular axis (ω):

$$\omega = \cos^{-1}\left(\frac{k}{\sqrt{J(J+1)}}\right) \tag{2.3}$$

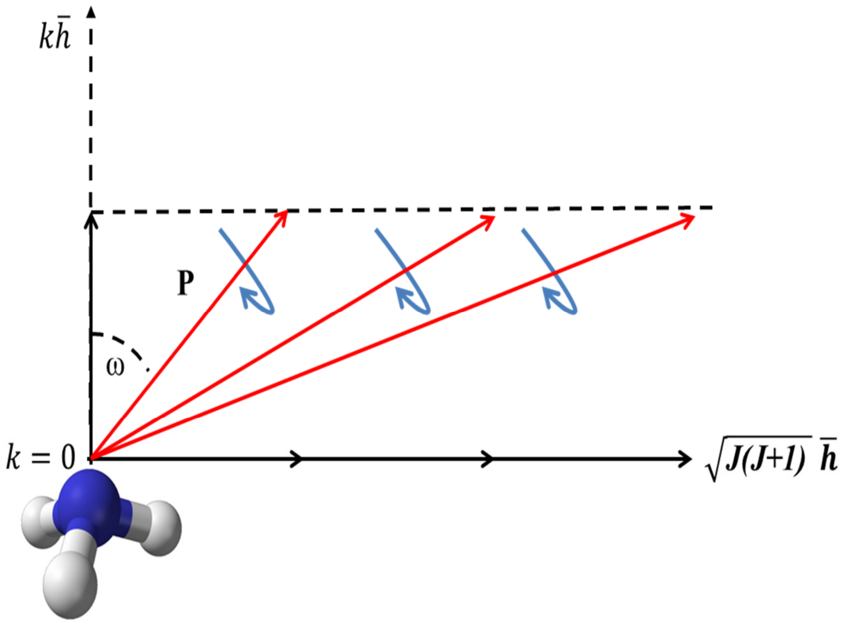

Figure 2.4 Vector description of angular momentum shows three vectors describing P for $J_k = 1_1$, 2_1 and 3_1 (red arrows) with respect to the molecular symmetry axis ($k\hbar$) and the perpendicular axis $\sqrt{J(J+1)}\hbar$. The angle of $\mathbf{P}(\omega)$ relative to $k\hbar$ is marked for $J_k = 1_1$

Hence for states where $J > 0$, there is always some contribution from the perpendicular component as $\sqrt{J(J+1)}$ can never equal k, hence ω can never equal 0. In addition k cannot be greater than J because the magnitude of **P** defines the contribution from the primary molecular axis.

For $k = 0$, the degeneracy of the energy level must account for the component of angular momentum about the external laboratory-frame z-axis, often denoted as M_J, however, it has no angular momentum contributions about the primary axis, resulting in a degeneracy of $2J+1$. As the energy of a symmetric top is dependent on both J and k, any states other than $k = 0$ display double degeneracy because the direction of the rotation, i.e. clockwise or anti-clockwise, does not change the overall energy. Hence the degeneracy of a rotational energy level, J_k, where $k \neq 0$ is $2(2J+1)$-fold. This double degeneracy from the J_k state does not apply to $k = 0$ state because the rotation has no component around the C_3 axis. However, the electric fields of the ion-imaging technique in use are not sufficient for the detection of the Stark splitting in the REMPI spectrum that would result from these degenerate energy levels.

The equation for rotational energy stated above treats the molecule as a rigid rotor. Molecules are more flexible than a true rigid rotor so it is also necessary to consider the

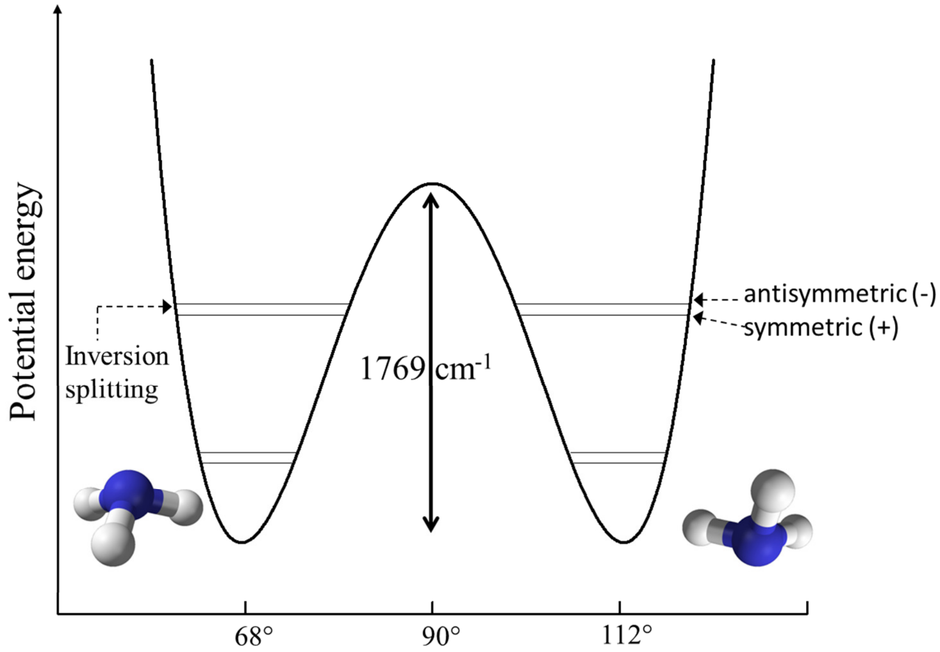

Figure 2.5 Potential energy diagram showing double well minimum of the v_2 "umbrella" mode of NH_3. The barrier to inversion is noted as are the minimum energy geometries of the NH_3.

effect of centrifugal forces on the bond lengths and angles. To take into account the consequence of this upon the energy, it is necessary to include the centrifugal distortion constants (D_J, D_k and D_{Jk}) hence the modification to equation 2.2 is as follows:[81]

$$F_J = \tilde{B}J(J+1) + (\tilde{C} - \tilde{B})k^2 - D_J J^2(J+1)^2 - D_{Jk}J(J+1)k^2 - D_k k^4 \qquad 2.4$$

Table 2.1 Molecular constants of all the molecules (cm^{-1}) used in this thesis.

	NH_3[82]	**D_2[83]**	**CH_4[84]**	**C_2H_6[85]**	**$C(CH_3)_4$[86]**
B	9.9466	30.443	5.2406	2.669	0.148
C	6.2275	-	-	0.663	-
D_J	8.49E-04	0.0114	1.09E-04	1.03E-06	-
D_{Jk}	-1.58E-03	-	-	2.66E-06	-
D_k	9.13E-04	-	-	8.85E-06	-

The REMPI scheme employed in these experiments excite through the umbrella mode, ν_2, where the intermediate state is $v_2 = 4$. The umbrella state can be described by a double minimum potential, an example schematic is in Figure 2.5, attributable to the two dominant conformational modes. These equilibrium geometries have the hydrogens either above or below the plane of the nitrogen perpendicular to the C_3 axis moving through the planar configuration and as a result they are mirror images of one another, for which the barrier to inversion[87] is 1769 cm^{-1}. In the planar geometry of NH_3 the vector describing the NH bond is 90° relative to the C_3 molecular symmetry axis. The minima of the potential occur when this angle is 68° and 112°. However, tunnelling between the two equilibrium geometries is possible resulting in splitting of the rotational energy levels into doublets with symmetric (+) and antisymmetric (-) components. For the lowest vibrational states, the antisymmetric state is 0.7933 cm^{-1} higher[88] in energy than the symmetric state. The energy level diagram in Figure 2.6 includes this splitting although the energy gap has been exaggerated in order for it to be discernible. The upper level of each pair corresponds to the - parity state and the lower lying state is the + contribution. However, where $k = 0$, one of each doublet is excluded due to the Pauli exclusion principle. For even values of J, the antisymmetric component is excluded, as is the symmetric component for odd values of J.

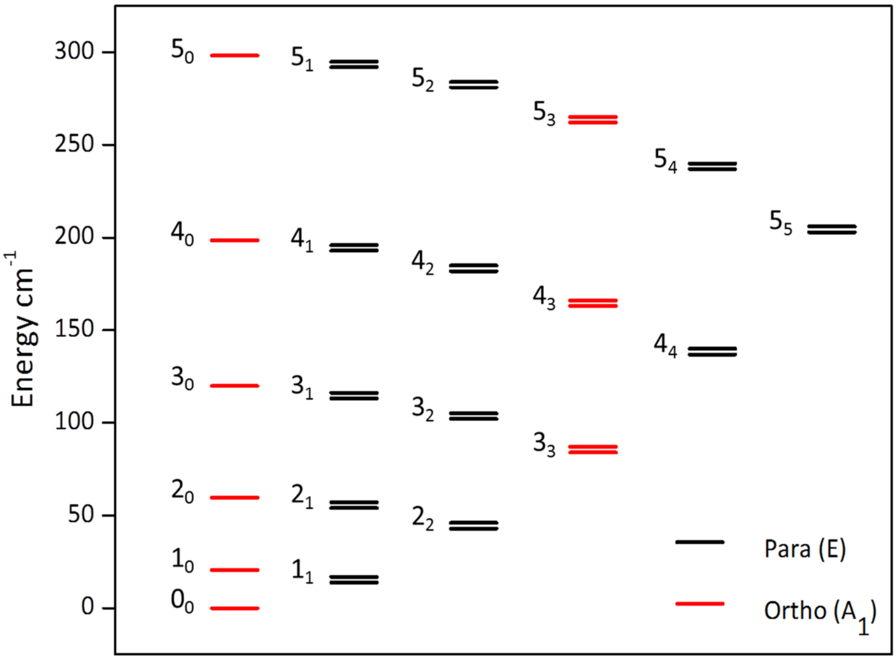

Figure 2.6 Rotational energy level diagram of the NH_3 ground vibrational state in the $\tilde{X}$ electronic state. The J_k quantum states are labelled and coloured according to their nuclear spin state. See text for symmetry assignments. The splitting of the parity states has been exaggerated for clarity.

Due to the REMPI scheme employed for these experiments only products with antisymmetric character are detected. However, it is possible to interconvert between different parities so these products will have contributions from both + and - initial states where available. This experiment does not have the capability to be initial parity state selective, it is worth noting that in experiments where this capability has been available it has been shown that for some products differing cross sections are observed.[63, 66]

As a hydrogen containing molecule, NH_3 has *ortho* and *para* nuclear spin isomers. NH_3 is a fermion as the overall nuclear spin (I) is half-integral, with ortho-NH_3 $I = 3/2$ and para-NH_3 $I = 1/2$.[89] States where $k = 0$ or a multiple of 3 are *ortho* and all other states, i.e. $k \neq 3n$, are *para*. The symmetry of the molecular energy levels are described by the C_{3v} point group, hence the *ortho* states have A_1 symmetry and *para* states have E symmetry, as noted in Figure 2.6.[90] It is not possible for the NH_3 to undergo conversion between different nuclear spin states upon rotational excitation hence the products imaged come from well-defined initial states, primarily $J_k = 0_0^+$ and $J_k = 1_1^{\pm}$. The full initial state populations are discussed in section 2.4.2. One reason for the focus on NH_3 is that it provides a closed-shell comparison to previous experiments that focussed on another symmetric top, the open-shell system, CH_3 (CD_3).[57, 62, 77] Many of the conclusions that can be drawn are qualitative in nature as these CH_3 radical experiments do not offer product k-state resolution.

2.4 Molecular beam characterisation

In order to understand the differential cross sections (DCS) of the scattering products, it is necessary to prepare the initial states of the colliders as far as possible. Minimising the distribution of initial states is desirable, as it reduces the range of rotational excitation energies and therefore the spread in the image radii. As discussed in Chapter 1.3, it is possible to achieve this using a pulsed molecular beam from a supersonic expansion because they provide a narrow range of initial velocities due to the translational and rotational cooling that occurs through numerous collisions. How these parameters are exploited for the work in this thesis is discussed below.

2.4.1 Beam velocity

The gas sample is kept at room temperature so barring any localised heating at the nozzle, this provides a starting point for calculating the beam speeds. The initial stagnation enthalpy of a system is defined as $H_0 = U_0 + p_0V_0$, where the internal energy is defined as U_0 for a given pressure (p_0) and volume (V_0). If it is assumed that this is completely converted into the translational motion, an expected beam speed for a pure gas sample can be calculated using the relationship between velocity (v) and the mass (m), the heat capacity ratio (γ), Boltzmann's constant (k_B) and the stagnation temperature of the gas prior to expansion (T_0):[22]

$$v = \sqrt{\left(\frac{2k_BT_0}{m}\right)\left(\frac{\gamma}{\gamma-1}\right)} \qquad 2.5$$

where the units of m are kg and T in K in order to calculate v in ms^{-1}. The heat capacity ratio is $\gamma = \frac{C_p}{C_v}$ where C_p is the heat capacity at constant pressure and C_v is the heat capacity at constant volume. It is dependent on the structure of the molecule, for monotomics this is $^5/_3$, diatomics $^7/_5$ and polyatomics $^4/_3$.[22] For a gas mixture m and γ are determined by the concentration of any seeded gas (C) hence they become equivalent to:

$$m_{mix} = Cm_A + (1 - C)m_B \qquad 2.6$$

$$\gamma_{mix} = C\gamma_A + (1 - C)\gamma_B \qquad 2.7$$

Table 2.2 Calculated velocities for the gas mixtures used at a temperature of 303 K.

Gas	**v (ms^{-1})**
NH_3 (3% in Ar)	568
Ar	561
D_2	2099.5
CH_4 (25% in He)	1398
C_2H_6 (25% in He)	1141
$C(CH_3)_4$ (25% in He)	807

It is not unusual for the nozzles to heat up during running which is why the predicted beam speeds were calculated for a gas temperature of 30°C which correlates to the position of the beam spots in the recorded images. The energy throughout the sample is not initially dispersed uniformly; it is through the process of supersonic expansion that it transfers primarily into translational energy modes with a narrow range of velocities. The skimmer selects the central portion of the expansion which contains the narrowest distribution of speeds all propagating in the same direction. The distribution of the velocities can be characterised by fitting the beam spot detected from ionization of unscattered NH_3. In order to characterise the secondary molecular beams within the bounds of the experimental set up, small volumes of NH_3 are leaked into the secondary gas line.

Even these trace amounts of NH_3 are easily detectable and as a result some images, particularly those with larger scattering radii, i.e Ar, CH_4 etc, contain a secondary beam spot. In those with smaller scattering radii, e.g. D_2, the beam spot may still be present but due to the high secondary beam velocity, it appears in a region beyond the area of the scattered signal in the image and is therefore not visible in the images.

The distribution of velocities observed, will affect the size of the primary NH_3 beam spot which will appear in the images at 0° and the combined effect of beam speed spread from both nozzles will result in the velocity spread in the images. This is because, as noted in Chapter 1.1.2, the initial velocities of the colliders are related to the final scattering velocity by the collision energy (equation 1.11 and equation 2.13).

2.4.2 Rotational temperature

The rotational temperature of the molecular beam can be characterised by obtaining a REMPI spectrum of the lowest *J* states of the NH_3 and fitting this with a simulation using PGOPHER,[91] shown in Figure 2.7. As mentioned in the previous section, all of the collider beams are characterised by leaking a small volume of NH_3 into the gas line allowing a REMPI spectrum to be taken to obtain an estimate of the translational temperature for atomic systems, or rotational temperature of molecular systems. This technique assumes that the NH_3 is being cooled as efficiently as the species being characterised. Ideally, the sample would be characterised by obtaining a REMPI spectrum of the species, however, this is not always experimentally feasible.

It is important to focus on the spectroscopy of the lowest *J* states because background signal builds up, due to NH_3 molecules undergoing multiple collisions with the chamber and ion optics. This occurs particularly in scattering acquired for the NH_3 and hydrocarbon beams because of the cuboid design (see Figure 2.10) that was used for these experiments. Where a bimodal rotational temperature is observed, fitting the REMPI spectrum according to the lowest few rotational *J* states is still a valid representation of the rotational temperature of the beam because the background scatter primarily affects the relative intensity of higher *J* states.

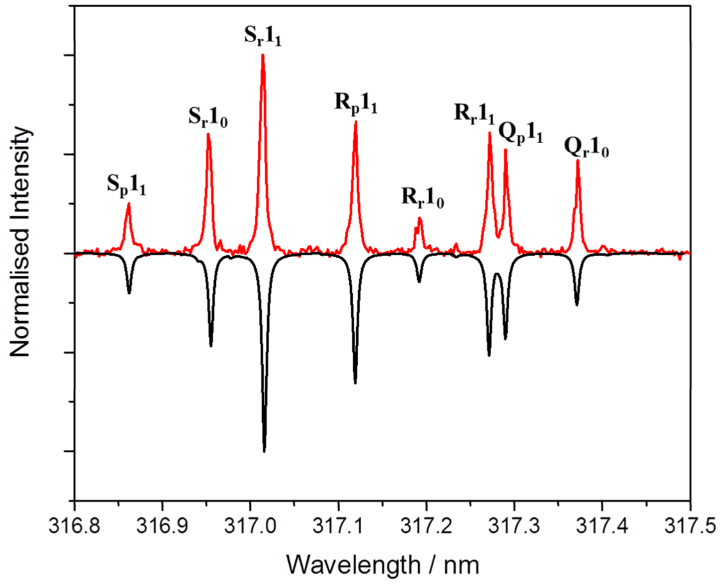

Figure 2.7 REMPI spectrum (red plot) of NH_3 (3% in 4 bar Ar) obtained between 316.8 nm and 317.5 nm. The black plot is the simulated spectrum for a temperature of 8 K.

The rotational temperature allows for the calculation of the expected initial populations of the colliders. The Boltzmann equation (equation 2.8) is used to determine the populations of the initial states that are available for excitation:

$$\frac{N_J}{N_0} = g_J \exp\left(\frac{-\Delta E_J}{k_B T}\right) \tag{2.8}$$

the degeneracy of the J_k state (g_J), ΔE_J is the energy of the rotational state relative to the ground state, and k_B and T are the Boltzmann constant and temperature respectively. The spectroscopy of NH_3 was detailed in Section 2.3.3.

Larger polyatomics have more complex rotational and vibrational spectra, the specifics of which are discussed in Chapter 5. For particularly large molecules such as neopentane measuring the rotational temperature with the NH_3 spectrum only provides an estimate of rotational temperature because it is probable that the NH_3 in the beam will be cooled more efficiently because the energy levels have greater separation between them.

Table 2.3 Rotational temperatures obtained for trace quantities of NH_3 in kelvin of the molecular beams of the gas mixtures used. Obtained as described in the text.

Gas	**T (K)**
NH_3 (3% in Ar)	8
Ar	8
D_2	9
CH_4 (25% in He)	~15
C_2H_6 (25% in He)	~20
$C(CH_3)_4$ (25% in He)	~30

Table 2.4 Rotational populations of the lowest quantum states of NH_3 at a rotational temperature of 8 K (3% NH_3 in 4 bar Ar) with the nuclear spin state of the J_k noted.

NH_3 $J_k^{\pm}$	**Population**	**Nuclear Spin State**
0_0^+	59.10%	Ortho
1_0^-	4.30%	Ortho
1_1^+	19.40%	Para
1_1^-	16.80%	Para
2_0^+	0.00%	Ortho
2_1^+	0.00%	Para
2_1^-	0.00%	Para
2_2^+	0.20%	Para
2_2^-	0.20%	Para

2.4.3 Temporal profile

The timing of the nozzle pulse for both beams can be adjusted so that the laser samples scattering products from collisions resulting from different parts of the molecular beams. The front part of the molecular beam pulse is the section of fastest moving molecules from the expansion and will have the narrowest spread of velocities and therefore the most rotationally cold molecules. The pulse timing and duration is optimised in conjunction with the timing of the laser in order to detect scattering from collisions occurring between the coldest parts of both molecular beams.

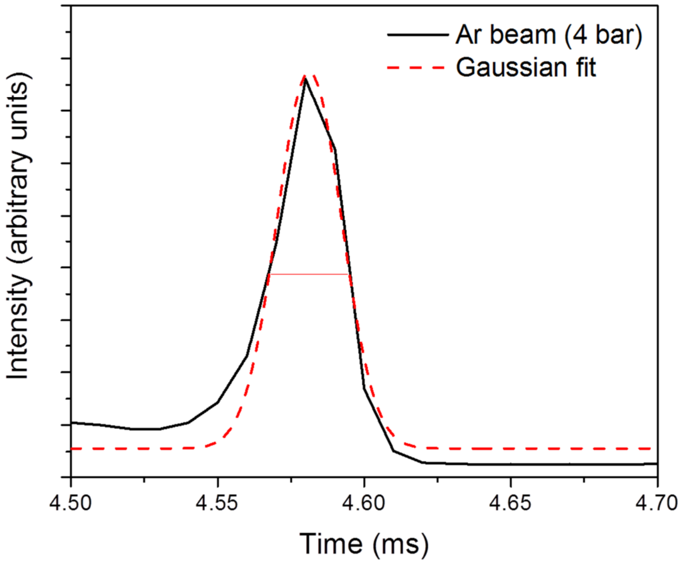

Figure 2.8 An example of the temporal distribution of the Ar molecular beam based on the intensity of the beam spot of a trace amount of NH_3 in the beam. The plot is signal vs nozzle delay time (ms) graph with the FWHM indicated for the Gaussian fit.

2.4.4 Seeding NH_3

In order to achieve the minimum number of initial states of any reagent molecules undergoing collisions producing molecular beams of gas mixtures is a necessity. Rare gases can be used in a pure state as rotational and vibrational factors do not influence these systems. It is also possible to use a pure beam of some diatomic molecules, such as H_2 and D_2, as their small size, large rotational constants and high barriers for vibrational excitation lead to effective collisional cooling. However, for larger polyatomic molecules, it is necessary to consider how suitable rotational cooling will be achieved. Such molecules will have initial populations in a greater number of, and higher lying, rotational states due to the spacing between energy levels being much closer for these molecules. The larger size of the molecules will result in a lower density of molecules upon expansion meaning fewer collisions and therefore less efficient energetic cooling.

In order to create the number of collisions in the expansion required to efficiently reduce the range of rovibrational states in the molecular beam it is necessary to seed the molecule of interest in a carrier gas, generally an atomic system. This also reduces the tendency for the molecules to form clusters when subjected to the high backing pressures. Clusters are problematic because they reduce the number of available molecules of interest, therefore reducing the number of collisions of interest. When cluster formation occurs in the primary beam, then the molecules may still be ionised through multiphoton processes, however, they will be separated according to mass by their relative time of flight so will not affect the images due to the use of DC slice imaging, see section 2.6.1. If cluster formation occurs in the expansion of the secondary beam it is more problematic as it results in additional collisions between the NH_3 and the clusters. Scattering from these additional cluster collisions would be detected, as these NH_3 molecules can be ionised, increasing the background signal.

To achieve the cooling required for NH_3 it is seeded at a 3% mix in 4 bar of pure Ar for these experiments. Although seeding reduces the number of molecules available for detection from the collision of interest this is also considered one of its advantages because the high ionization efficiency of NH_3 means that the number of ions produced at a higher concentration would result in saturation of the detector. If saturation was not a risk, then the recorded data would be of little use for extracting the dynamical information because the increased range of initial states due to less effective cooling that the resulting image would very blurred. There would also be higher concentration of unscattered molecules available for ionization which would interfere to a greater degree with the images in the angles that describe the very forwards scattering angles e.g. $\theta = 0$ - 30°.

2.4.5 Seeding polyatomic colliders

Besides encouraging rotational cooling, seeding offers control over molecular beam characteristics such as the speed, as discussed in section 2.4.1, so it is possible to tune these using the carrier gas. Using different noble gases or mixtures of noble gases will produce particular results depending on their characteristics, as the mass and the heat capacity ratio of the mixture governs the beam velocity as described in equation 2.5. For a gas mixture, if the ratio favours the carrier gas then the characteristics of the beam will be dominated by it, due to the relationships in equations 2.6 and 2.7. This means seeding is advantageous for very bulky molecules e.g. neopentane, for more than just rotational cooling because the larger the total mass of the system the slower the beam speed. Due to the relationship in equation 1.11, the result is a low collision energy which would make comparing the various collision systems difficult as the range of energies used across the experiments would be very different. Seeding in an atomic system means that the parameters are weighted towards the smaller particle, which results in high beam speed and therefore a higher collision energy and a narrower range

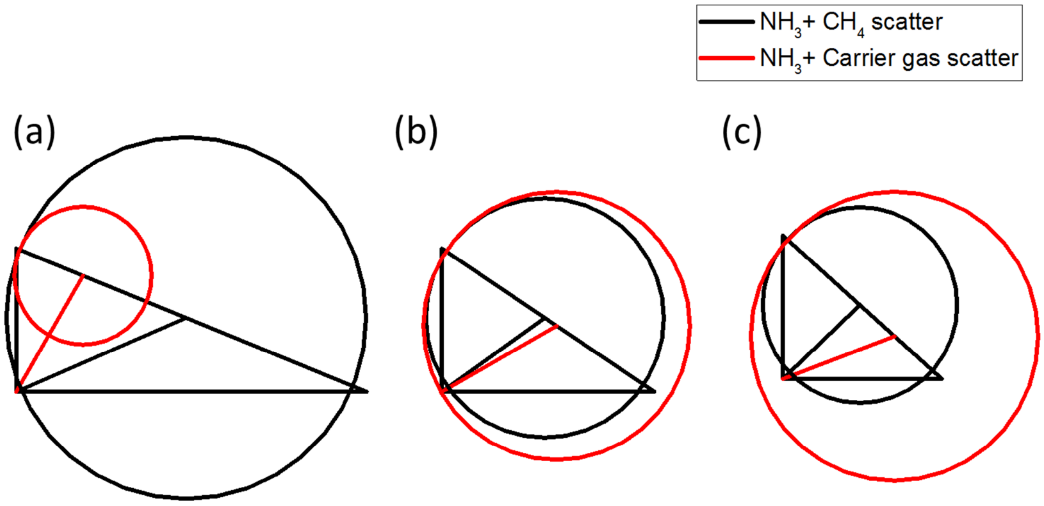

Figure 2.9 Newton diagrams with predicted scattering ring pairs for the collisions of NH_3 with CH_4 (black lines) seeded at a concentration of 25% in a) He, b) Ne and c) Ar (red lines). The initial NH_3 velocity is along the positive vertical axis, and the seeded CH4 velocity is along the horizontal axis. The variation in v_{CM} is also indicated in the corresponding colours.

of collision energies. As a consequence of this, the differences between scattering of NH_3 can be assigned to the dynamics of the collisions and are not the result of the variation in the collision energies between the collider systems.

In previous work, a polyatomic, e.g. NH_3 or CD_3 has been seeded in a carrier gas, Ar, and collided with a second beam of pure gas, for example He, Ar or H_2.[62, 77, 78, 92] This is common practice in research utilising molecular beams. The work describe herein is interested in the dynamics of collisions between two polyatomic molecules which requires both colliders of interest to be seeded in a carrier gas. In addition to the advantages mentioned above, the reduction in image definition caused by one beam being ineffectively cooled would be enhanced when both beams are not sufficiently rotationally cold. The range of internal energies would result in a spread of total energies as well as numerous collisional excitation pathways caused by simultaneous excitation (or de-excitation) of the collider molecule, all of which would cause a detected single NH_3 product state to exhibit a multitude of velocities. This would produce data that it would be difficult to extract useful information from.

The requirement for seeding of the secondary beam has resulted in the experimental images becoming more complex. This is because, despite both types of particle in the secondary beam experiencing the same environment, the dependency of collision energy (E_{coll}) on the reduced mass of the colliders (equation 1.11) means that for each collision pair, the NH_3 experiences a different collision energy and therefore will scatter at a different velocity. The scattered ions from the collisions between the NH_3 and the secondary beam carrier gas are generated simultaneously with those resulting from the bimolecular collision and this ion packet experiences the same VMI conditions and so arrives at the detector at the same time as the ion packet of interest. This results in the second ring appearing in the experimental images. Figure 2.9 demonstrates the relationships between the calculated radii of NH_3-CH_4 scattering and NH_3-rare gas scattering and Table 2.5 compares the same selection of carrier gases with other hydrocarbons relevant to this work. The calculation of expected scattering rings sizes is discussed later in Section 2.7.

Table 2.5 Expected scattering radii in pixels of the $J_k = 2_2$ product state of NH_3 resulting from collisions with the hydrocarbon colliders and the possible carrier gases. The difference in scattering radii in pixels is indicated in the final column.

Collider mixture		Collider (pixel)	Carrier (pixel)	Δpixel
25% in He	CH_4	60.2	22.9	37.3
	C_2H_6	66.9	19.0	47.9
	$C(CH_3)_4$	65.2	13.9	51.3
25% in Ne	CH_4	39.8	44.6	4.8
	C_2H_6	49.8	41.9	7.9
	$C(CH_3)_4$	56.2	36.9	19.3
25% in Ar	CH_4	32.6	48.1	15.5
	C_2H_6	42.3	46.7	4.4
	$C(CH_3)_4$	50.7	43.6	7.1

The added complexity of the images means the carrier gas of the secondary beam has to be considered carefully because if the characteristics of this secondary collision system are close to that of the system of interest then the 2 rings will overlap and the information gained will be inseparable. There will always be some overlap in the most forward scattering angles because $\theta = 0°$ will be the same point on the detector for both systems, where the same type of collision is occurring for NH_3 i.e. no contribution to the internal energy from the collision partner. However, the degree of this overlap is determined by the ratio of the radii of the 2 rings. The overlapping region must be subtracted from the raw images of the bimolecular collisions before analysis, the methodology for this is discussed in detail in Chapter 5. This is not as disadvantageous as it initially seems as it is often necessary to disregard up to the first 20° of the image hemisphere because the beam spot of unscattered NH_3 in this region renders this section of the ring unreliable.

2.5 Single-collision conditions

Experiments used to investigate collisions need to be conducted under 'single collision' conditions to ensure that the data reflects the nascent products which can then be directly correlated to the information known about the parent molecules. If allowed to occur, the energy exchange processes that are experienced through multiple collisions result in the alteration of the energy distribution of the detected products, thus removing the connection between them and the parent molecules. It also becomes impossible to tell how many collisions a particle has undergone and therefore the exact nature of the energy exchange processes it has experienced. In the case of inelastic collisions it specifically removes the connection to the initial collision event by both altering the velocity and internal energy distribution of the detected species rendering the information obtained unusable. In collisions resulting in reactions, multiple collisions may result in the formation of additional products resulting in a misleading enhancement or depletion of the primary product's detection probability. The necessary conditions can be achieved by controlling the collision frequency through spatial isolation i.e. increase the mean distance travelled between collisions; and temporal isolation i.e. ensuring the time between collisions is longer than the period of detection.

Maintaining temporal isolation is achieved by ensuring that the timing of the ionisation laser is such that it arrives directly after the collision has occurred so that the nascent product is ionized. As discussed in Chapter 1.2, it is assumed that the ejection of an electron has a negligible effect on the particle's velocity and internal energy distribution. The pulse length of the ionization laser is also very short (few nanoseconds) whilst the time of flight is on the order of a few microseconds so collisions in the drift region are also highly unlikely.

The average distance travelled between successive collisions by a molecule is known as the mean free path (*l*). It is a property that is influenced by the number of molecules present within the volume of the apparatus. The relationship is described by:

$$l = \frac{k_B T}{\sqrt{2}\sigma p} \qquad 2.9$$

where p is the pressure and σ is the collisional cross section which can be estimated from the van der Waals radius (r) of an atom or the bond lengths of the molecule as $\sigma = 4\pi r^2$.

The distance from the point of initial collision to the detector is 66 cm and providing that l is greater than this then the conditions for spatial isolation are satisfied. An example for a two-nozzle experiment with an operating pressure of 1 x10^{-5} mbar and respective van der Waals radii for He and Ar of 1.40 x10^{-10} m and 1.88 x10^{-10} m,[93] therefore results in l = 11.81 m for He and 6.55 m for Ar respectively. This clearly satisfies the aforementioned condition of being greater than the distance travelled to the detector. If the experiments are conducted in low pressure conditions then this results in a larger l. However, this is an average value for the apparatus and it is important to ensure that there is particular focus on maintaining these conditions in the collision region. A modification was made to the chamber to make certain that this was the case because the much higher local pressure in the collision volume results in a considerably smaller mean free path, however, this is much harder to estimate as the exact pressure in this region is unknown. The central cuboid, as described in its initial design[72] and as used for the Ar and small hydrocarbon experiments had solid walls except holes for the lasers on the corners and 2 holes directly opposite the molecular beams to allow for the

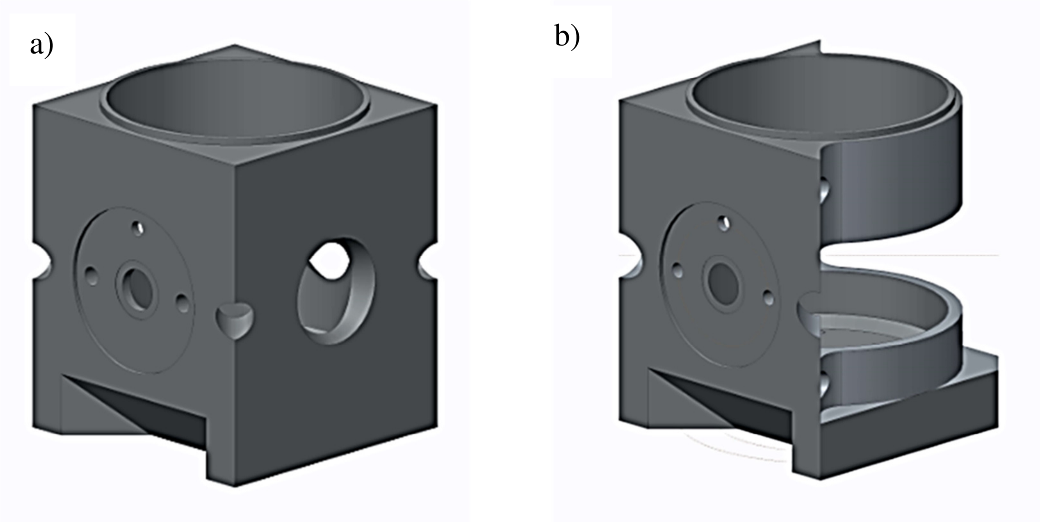

Figure 2.10 Side 3-D views of the central cuboids including the skimmer mounting point for one molecular beam on the left where a) is the old design in use for NH_3+ Ar and Hydrocarbons scattering experiments and b) the replacement design used for the NH_3+D_2 experiments.

gas to be pumped away directly (see Figure 2.10a). The enclosed nature of this cuboid led to background signal in the experimental images with this particularly observed in the hydrocarbon images due to the requirement of seeding the hydrocarbons in He, which the turbomolecular pumps are less efficient at removing. Although the background image subtraction removes most of this noise, a new design was required to minimise it further. The new cuboid was designed by Dr David Hadden and it was exchanged prior to the commencement of the D_2 experiments, which is the only set of data affected by this modification. The new cuboid is less enclosed in order to promote the removal of the gas in the collision region (Figure 2.10b).

2.6 Velocity map imaging

VMI is an imaging technique that uses inhomogeneous electric fields in order to focus the ions according to their velocity on to the position sensitive detector. The specifics of how this is achieved are discussed in greater detail in Chapter 1.2. In order to achieve the velocity mapping conditions a stack of electrodes are required to generate the necessary electric fields, the collision/ionization region is situated within the electrode stack so that the nascent ions can be accelerated immediately towards the detector. As the electric fields have a focussing effect on the particles, the electrodes can be described as lenses hence the term ion optics is often used as a description. In this experimental apparatus, the ion optics stack consists of the repeller and extractor between which two stabiliser electrodes are located, and then a further 16 electrodes which have an electric gradient applied over them with the final one grounded. The repeller and extractor accelerate the ions from the collision region for which the electric fields are stabilised by a pair of intermediate electrodes. 4 further electrodes act as a lens to focus the ions according to their velocity. The remaining 12 electrodes are then used to provide a gradual and linear gradient down to ground to homogenously accelerate the ion packet. The design, shown in Figure 2.11, is adapted from that which was developed by Lin *et al.*[19] and has been intended for use with direct current (DC) slice imaging[17]

2.6.1 DC slice imaging

Post-collision the inelastically scattered products will have a new velocity and as these collisions are occurring in 3-D space the scattering from the centre of mass will form an ion cloud that is spherical in nature with different probabilities of scattering to each point on the sphere's surface. Therefore the scattered particles will have angular components of both θ, the angle in the plane of the detector and φ, the azimuthal angle. Although the image would have the cylindrical symmetry, which is a key factor in 'standard' VMI, the distribution of the scattering would be spherical resulting in a blurred image from which it would be very difficult to extract dynamical information as discussed in more detail in Chapter 1.2. In order to overcome this direct current (DC) slice imaging is used.[17] A gentle electric field gradient and lower voltages are used (see Table 2.6) instead of the high voltages and steep gradients that are used to compress the Newton sphere. A short voltage pulse (~30 ns) is then applied to the rear MCP so only the ions impacting the detector during the pulse are recorded. The timing of the pulse is optimised to the arrival of the centre of the ion sphere on the detector, as shown in Figure 2.12. The 2-D slice that is recorded produces an image that is directly correlated to the velocity, removing the requirement for complex forward convolution methods to obtain the DCS as mentioned in Chapter 1.2 although there are density-to-flux issues that need to be accounted for, the method for which is described later in Section 2.8.

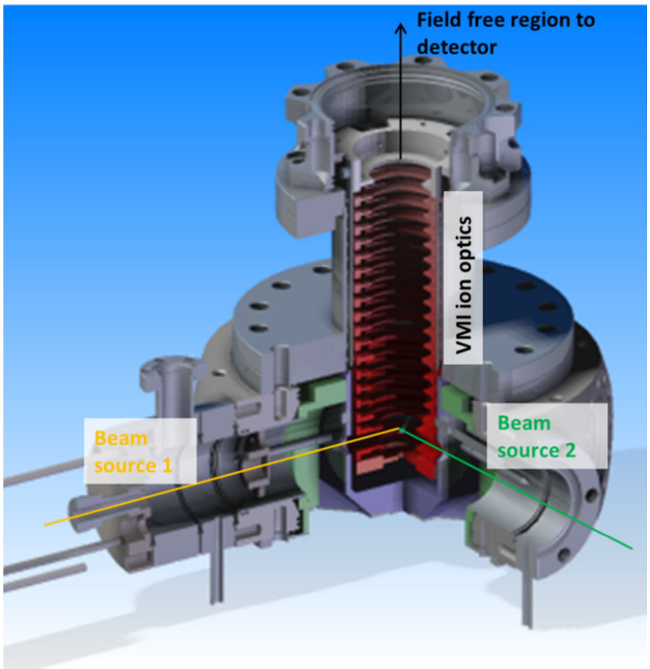

Figure 2.11 Side view with a cut through the main chamber including the ion optics stack. Beam source 1 (orange) is the NH_3 beam and beam source 2 (green) is the collider beam.

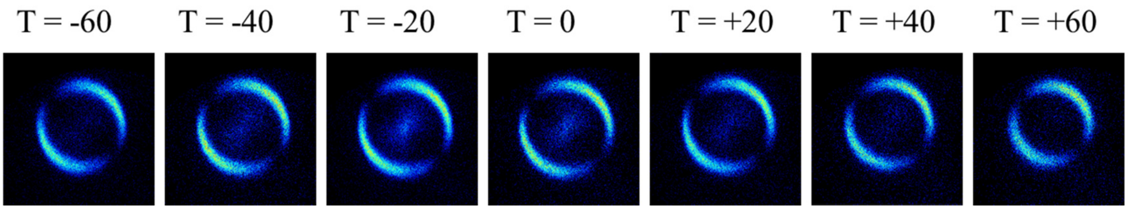

Figure 2.12 CD_3I photodissociation DC slice images obtained at different times (in μs) for the slice with respect to the centre of the ion cloud (*T* = 0). The laser wavelength was 310.6 nm to detect I* via (2+1) REMPI.

Table 2.6 Voltages used for the ion optics, electrodes named where appropriate. The voltage on electrode H is then divided by a resistor change as described in text.

Electrode	**Voltage (V)**
Repeller (A)	1000
Stabiliser 1 (B)	971
Stabiliser 2 (C)	931
Extractor (D)	911
Electrode E	888
Electrode F	867
Electrode G	846
Electrode H	824

In standard VMI all ion hits are imaged regardless of their time of arrival. The possibility of the detection of multiple mass channels introduces a dimension of noise from background molecules and can be problematic in all types of VMI experiments. These background species, such as carrier gases or colliders, may be ionised by non-resonant multiphoton processes. This introduces “noise” to the images additional to the background created by the molecule of interest that is not involved in the collisional process of interest. The pulse of the detector is timed in order to provide mass gating over a particular subset of the ions. Providing that the field conditions do not cause the ion clouds of background ions to overlap in time with the slice being imaged, other mass channels should not be detectable.

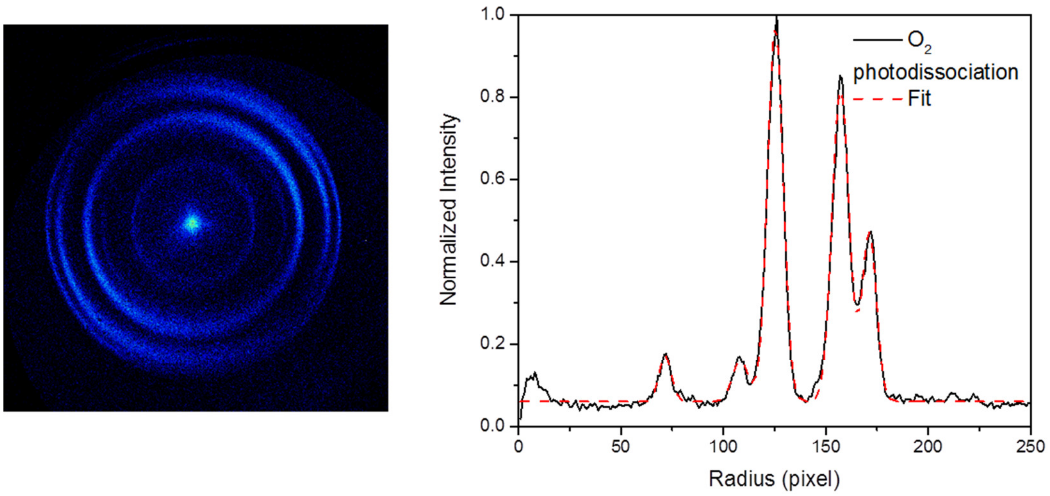

Figure 2.13 20 ns slice image of O_2 photodissociation at 224.99 nm and its corresponding intensity vs pixel radius plot.

2.7 Velocity Calibration

After transferring the experimental set up from Bristol to Heriot-Watt it was necessary to reassess the calibration of the detector. The ideal method of doing this is to detect $O(^3P)$ from the photodissociation of O_2, at 224.99 nm which excites via the $3d\pi(^3\Sigma^-_{1g})$ Rydberg state of O_2. The image of O^+ consists of many distinct rings caused by a wide range of well described product pathways.[15, 19] The dissociation energies of these product pathways have been calculated and from the relationship described later in equation 2.12 it is possible to calculate the expected velocities of each ring. The observed radius of the photodissociation ring of a known velocity allows for the calculation of a velocity per pixel calibration factor for the experimental setup.

From this an initial calibration factor, F_1, for O was found to be 12.3 m s^{-1}/pixel. This is related to the mass of the experimentally detected species by the relationship:-

$$F_2 = \left(\sqrt{\frac{m_1}{m_2}}\right) F_1 \qquad 2.10$$

where F_2 is the calibration for the experimental species and m_2 is its mass. F_1 is the initial calibration factor and m_1 is the mass of the calibration species i.e. 16 for O.

As the O_2 calibration is dependent on wavelengths in the UV whilst the NH_3 ionization is achieved at longer wavelengths closer to the visible region, an alternative method of providing occasional verification of the calibration during the experimental time period

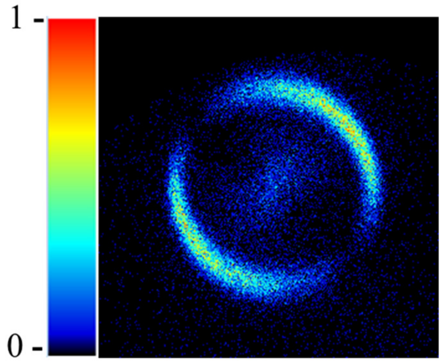

Figure 2.14 CD_3I calibration image of the photodissociation product, I*, at 310.6 nm.

was required to remove the necessity of changing the laser dye and the internal alignment of the dye laser. The system used is the photodissociation of CD_3I through the A-band,[94] using a (2+1) REMPI scheme at 310.6 nm to detect the I* $^2P_{1/2}$ photofragments, as in Figure 2.14. The photodissociation of CD_3I produces a single ring with a scattering velocity of 352.7 ms^{-1}.

Once the calibration factor has been determined, the expected scattering ring sizes can be calculated. The collision energy is extrapolated from the velocities of the molecular beams. Likewise the scattering velocities of the products (v_n'') can be derived from the translational energy available for partitioning after any transfer into internal modes has been accounted for by;

$$E_{scatt} = E_{coll} - \Delta E_{int} \qquad 2.11$$

The energy available for scattering (E_{scatt}) can be used in equation 2.12 to calculate the total scattering velocity (v_{scatt}).

$$v_{scatt} = \sqrt{\frac{2E_{scatt}}{\mu}} \qquad 2.12$$

This can then be partitioned according to the mass of particles involved in the collision (m_A and m_B):

$$v_1'' = v_{scatt}\left(\frac{m_2}{m_1+m_2}\right) \qquad 2.13$$

The scattering velocity of a molecule (v_A'') can then be divided through by F_2 (equation 2.10) to find the expected scattering radius in pixels. It is important to note that for the systems involving multiple scattering rings, as discussed in Section 2.4.5, there will be different collision energies due to the dependency on the reduced mass of the colliding particles.

It is important to note that as E_{scatt} is dependent on ΔE_{int} which must account for any internal excitation of both of the colliders. As the experiments are state selectively detecting the NH_3, the initial and final J_k states are known and therefore the rotational excitation energy is well defined. However, for molecular colliders it is also possible for co-excitation occur. All of the molecules used in this thesis have rotational levels that are energetically accessible at the collision energies in use. The distributions of the energy levels in these molecules are discussed in the corresponding chapters as are the difficulties in identifying the transitions that are occurring. However, as the image radius is dependent on E_{scatt}, for which the NH_3 contribution to ΔE_{int} is known then any deviation from the expected image radius allows for the calculation of the change in internal energy of the collider. Any excitation of the collider will result in a smaller than expected scattering ring because there will be less translational energy available. Any rotational cooling of collider molecules that are initially in higher quantum states will result in larger rings than predicted as this converts additional energy into kinetic energy.

2.8 Density-to-flux conversion

For a collision occurring in the centre-of-mass (CM) frame (Figure 2.15a) the resulting scatter should generate a symmetrical image about the relative velocity (v_{rel}) with differing scattering probabilities for the angular component of the velocity. However, the images obtained experimentally are not symmetrical as can be seen in Figure 2.15b. This is a consequence of the difference of the velocities in the lab frame (v'_{NH3}, v''_{NH3}) to the corresponding CM frame velocity (u'_{NH3}) of molecules that are scattered at the same speed but with opposing angular components in the centre of mass frame for example +100° and -100° (+ clockwise from 0°, - anticlockwise from 0°) (Figure 2.15a).

The images are measurements of the CM frame DCS, however, the collisions take place in the lab frame. The centre of the image, i.e. the CM, is the point at which the lab frame v_{CM} intersects v_{rel} as shown in the Newton diagram. The CM frame velocity is described by u_n which is related to the lab frame velocity by equation 1.8. Post-collision the molecule has a new CM velocity, u_n', and it is necessary to consider how this acts on the molecule in the lab frame. As an example scattering to -100° can be

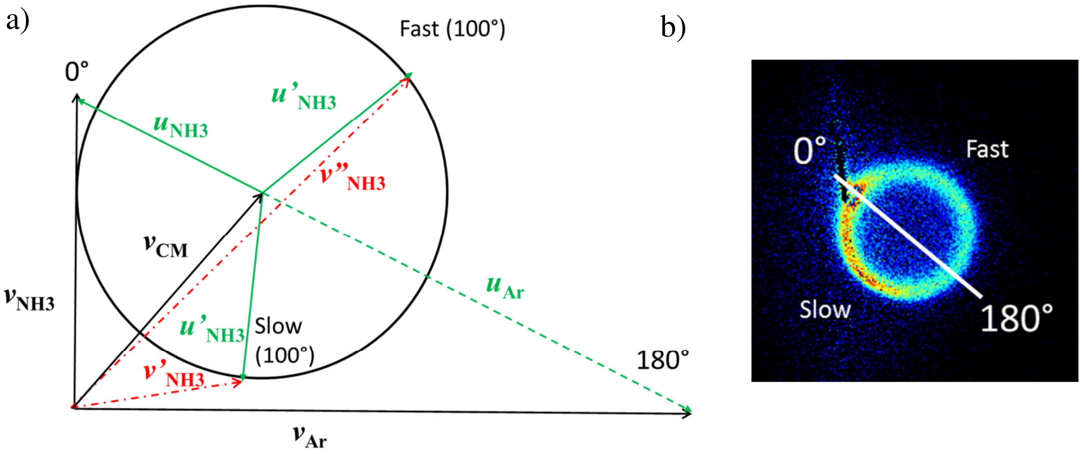

Figure 2.15 Lab frame to Centre of Mass frame transformation for inelastic scattering of NH_3 with Ar where a) is a Newton diagram describing the scattering system, including the vectors for products scatter into θ = ±100° relative to the CM and b) experimental image for the $J_k = 3_0$ product state that exhibits a strong detection bias on the slow side.

described by $v_1' = v_{CM} - u'$. In contrast molecules detected in the other half of the DCS, are moving at a much higher lab frame velocity i.e. $v_1' = v_{CM} + u'$.[1]

Since collisions are continually happening, a build-up of the 'slow' lab frame molecules in the ionization region occurs in addition to a depletion of the molecules that have a 'fast' lab frame velocity. This detection bias is attributable to the difference in the duration of the gas pulses (μs) compared to the detection time (ns). The longer time spent in the ionization region by the slower moving particles means that there is an increased density of these when the laser pulse arrives, this results in a higher detection probability of these molecules. The lifetime of the faster moving molecules in the ionisation volume is much shorter, some will have moved out of the ionisation region prior to the arrival of the laser pulse reducing the number of molecules available for detection. This causes a bias in the intensities of the images due to these two types of lab frame product, resulting in the asymmetry that is apparent. Hence the images represent an experimental number density (N_{lab} (θ, v)) rather than the true flux of particles formed (F_{CM} (θ, u)). The relationship of which is described by:[1]

$$N_{lab}(\theta, v) = F_{CM}(\theta, u)\frac{v}{u^2} \qquad 2.14$$

In order to overcome this detection bias and extract the DCS, $\frac{d\sigma}{d\omega}(\theta)$ it is necessary to simulate an angle-dependent instrument function. As the experimental image is proportional to the number density, it is related to the DCS through the instrument function:

$$N_{image}(\theta) = \frac{d\sigma}{d\omega}(\theta) G_{instrument}(\theta) \tag{2.15}$$

The experimental image can then be divided by the simulated image of the instrument function to extract the DCS. The details of how the instrument function is generated are discussed below.

2.8.1 Dealing with density to flux conversion

To simulate the instrument function for the apparatus, a Monte Carlo method is used to simulate a range of trajectories for each molecular beam and to determine the probabilities of collision and subsequent detection using a Fortran 77 program developed by Mark Brouard and Chris Eyles [95] and adapted for this experimental setup by Ondrej Tkáč.[72] Further amendments have been made to the program particularly for the use of two diatomic/polyatomic molecular beams. The program requires the input of numerous parameters that characterise both molecular beams and the laser, it also requires an input controlling the number of successful trajectories that are required to run, typically this is set to $3 \mathrm{x} 10^7$.

In order to simulate collisions of the molecules of interest it is necessary to describe the molecular beams in detail. The types of parameter required for each of the molecular beams are the same. The initial set describes the final rotational level ($J'_{k'}$) and the initial state (J_k) as well as the rotational constants B and C of the molecule being detected. The program uses equation 2.16 to calculate the change in rotational energy, ΔE_{rot} for the primary beam:

$$\Delta E_{rot} = hc\left(\left(BJ(J+1) + (C-B)k^2\right) - \left(BJ'(J'+1) + (C-B)k'^2\right)\right) \tag{2.16}$$

For a secondary beam containing a diatomic or a polyatomic the rotational constants, initial and final states can be included where appropriate. Using these constants for the secondary beam allows for the adjustment of the scattering energy if co-excitation of the collider is observed with 2.17 with the appropriate rotational constants and states, or E_{rot2} is the same equation as 2.16, depending on whether the collider molecule is spherical/diatomic or symmetric top respectively. The rotational constants for the molecules in use are included in Table 2.1.

$$\Delta E_{rot2} = hc\left(\left(BJ(J+1)\right) - \left(BJ'(J'+1)\right)\right) \qquad 2.17$$

The characterisation of the molecular beams continues with further description of the molecules of interest. The mass and the beam velocities are given for the two colliders in order for the calculation of E_{coll}, using equation 1.11. The total remaining translational energy (E_{trans}) can then be found:

$$E_{trans} = E_{coll} - \Delta E_{rot} - \Delta E_{rot2} \qquad 2.18$$

The parameters of the collision trajectories used to generate an instrument function are sampled over a range of velocities, angular divergences of the molecular beam in the collision region, spatial widths of the molecular beam and possible collision times. The values for all of these parameters are randomly selected from the Gaussian distributions calculated based on the full width half maxima (FWHMs) that are given as inputs to the program. The FWHMs are extracted from the characterisation of the beam spots described in Section 2.4 used to characterise the molecular beams. The angular divergence after the skimmer of both beams is 3.2° and the spatial width of the collision centre is 3.5 mm. The FWHMs of the velocities obtained from the beam spots can be found in Table 2.7. The collision times were randomly generated based on the FWHMs of the temporal distribution of the molecular beams (Figure 2.8) and are also included in Table 2.7. This provides a description of the Gaussian distribution of the gas pulse. A probability of collision is then determined based on the combination of these parameters for the trajectories of the two particles.

Table 2.7 Table of parameters used to describe the FWHM of the molecular beams velocity and temporal distributions in the Monte Carlo Simulation program.

Gas	**FWHM v (m s^{-1})**	**FWHM t (μs)**
NH_3 (3% in Ar)	145	86
Ar	60	27
D_2	250	50
CH_4 (25% in He)	270	105
C_2H_6 (25% in He)	275	105
$C(CH_3)_4$ (25% in He)	235	105

It is then necessary to calculate the probability of detection by the laser once a collision has been found to have a chance of occurring for the given set of parameters. This is any trajectory calculated to have a collisional probability > 0. A description of the ionization volume is therefore required; the program inputs for the laser characterization are the beam waist (w_0) and the Rayleigh range (Z_r). The beam waist is calculated from the wavelength (λ) and the focal length of the lens (f) used. For all experiments a 250 mm lens was used, and its wavelength dependent focal length was calculated for use in the simulation.

The limiting factor used to determine the probability of detection along the axis of laser propagation is $\pm Z_r$ as this is the point at which the cross-sectional area doubles, i.e. the radius of the beam increases to $\sqrt{2}w_0$. The beam radius (w_Z) at a given point along the axis of laser propagation (z) between w_0 and Z_r can be calculated by:

$$w_Z = w_0\sqrt{1 + (\frac{z}{Z_r})^2} \qquad 2.19$$

The beam intensity can be approximated by a Gaussian distribution along the laser propagation axis where the focal point is the peak of the curve i.e. the highest density of photons. If the density of photons is not sufficient then the probability of a multiphoton process, such as REMPI, occurring is reduced. It is also necessary to consider the radial intensity of the beam – the intensity across the axes around the centre-line of the beam. The radial intensity of the laser can also be described by a Gaussian distribution in fact w_0 is the width at which the intensity has decreased to $1/e^2$ of the Gaussian peak value. This is why $2w_Z$ is considered the point at which the intensity is negligible and insufficient for ionization to occur and is therefore used as the radial bounds for detection probability. It is therefore possible to weight the probability of detection

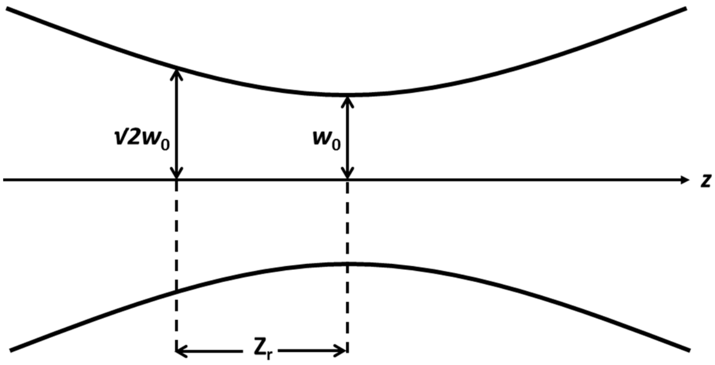

Figure 2.16 Pictorial description of the focal region of the laser i.e. the ionization volume.

based on the overall intensity using the relationship expressed in following equation:

$$I_{z,r} = I_0\left(\frac{w_0}{w_z}\right)^2 \exp\left(-\frac{2r^2}{w_z{}^2}\right) \qquad 2.20$$

From which the probability of detection can be extracted as:

$$P_{det} = \exp\left(-\frac{2r^2}{w_z{}^2}\right) \qquad 2.21$$

Multiple simulations are run to include the necessary initial states of the NH_3 (generally 2, see Table 2.4) which can then be weighted according to the percentage populations of the initial state in the molecular beam and summed. For collisions where the collider is excited it is also necessary to apply a weighting to this post-simulation. As the probabilities of excitation are unknown this has led to several solutions, depending upon what was appropriate for the situation. This includes the application of forward convolution techniques. The techniques used will be more fully described in Chapter 4 and Chapter 5.

2.9 Image analysis

In order to complete the analysis of the experimental images, the angular distributions need to be extracted. This was achieved using a LabView program written by Dr David Hadden. The program converts the Cartesian coordinates of the 3-D image array into a triangular polar pixel array centred around a given set of *x, y* coordinates. Coordinates are assigned to the centre of the scattering ring, the exact values of which can be adjusted to account for the slight drift in the experimental image position on the detector that occurs due to environmental factors, such as the daily nozzle operating temperature for example. The array is therefore a plot of pixel radius vs the number of pixels at that radius.

From this, two pieces of information are obtained. The intensity vs. radius plot is obtained for the entire image, where intensity is the sum of the intensities of all of the pixels at a given radius relative to the centre coordinates. This provides a useful check on the actual scattering ring size in comparison to the predicted ring size calculated according to the description in section 2.7.

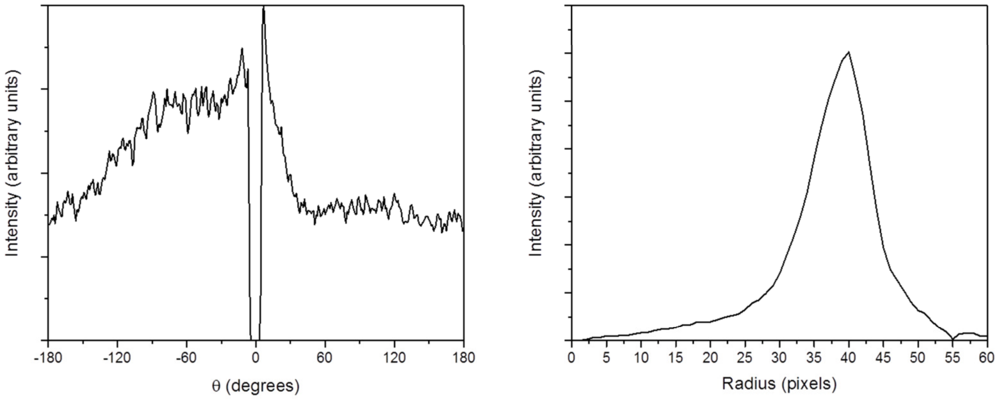

Figure 2.17 Example of a) raw angular distribution, where $\theta = 0$ to -180° corresponds to the lab frame "slow" side and b) the velocity distribution for NH_3 product state $J_k = 3_0$ from the inelastic collisions of NH_3 with Ar.

The second piece of information that is obtained from the triangular polar array is the angular distribution of the scattering relative to the centre coordinates which produces a plot of intensity vs. angle, θ. An angular distribution is extracted for each individual pixel radius by assigning the intensity to each degree bin. These plots obtained are then used to generate a mean angular distribution for $\theta = -180$ to 180°. In order to minimise the influence of background noise on the final angular distribution, a radius range is selected. This range is chosen according to the width of the scattering ring and is therefore also adjustable to the radius appropriate for the product state being detected. The assignment of $\theta = 0°$ of the angular distribution can also be adjusted so that it is equivalent to the angular position of the unscattered NH_3 experimental image by applying an appropriate offset.

Working from the triangular array allows for more flexibility in order to extract the angular distribution for appropriate regions of the image. It allows for the removal of the more intense regions in the most forward scattering angles caused by unscattered NH_3. Despite subtraction of the majority of the beam spot using the simultaneously recorded background image, this additional intensity arises from inaccurate centroiding of the beam spot in some of the experimental images. The subtraction is achieved by positioning a wedge of zeroed pixels across an angular section. The size of the angular range is dependent on the scattering system and is centred at $\theta = 0°$ for that image. This wedge subtraction is also used to remove additional scatter from collisions between NH_3 and the carrier gas that appears in the images of the NH_3-hydrocarbon collisions.

It is the angular distributions of the experimental data and the instrument functions that are used in equation 2.15, in order to obtain the DCSs. The angular distributions from are normalised by area prior to the extraction of the DCS for a particular J_k state. This is to allow for the intensities of individual experimental datasets on a comparable scale. The resulting DCS is then averaged over the lab frame "slow" and "fast" hemispheres in order to account for minor discrepancies resulting from pixilation. In order to calculate a final DCS for each product state that reflects multiple experimental datasets, a weighted mean is produced based on the intensities of the contributing experimental images. Any alterations to this methodology are noted in the individual chapters.

The following chapters contain a description and discussion of the results of the experiments that have been discussed in this chapter.

Chapter 3 – Ammonia + Argon

3.1 Background

3.1.1 NH_3 + noble gases

Ammonia has faced intense scrutiny in recent years due to its presence in the interstellar medium (ISM) and the use of its spectroscopy as a guide for the temperature of the regions it is detected in.[90] The spectroscopic data obtained has shown NH_3 to be warmer than would be expected if at thermal equilibrium in these regions,[96] suggesting that it is undergoing frequent energy exchange with surrounding species. In order to understand these temperature discrepancies it is first necessary to understand the nature of these energy transfer processes. Inelastic collisions have been thoroughly investigated for small molecular species focussing primarily on diatomic systems [41, 97] with a gradual shift towards larger systems colliding with monoatomic gas species[61] as detailed more fully in Chapter 1.4. Although Ar is not a common species in the ISM, understanding the trends that appear as the nature of the potential energy surfaces (PES) evolves with the size of the collider allows sensible predictions to be made about the collisional behaviour of species that are more challenging to investigate experimentally. Investigating Ar collisions also provides a comparison to smaller and more well-studied species such as He[57, 64, 65, 71] and Ne[70] allowing for confirmation that trends observed can be assigned to the changing nature of the PES.

Previous work has investigated the inelastic collisions of NH_3 and ND_3 with a range of collision partners. The experimental and theoretical work that has studied the collisions of these species with He[28, 64, 71] demonstrate strong correlation between differential cross sections obtained experimentally and through quantum scattering calculations. The picture that emerges from this type of collision is of a PES that is dominated by repulsive interactions, resulting in a high proportion of side and backwards scattering in the differential cross sections (DCSs) as the degree of rotational excitation, ΔJ, of the detected species, i.e. NH_3/ND_3 increases. Investigations by Chandler's group[70] of inelastic scattering of ND_3 with Ne as the collider have occurred, although this system has not been as rigorously studied as He. The work with Ne demonstrates that repulsive interactions still hold sway over the collisional dynamics at the energies studied although to a lesser extent than with He.

The focus of this chapter is velocity map imaging (VMI) of the inelastic scattering of NH_3 + Ar, which has received less attention than its deuterated analogue. In the early 1990s, Meyer used counter propagating beams to investigate high energy collisions of NH_3 with monatomic gases including Ar[68, 69] and He.[64, 65] Due to the nature of the experimental set up, the collision energies for these systems were 1274 cm^{-1} and 1130 cm^{-1} respectively. The results from the work by Meyer are discussed in more depth in relation to the data obtained for this chapter later on.

At collision energies of 410 and 360 cm^{-1}, which are more relevant to the experiments described herein, and utilising both crossed molecular beam (CMB) and VMI techniques, are the experiments detailed by Tkáč et al.[66] investigating ND_3 + Ar. These focus primarily on experiments offering initial state selection of the ND_3 through the use of a hexapole. The initial state selection of $J_k^{\varepsilon} = 1_1^-$ results in only images of the ND_3 final states with E nuclear spin symmetry being recorded and so the focus of the discussion is on the effect that parity preserving or parity inverting collisions have on the DCSs and a comparison of the parity pairs of the same final J_k states. However, due to the initial state selection only part of the story is described because there is little data obtained to describe the nature of the scattering of other symmetry products, which in the case of ND_3 are A_1, A_2 and $k = 3n$ ($k \neq 0$) product states which have contributions from both A symmetry states. Although the experiments described in this chapter lose some resolution due to contributions from two initial states for each *ortho* (A_1) or *para* (E) final state, it is possible to compare the nature of the scattering into the product states with different nuclear spin symmetry. The populations of the initial states of NH_3 in the molecular beam can be found in Table 2.4. Each nuclear spin state is dominated by population in a single initial J_k state, 0_0 and 1_1 for ortho and para respectively. It is valid to assume that the images are dominated by collisions originating in these states. Therefore the resulting DCSs can be used to provide an assessment of the scattering into *ortho*/*para* rotationally excited states from the two ground initial states.

The theoretical investigation[71, 98, 99] of the PES of the NH_3 (ND_3) + Ar system shows a deeper attractive well than that which is calculated for the He system. This shifts the collisions towards a more attractive dominated potential, resulting in the expectation that a higher proportion of forward scatter will be observed in the experimental DCSs of NH_3 + Ar and of larger impact parameters dominating the collisions, in comparison to scattering with smaller noble gases, e.g. He and Ne. This trend has so far been upheld by experimental data obtained for ND_3 with these 3 systems.[63, 66, 70, 74] Scattering resonances are also predicted by theory for the NH_3 + Ar system,[74] however, these are not observable under the collision regime described in this work because there is insufficient experimental resolution.

3.1.2 Ar + other polyatomics

As discussed in Chapter 1 collisions involving polyatomics have not been investigated as thoroughly as smaller molecules, particularly diatomics, and there are only a few examples of work conducted between polyatomics and Ar beyond those mentioned above in conjunction with ND_3. Nesbitt and co-workers[54] have used a CMB apparatus to investigate H_2O + Ar with transient infrared absorption spectroscopy to establish the scattering propensities and to test the quality of the PES. Other work which is more relevant to that discussed in this chapter, are the investigations into CD_3 + Ar.[77] The open shell symmetric top, methyl radical provides a comparison to the closed shell symmetric top of NH_3. Qualitative observations can be made about the nature of the collisions and their interaction potentials which can then be compared as has been done for ND_3 and CD_3 with He.[57] The data obtained for this chapter was collected on the same apparatus as the methyl data found in reference 79; as such both sets of experiments have been evaluated in relation to each other in more depth later on.

3.2 Results

3.2.1 Velocity Map Images

Images have been recorded for NH_3 product states where a single J_k state is spectroscopically accessible with little or no overlap by other nearby REMPI transitions from other rotational levels. The collision energy studied in these experiments is 318 ± 37 cm^{-1}. The energy level diagram showing the required change in internal energy to access the antisymmetric rotational levels of NH_3 from the relevant initial state is in Figure 3.1, which displays the states that can be accessed within the experimental collision energy. As can be seen only rotational states up to $J_k = 6_5$ (304 cm^{-1} from $1_1^{\pm}$), are energetically accessible assuming that the excitation is from the lowest lying initial state. It does not necessarily follow that it is possible to image all states; for example, in the case of $J = 1$ states, images are not attempted because the high population of these states in the molecular beam, particularly $J_k = 1_1^{\pm}$ as pointed out in Table 2.4, the signal from the molecular beam creates so much background that detecting scattered signal is almost impossible. Alternatively, this can be due to the lack of available isolated REMPI transitions for a state, such as $J_k = 5_4$, or may be due to a lower product population in these states as found for $J_k = 5_0$. A low population of a product state may be caused by several factors, such as a small integral collisional cross section. It is also possible that a state may have low detection probability due to a low ionization efficiency. As discussed in Chapter 2.3.3 only the antisymmetric product states are detected at the wavelength range in use, as a result where J is an even number, $k = 0$ does not exist in the antisymmetric state as explained in further detail in Chapter 2.3.3.

The background subtracted experimental images are presented in Figure 3.2 for the inelastic scattering of NH_3-Ar for a selection of NH_3 product states $J = 2$ to 5, $k = 0$ to 5 as appropriate and where accessible. These images are displayed in a grid according to increasing J down the columns and k across the rows. There is a dark irregular shaped spot in the experimental images in Figure 3.2 at $\theta = 0°$ due to the subtraction of the beam spot which is comprised of unscattered NH_3. In some images a second bright beam spot, which is not subtracted, also appears in the backwards direction. This is due to trace amounts of NH_3 in the secondary beam that was used for characterisation of the beam and timing optimization.

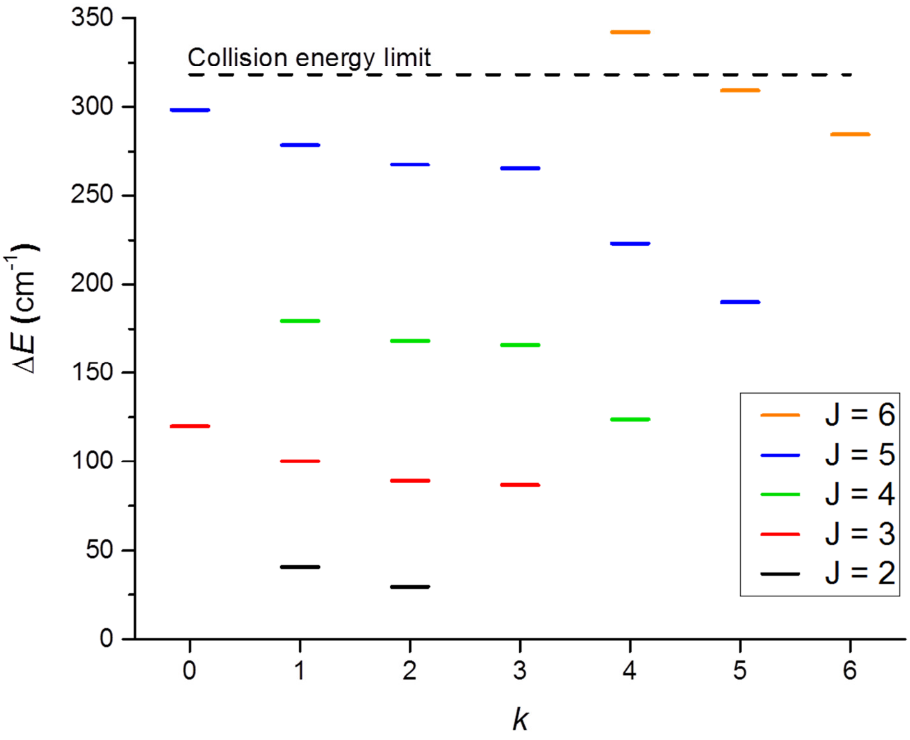

Figure 3.1 Energy diagram demonstrating the energies required for the collisional excitation of NH_3. The initial state for all *ortho* transitions (k = 0, 3n) is $J_k = 0_0^+$ and the initial state for all *para* transitions ($k \neq 3n$) is $J_k = 1_1^{\pm}$.

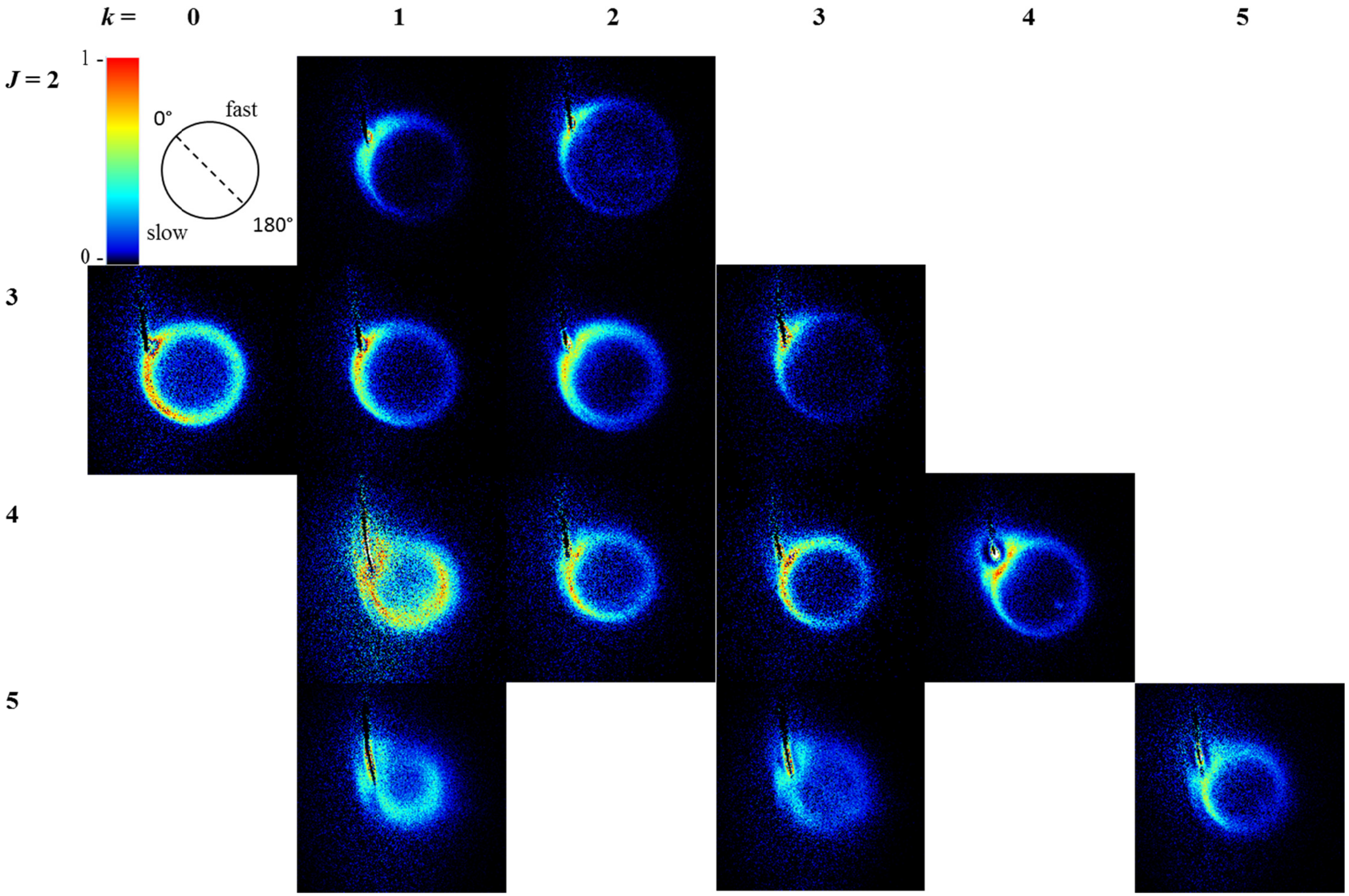

Figure 3.2 Velocity map images of the inelastic scattering of NH_3-Ar at a collision energy of 318 ± 37 cm^{-1}. The images are arranged according to *J* down the columns, and increasing *k* across the rows. The top left panel shows the intensity colour scale and orientation of the scattering ring with θ.

The raw images show some evidence for the trends that are discussed later with respect to the extracted DCSs; however, there is a large intensity discrepancy in the images between the slow and fast sides as a result of the detection bias as discussed in Section 2.8. The images in the $J = 3$ series, particularly $J_k = 3_0$ demonstrate this bias particularly clearly. Unlike later chapters which require more consideration of the final states of the collider species in conjunction with the final state of the NH_3, collisions with atomic Ar requires a simpler method of image analysis. The simulated instrument function is used to correct the experimental images using the relationship described by equation 2.15 with some scaling introduced to adjust the instrument function as at times this over predicts the bias in the slow side resulting in overcompensation by the density to flux conversion. The methods for the instrument function simulation are fully described in Chapter 2.8.1. After correction a DCS can then be extracted from each image.

3.2.2 Differential Cross Sections

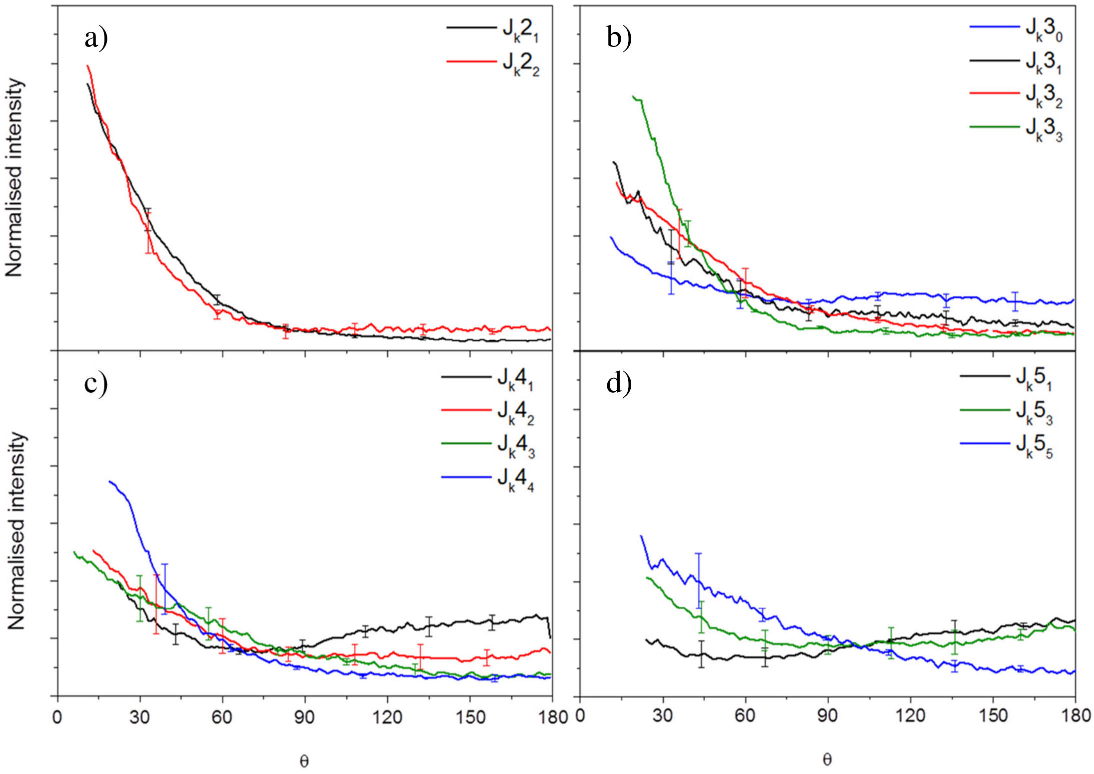

Figure 3.3 DCSs for the NH_3 product states for the collision of NH_3-Ar a) $J = 2$, $k = 1,2$ b) $J = 3$, $k = 0 – 3$ c) $J = 4$, $k = 1 – 4$ d) $J = 5$, $k = 1, 3, 5$. Obtained at a collision energy of 318 ± 37 cm^{-1}.

The DCSs of the states imaged are presented in Figure 3.3, they are a mean average obtained from processing multiple experimental images in the following way. A density-to-flux corrected DCS is extracted for each single experimental image over a scattering angle range of θ = -180° to 180° as described in Chapter 2.9. Each half of the DCS, relative to $\theta = 0°$, describes the slow (negative/anticlockwise) or fast (positive/clockwise) lab frame hemispheres of the DCSs. The density-to-flux corrected DCS should be symmetrical about $\theta = 0°$ but in reality there can be slight discrepancies between each side due to the pixelated nature of the images and simulations. To account for these minor inconsistencies, an average of the two halves is taken to produce a single DCS describing scattering from $\theta = 0°$ to 180° for a single dataset (Figure 3.4a).

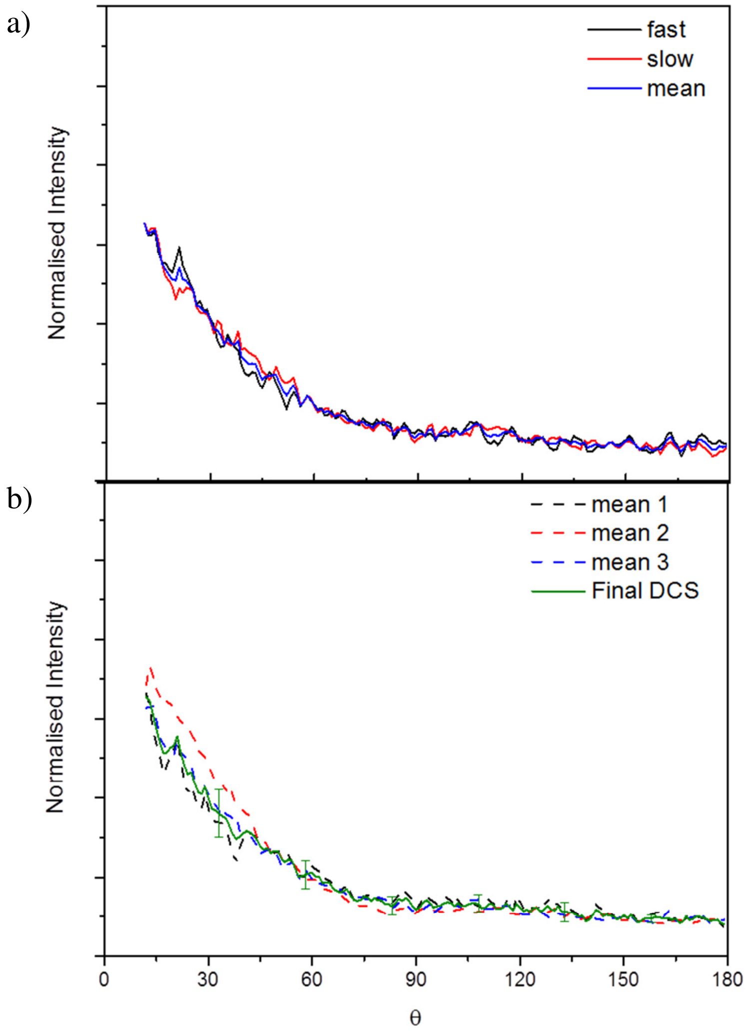

Figure 3.4 Example plots for J_k = 3_1 a) of slow/fast/mean of a single experimental dataset and b) of the fast/slow means of multiple datasets and the overall weighted mean DCS for the product state.

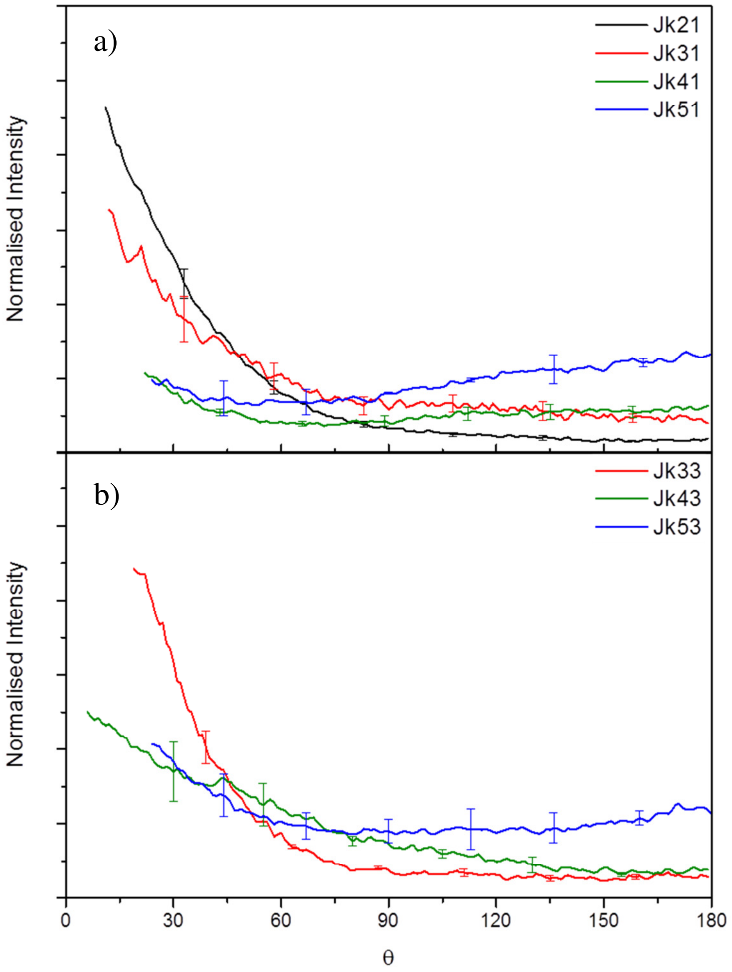

Figure 3.5 Plots for single k product states demonstrating the increase in the range of scattering angles as J increases a) $k = 1$, $J = 2 - 5$ and b) $k = 3$, $J = 3 - 5$.

The overall DCSs displayed in Figure 3.3 for each individual product state, is the mean average of the datasets that are available for that J_k state, the contribution of each dataset is weighted according to the total intensity of the experimental image (Figure 3.4b). The error bars describe the contributions from both averaging the two halves of each experimental image and the error introduced from taking a mean of multiple experimentally derived DCSs . The error introduced from the mean of the two halves of an individual dataset is the difference of one half from the average, see equation 3.1 and the overall error is the root mean square of these values as described by equation 3.2.

$$i = x - \bar{x} \tag{3.1}$$

$$error = \sqrt{\frac{1}{n}\left({i_1}^2 + {i_2}^2 + \cdots\right)} \tag{3.2}$$

The DCSs in Figure 3.3 show that the majority of scattering is in the forward direction with the highest proportion of all scattering appearing at angles less than 60° for the $J \leq 4$ states. In contrast, the $J = 5$ states present scattering into a much wider range of angles and a shift towards a backwards ($\theta = 120$ - $180°$) dominated scattering regime as can be discerned in the DCS of $J_k = 5_1$. As J increases, the amount of scatter into angles greater than 60° also increases as would be expected due to the increase in torque required to generate the higher energy rotational states which results in a greater deflection from the original direction of motion, this is sometimes referred to as the rotational rainbow.[1] This is most clearly demonstrated when comparing the DCSs for $J = 2 – 5$ in $k = 1$, see Figure 3.5a, and $J = 3 – 5$ in $k = 3$, Figure 3.5b. The other k states do not have sufficient datasets to allow a similar comparison, due to a lack of suitable spectroscopic transitions, see Section 3.2.1.

There is a second trend within the DCSs from the same initial J state which can be observed clearly in all graphs included in Figure 3.3; there is a tendency for the amount of scatter that is sideways and backwards in nature to decrease as k increases. Although seen in the DCSs across all J_k series, the $J = 5$ rotational states' DCSs (Figure 3.3d) demonstrate a considerably wider range of angles than is observed for other rotational states, with $k = 5$ showing considerable sideways scatter ($\theta = 60 – 120°$) whilst $k = 1$ and 3 demonstrate significant proportions of backwards scatter ($\theta = 120 – 180°$) with $k = 1$ in particular being dominated by the backward scattering angles. As it was not possible to image all the k states in this series, the change in the nature of the scattering across the k states appears to be more dramatic than others. It is not as simple as it initially appears to simply describe this as a trend that is fully attributable to the value of k, the reasons for which is discussed in more detail below.

3.3 Discussion

3.3.1 Comparison to existing NH_3-Ar

The DCSs of the NH_3 + Ar system are dominated by forward scatter as described above. However, there are discrepancies in the shape of certain DCSs such as the $J_k = 3_0$ and 3_1 states with respect to previous reports.[69, 71] Past experimental DCSs reported demonstrate a significant shoulder from 0° to ≈ 45° in $J_k = 3_1$ and between ≈ 60° and 90° for $J_k = 3_0$, although it is worth noting that this is for the symmetric state in contrast to the antisymmetric state recorded herein. These discrepancies can be accounted for by the difference in orientation of the molecular beams in the experimental set up used and by the significant difference in collision energy, i.e. 1274 vs 318 cm^{-1}, as this is likely to alter the dynamics considerably. In the same theoretical comparison paper by van der Sanden et al.[71] that provides calculated DCSs that support the conclusions of Meyer, there is an additional section that includes the theoretical DCSs for collisions at 485 cm^{-1} which is a collision energy that is comparable to that used herein. These theoretical DCSs demonstrate the energy dependence suggested above, moreover the experimental DCS for $J_k = 3_0^-$ in this thesis exhibits a resemblance to the calculated DCS for $J_k = 3_0^+$ in said paper. Other states also display comparable angular distributions to those calculated, although the theoretical DCSs are not available for all the states obtained experimentally. Overall the maxima and the shoulders observed in the high energy theoretical and experimental DCSs have practically vanished at the lower theoretical collision energy used suggesting that at the experimental collision energy studied here they will be even less distinguishable.

It is worth noting that this is the first reporting of experimental scattering DCSs for this collision system for $J_k = 5_1$, 5_3 and 5_5, and for all states for this collision energy. Qualitative comparisons can be made with previous data for $J_k = 5_5$ which appears to have a similar profile to those recorded for ND_3 + Ar.[66] In the NH_3 work herein there does appear to be more scattering into a wider range of angles that is more analogous to the theoretical data presented in the ND_3 work than the experimental DCS. The enhancement of these angles in comparison to ND_3 scatter is primarily due to NH_3 being lighter than its deuterated equivalent. As this work detects both parity conserving and parity inverting collisions due to lack of initial state selection, it is also possible this contributes to the differences observed in a minor way. This is because the ND_3 work found that considerable differences are observed between DCSs of the same final J_k state depending upon if they have been formed through parity inversion or conservation.

Although it is difficult to compare the scattering of NH_3 and ND_3 due to the variances in the spectroscopy that result from the isotopic differences it is possible to make qualitative comparisons. In a brief aside within the ND_3 + Ar work by Tkáč et al.,[66] there is a small section with images that were obtained without invoking initial state selection. This makes the scattering more comparable to what is observed in this work as there is no parity state selection except in detection. The DCSs appear to be somewhat more forward scattered than the NH_3 equivalents presented in this thesis. This section of the paper also displays both *ortho* and *para* final states unlike the rest of the paper which is focussed on *para* only. The DCSs reported appear to display the trend across *k*, that is previously mentioned in Section 3.2.2, for $J = 2$ and 3 states which remains unremarked upon by the authors.[66] This correlates with what has been observed in this thesis for rotational quantum states up to $J = 5$.

3.3.2 Differences within J-states

This work sees evidence for what initially appears to be a trend across *k* within the *J* states that has not been previously discussed, however, there does appear to be evidence for it within the work of other groups.[66, 70] The trend observed is a decrease in sideways scatter as *k* increases. Beyond the data presented herein this also appears to apply to work done by Kay et al.[70] on ND_3 + Ne inelastic scattering although it is not discussed by the authors. It is harder to discern than in the NH_3 work studied here as they present, for the most part, only a single image from each rotational quantum state. It does appear to be visible in the DCSs for the *k* levels for the lower rotational quantum states $J = 2$ and 3 for which multiple states are included.

Despite the evidence for this trend in *k* there is some difficulty in pinpointing the cause of it precisely. It could be directly related to the amount of energy required for excitation as with the observed trend for increasing *J*, decreasing *k* is related to increase in rotational energy change. However, if it was this simple then different J_k states with similar energy changes would look more alike. A particular example of this not being the case is $J_k = 3_0^-$ & 4_4^- which have collisional excitation energies from their respective initial states of 120 and 123 cm^{-1}, see Figure 3.1. As can be observed by comparing across Figure 3.3b and c, these two DCSs are very different which suggests that energetics alone is a much too simplistic explanation and there are other dynamic factors influencing the nature of the scattering into each *k* state.

Table 3.1 Parameters describing the collisional excitations for *ortho* transitions observed in this dataset including the nature of the transition. $\Delta J \Delta k$, the resultant energy difference, ΔE, and change in angle of the angular momentum vector, $\Delta\omega$**.**

Ortho transitions	$\Delta J \Delta k$	ΔE (cm^{-1})	$\Delta\omega$ (°)
$0_0 \rightarrow 3_0$	3_0	119.97	0
$0_0 \rightarrow 3_3$	3_3	86.66	-60
$0_0 \rightarrow 4_3$	4_3	166.09	-42.1
$0_0 \rightarrow 5_3$	5_3	265.23	-33.2

Table 3.2 Parameters describing the collisional excitations for *para* transitions observed in this dataset including the nature of the transition $\Delta J \Delta k$, the resultant energy difference ΔE, and change in angle of the angular momentum vector $\Delta\omega$.

Para transitions	**$\Delta J \Delta k$**	**ΔE (cm^{-1})**	**$\Delta\omega$ (°)**
$1_1 \rightarrow 2_1$	1_0	40.54	20.9
$1_1 \rightarrow 2_2$	1_1	29.41	-9.7
$1_1 \rightarrow 3_1$	2_0	100.10	28.2
$1_1 \rightarrow 3_2$	2_1	89.01	9.7
$1_1 \rightarrow 4_1$	3_0	179.44	32.1
$1_1 \rightarrow 4_2$	3_1	168.38	18.4
$1_1 \rightarrow 4_4$	3_3	123.99	-18.4
$1_1 \rightarrow 5_1$	4_0	278.4515	34.5
$1_1 \rightarrow 5_5$	4_4	189.914	-20.9

Taking the example described above, 3_0^- and 4_4^-, in spite of their similar excitation energy have a number of differing characteristics. As discussed in Section 2.3.3, $J_k = 3_0$ is an *ortho* state and as such the scattering into 3_0^- originates from 0_0^+ or 1_0^- which results in a $\Delta k = 0$ excitation. In contrast $J_k = 4_4$ is a *para* state starting in $1_1^{\pm}$ or $2_2^{\pm}$ which means that there are contributions possibly from $\Delta k = +2$ or +3 collisional excitations. A range of ΔJ and Δk combinations within a product J state are possible as a result of the restrictions created by the nuclear spin state of initial NH_3 state, as shown in Table 3.1 which shows the parameters for *ortho* excitations and Table 3.2 which includes those for *para* transitions, therefore suggesting that the collisional excitations are not responsible for this trend in k. Despite this, the possibility that the collisional transitions do influence the shape of the DCS to some degree is discussed later in this chapter.

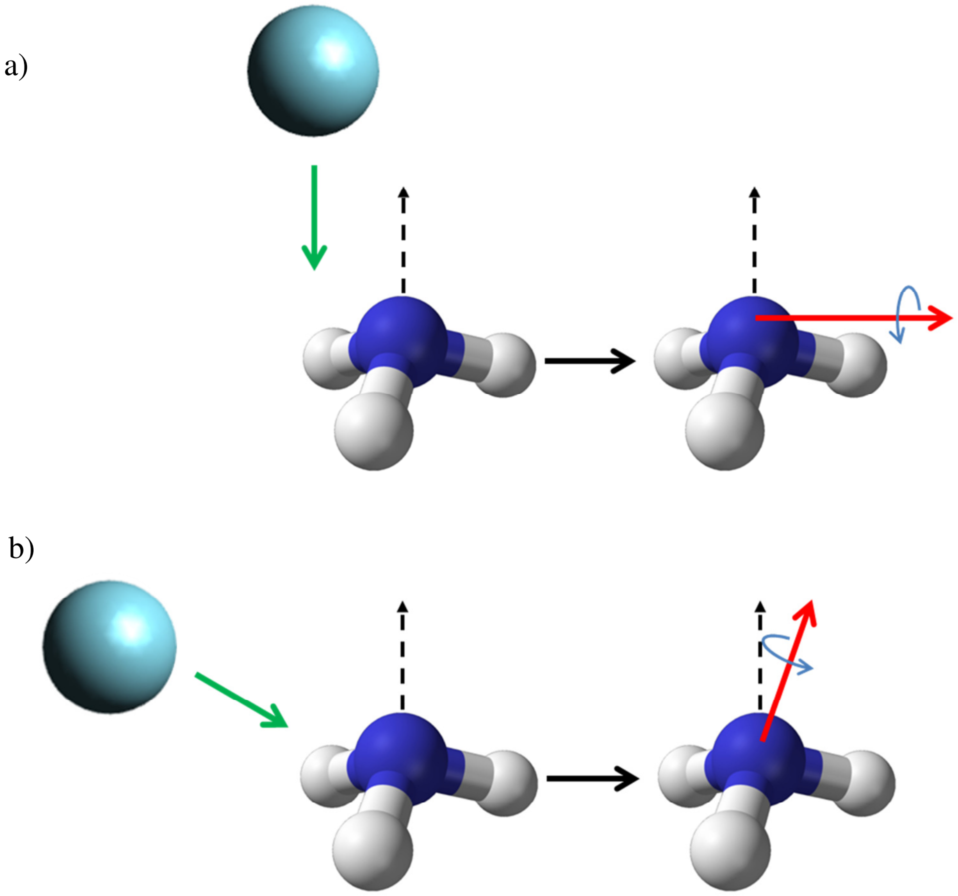

Figure 3.6 Angles of approach for NH_3-Ar for extreme collision excitation examples a) *J* only excitation; $0_0 \rightarrow 3_0$ b) *J*=*k* excitation; $0_0 \rightarrow 3_3$, described in further detail in the text.

In focussing on the collisional excitations involved, one can consider the nature of the collision in a purely classical sense by looking at the direction of approach of the colliding molecules when modelled as hard spheres. The extremes of the direction of approach can be considered with respect to the primary axis of the NH_3 as shown in Figure 3.6. In order to promote the rotational state of a molecule into a higher *J* state whilst inducing rotation perpendicular to the primary molecular axis ($k = 0$) (see Figure 2.3), the direction of approach of the collider would be parallel to the primary axis as demonstrated in Figure 3.6a. In contrast, to promote rotation into the maximum value of $k = J$, the direction of approach of the collider would be perpendicular to primary molecular axis as shown in Figure 3.6b. As discussed in Chapter 2.3.3, *J* will never be fully parallel to the molecular axis, thus the collision angle required for this rotational excitation will never be completely perpendicular. Within the experimental data the excitation of 0_0 to 3_0 demonstrates the product of a collision along the primary

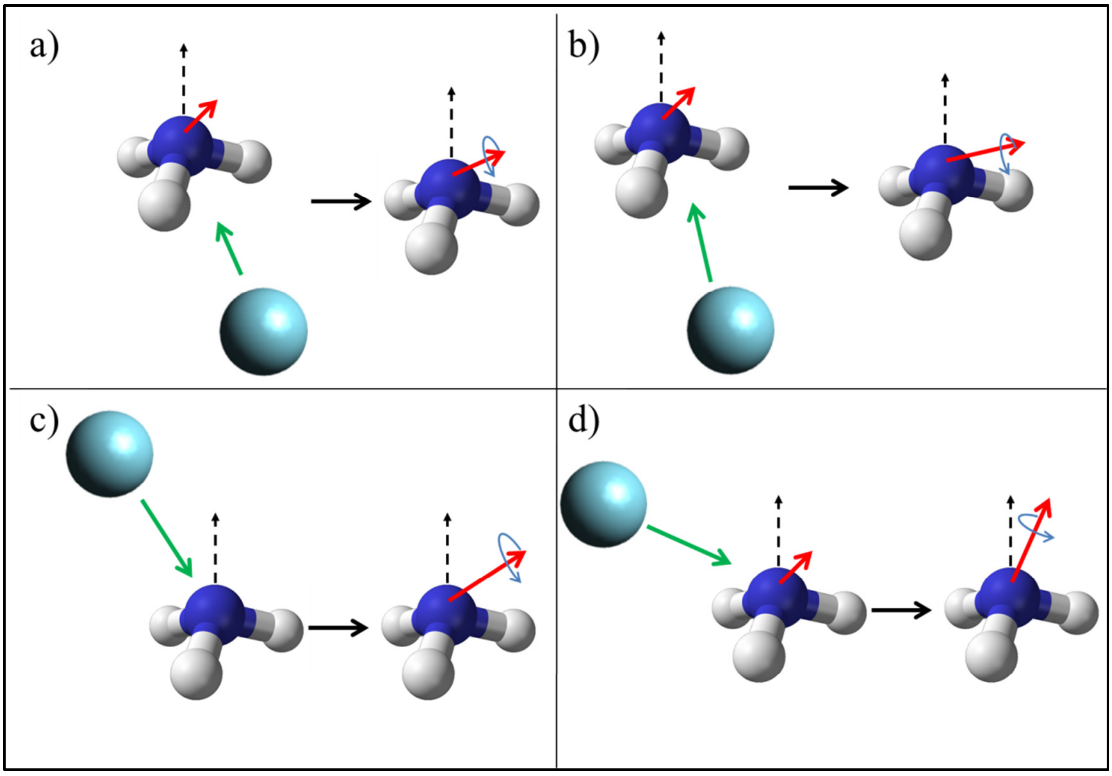

Figure 3.7 Examples of the angles of approach for Ar to excite an NH_3 in a given initial state into a given final state a) $1_1 \rightarrow 2_1$ b) $1_1 \rightarrow 4_1$ c) $0_0 \rightarrow 5_3$ and d) $1_1 \rightarrow 5_5$

molecular axis as in Figure 3.6a, and 0_0 to 3_3 is an example of the near perpendicular approach as in Figure 3.6b.

The examples of the extremes given above are both *ortho*-NH_3 states, the most drastic change comes from the rotational ground state hence only *ortho* states are accessible. The other scattered states come from a *para* initial state, $J_k = 1_1$, and as such demonstrate a range of intermediate directions of approach because of this, see Figure 3.7 for some examples. There are no trends within these that correlate with the trend observed within k, suggesting that this is not something that can be explained simply or in purely classical terms. Due to the nature of the particles involved in the collisions being described in this chapter, particularly their size, it is likely that quantum effects still have a part to play in the collisions and therefore the scattering. So far the majority of theoretical DCSs have been derived for the deuterated analogue as discussed in Section 3.3.1. Some work for NH_3 does exist, however, the calculations exploring the PES of the NH_3 + Ar system are guided by the available experimental data and as such the collision energies used are relevant to the work by Meyer.[69] The techniques used by theoreticians have also evolved since the bulk of calculations were made in the 1990's as has knowledge and understanding of the PESs, but these have principally been applied to very low energy collisions in order to investigate the nature of scattering resonances in those regimes.[74] As such there are very little direct comparisons that can be made between our work and theoretical DCSs for this exact collisional system in the literature.

Referring back to the wide range of collisional characteristics observed in these experiments, see Table 3.1 and Table 3.2, there are also examples that suggest the type of excitation occurring upon collision may be a contributing factor to the DCS unrelated to the trends observed across *k*-states. Similarities appear in the DCSs of collisional transitions such as $J_k = 3_3^- \leftarrow 0_0^+$ and $4_4^- \leftarrow 1_1^\pm$ where the excitation for both is $\Delta J_k = 3_3$. This seems to occur despite these two collisional excitations having different excitation energies, separated by ~37 cm^{-1} and varying directions of approach in a classical model of the respective collisions, as in Figure 3.7. As can be seen in Figure 3.3, the DCSs show resemblances with a slight increase in higher scattering angles in $J_k = 4_4^-$ as befits the trend seen with increasing *J* previously described. In spite of a difference in excitation energy of ~60 cm^{-1}, similar comparisons can be drawn between the DCSs of $J_k = 3_0^- \leftarrow 0_0^+$ and $4_1^- \leftarrow 1_1^\pm$, for which the excitation is $\Delta J_k = 3_0$. However, as these are the only 2 sets of data demonstrating the same collisional transitions, it is difficult to make a definitive argument for how the transition contributes, but they would suggest that it can be considered an influence on the shape of the DCS irrespective of the nuclear spin state of the scattered molecules.

3.3.3 Comparison of NH_3-Ar with CD_3-Ar

The inelastic scattering of CD_3-Ar has previously been investigated on the same experimental apparatus,[77] comparing that data with this work provides a base for drawing conclusions as to how the electronic configuration may affect the dynamics of a collision using an example of open shell (CD_3) and closed shell (NH_3) systems. There is difficulty in making direct comparisons between the methyl and ammonia systems due to the lack of *k* state resolution in CD_3 detection; however, it is still possible to draw qualitative conclusions between the two. The CD_3-Ar experiments were conducted at a collision energy of 330 cm^{-1}, the data reveals a very forward dominated process with the scattering restricted to angles $\leq 60°$, with the majority into $\theta \leq 45°$ even up to $J = 5$. This contrasts with the wider range of scattering angles demonstrated by the NH_3 + Ar collision data in the higher *J* states, particularly $J = 5$. A key difference between the symmetric tops in question is the geometry of the molecules. The methyl radical is planar in nature and although NH_3 can be modelled as planar for symmetry purposes,

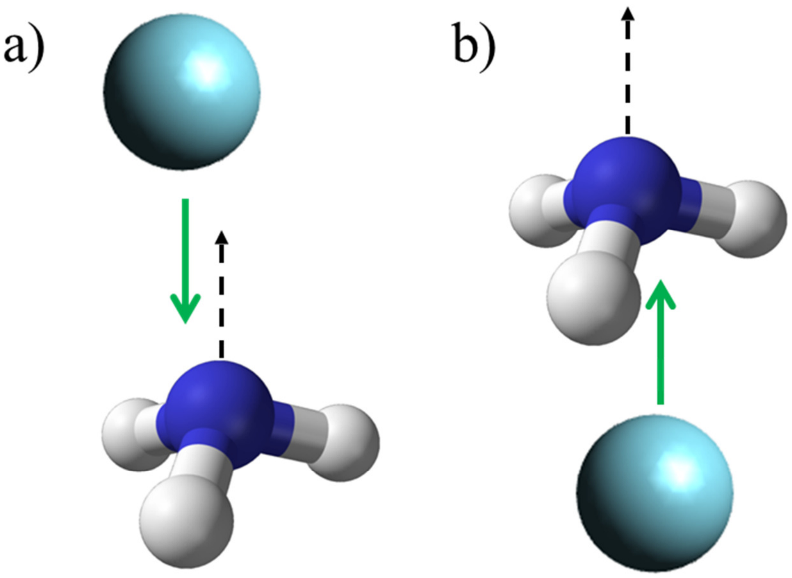

Figure 3.8 a) Ar approaching the lone pair of electrons on the NH_3, $\psi = 0°$ b) Ar approaching from the direction of the hydrogens, $\psi = 180°$.

the fact remains that it is pyramidal and can undergo inversion, which CD_3 cannot. As a result some of the differences in the nature of the scattering will be caused by parity inversion in the NH_3 and so the differences cannot be assumed to be purely resulting from the open shell nature of the methyl.

The geometry affects the nature of the scattering in another way. Theoretical predictions[57] find that the collider will experience a different potential depending on the direction of approach to the nonplanar NH_3 (ND_3). If the direction of approach is directly towards the nitrogen, from $\psi = 0°$, such as that seen in Figure 3.8a), then the collider will experience a more repulsive interaction than if the collider were to approach from the direction of the hydrogens ($\psi \approx 180°$) which is shown in Figure 3.8b). This is due to the interaction of the approaching atom with the lone pair of electrons on the nitrogen. This has certainly been found to be the case for He;[57] however, due to its larger van der Waals radius, Ar appears to demonstrate that of these two interactions the lowest energy conformer is from the direction of the lone pair[98] for the van der Waals complex, NH_3-Ar. All directions of approach are expected to occur with equal probability and as such the differences that arise from NH_3 being non-planar may contribute to the wider range of scattering angles observed for NH_3 in comparison to CD_3.

In the comparison between CD_3 and ND_3 in collisions with He,[57] theory shows that the nature of the rotational excitation, and how it couples with the isotropic potential of the symmetric top, affects the scattering distribution of the molecule according to the nature of the symmetric top. There is currently little theoretical information describing how the anisotropic contributions influence collisions that take place within the region of the intermolecular potential that is dominated by attractive forces as observed in NH_3-Ar collisions. Quantum scattering calculations would allow a more complete contrast between this system and the more repulsive NH_3-He potential. Currently this information is not available to be able to make this comparison.

3.4 Summary

This chapter has reported state-resolved differential cross sections for the inelastic scattering of NH_3 with Ar obtained at 318 ± 37 cm^{-1}. The DCSs from this work demonstrate a forward dominated range of scattering angles as expected based on previous scattering experiments by Meyer and previous theoretical calculations which have demonstrated that the PES of this collision system is dominated by attractive forces. This results from the more diffuse nature of Ar when contrasted to NH_3-He scattering which is dominated by repulsive regions of the PES. The forward scatter is indicative of the large impact parameter collisions that are predicted based on the increased size of Ar and the increased collisional cross section relative to scattering with He.

In addition to this, it has also been observed that as J increases the range of scattering angles also increases, in line with what has been previously observed with other scattering systems. This is caused by the decreasing impact parameters resulting from the gradually more ‘head-on’ collisions required to achieve greater ΔJ, which deflects the NH_3 more from its original trajectory. Within individual J states, there is also a more subtle trend of decreasing amounts of backwards scatter as k increases. Numerous explanations as to the potential cause have been suggested although it could equally be down to contributions from a number of, or all, of the factors discussed in Section 3.3.2.

The scattering of NH_3 has also been contrasted qualitatively with CD_3 which shows a tendency for the closed shell symmetric top to have a wider range of scattering angles than the open shell symmetric top. This can be explained by geometry differences and differences in the interaction potential due to the different reduced mass of the system although this is an assumption taken from work with He and so it is possible that the expected scattering behaviour resulting from an attractive interaction will be different.

This chapter, regarding the simple collider Ar, also provides a baseline to which other collider molecules can be contrasted. Later chapters present collisions involving NH_3 with a range of molecules, including hydrocarbons, which can be compared to argon in terms of collisional cross section and molecular radii; however, their more complex structure means that this will influence aspects of the collisions such as the duration of interaction and therefore nature of the scattering.

Chapter 4 – Ammonia + Deuterium

4.1 Background

4.1.1 $NH_3 + H_2$ background

Hydrogen is the most abundant molecule in the universe,[100, 101] as a result it is one of the most likely sources of collisions that result in the unexpected rotational excitation of NH_3 that is discussed in Chapter 3.1.1. Very little work has been done to study the scattering cross sections of molecular collisions with NH_3, however, due to its size and comparability with He, for which there is an abundance of information, [57, 63-65, 74, 92, 102, 103] H_2 is the perfect starting point for molecule-molecule collisions. A range of experiments have investigated inelastic collisions between molecular hydrogen and triatomics such as HCN[104] and deuterated water analogues[60] so investigating its influence on NH_3 is a natural progression.

Like NH_3, H_2 has 2 nuclear spin states, *ortho* and *para,* which contribute in different ways to the dynamics. As H_2 is a fermion the overall wavefunction must be antisymmetric in nature, resulting in the antisymmetric (*para*) nuclear spin state pairing with the even rotational states ($J_{H_2} = 0, 2…$) whilst the symmetric (*ortho*) nuclear spin state pairs with the odd rotational states ($J_{H_2} = 1, 3…$). In the past, in order to model the dynamics of collisions of a molecular system with H_2, ^4He was considered an analogue of *para*-H_2 ($J_{H_2} = 0$), due to the comparable lack of a dipole-quadrupole interaction in both systems.[101] The simpler nature of He, particularly its lack of rotational degrees of freedom, meant that it was easier for theoreticians to model in conjunction with polyatomics and it was long assumed that this was sufficient to describe the behaviour of the two systems, particularly in high temperature conditions, i.e. ~300 K, such as those used in the experiments described in this chapter. Schleipen et al.[105] established in 1993 that the state-to-state cross sections for the NH_3-He and NH_3-*para*-H_2 systems exhibit more differences than previously thought. The data from this work, however, provides little information as to the characteristics of the scattering processes involved.

The differences between the molecule-molecule system and the molecule-atom system, are supported by more recent works of Willey et al.,[106, 107] which instead investigate the pressure broadening of the NH_3 rotational spectrum in a multi-collision environment, in low temperature (10 to 50 K) regimes such as those found in interstellar clouds. Their work finds that the NH_3 + *para*-H_2 collisions exhibit greater differences than the NH_3 + He system with regards to collision rates and collisional cross sections. The conclusions of this group show that the major contributor to the differences between the nature of NH_3 collisions with He and H_2 is the well depth of the potential energy surfaces (PESs). Recent calculations[96, 108, 109] of the two PESs have found that the attractive well for the NH_3-H_2 PES is around eight times greater in depth than that of the NH_3-He PES. The dominance of the attractive well plays a larger part in low energy collisions compared to the more repulsive nature of the NH_3-He interaction. This places the nature of the NH_3-H_2 collision somewhere between the NH_3-He and NH_3-Ar systems because the attractive well of the NH_3-H_2 is not as deep as that observed in the NH_3-Ar PES. The focus of the experiments described by Willey et al. is on the effect of multiple collisions, however, this removes their studies from the dynamics of single collisions. They also study the effects of low temperature conditions in order to contribute to the detail of the potential energy surface for the NH_3-H_2 collisions. In addition, due to the 3:1 ratio of *ortho*:*para* H_2 at equilibrium, what is often observed is dominated by the collisions involving *ortho*-H_2 so focussing on a purely *para*-H_2 system removes the added complexity that appears in these molecule-molecule collisions.

Experiments conducted in conjunction with velocity map imaging (VMI) techniques by Tkáč et al.[63, 73] provide a comparison between the images and DCSs of He and H_2 scattering with ND_3. Unlike the work of Willey, these are conducted under single collision conditions and therefore provide information that can be directly related to the characteristics of the colliders. These experiments were also conducted at collision energies representative of ambient temperature regimes of ~300 K, similar to the conditions in the experiments in this thesis. The initial state selection in the work by Tkáč et al.[73] adds to the information regarding the use of ND_3-He as a description of ND_3 + *para*-H_2 and finds that even under the higher energy conditions there is a shift towards a more attractive dominated regime for the molecular system with the differences in the integral cross sections (ICSs) being significant, although in contrast to this, the differences between the differential cross sections (DCSs) are more subtle. In general each ND_3 DCS exhibits a similar shape irrespective of the collision partner, but with less scattering into the sideways and backward angles observed for the same ND_3 J_k states resulting from ND_3-H_2 collisions, in comparison to ND_3-He.[63]

As mentioned earlier, contributions to the scattering cross section come from both nuclear spin states of H_2. The work by Tkáč et al. can only distinguish the *ortho*/*para* contributions through the use of quantum scattering calculations to calculate the expected DCSs. These find that $J_{H_2} = 0$ behaves differently to $J_{H_2} = 1$ and 2 because it has zero total angular momentum and therefore no dipole-quadrupole interaction.[73] However, much like the work with ND_3-Ar[66] discussed in Chapter 3, the effect of the nuclear spin state of the ND_3 is not investigated.

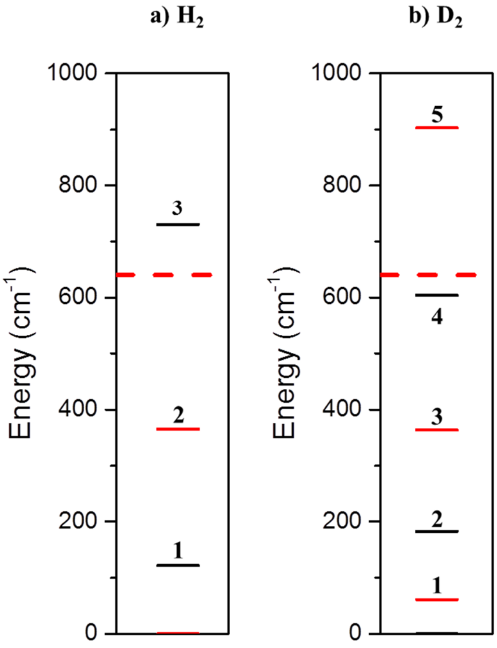

Figure 4.1 Energy level diagrams for a) H_2 and b) D_2. The colour of the lines indicates the nuclear spin state of the energy level – black is *ortho* and red is *para*. The dashed line indicates the experimental collision energy limit of 640 ± 60 cm^{-1}.

4.1.2 $NH_3 + D_2$

Despite the focus on H_2, relatively little comparative work has been conducted with its deuterated isotopologue, D_2. There are enough differences between the two molecules that one would expect both similarities and differences in the nature of the collisions between NH_3 and D_2 when compared with those using H_2. Like H_2, D_2 has two nuclear spin states however as it is a boson, the symmetric (*ortho*) nuclear spin state must pair with the even rotational states ($J_{D_2} = 0, 2\ldots$) in order to produce the overall symmetric wavefunction required, likewise the antisymmetric (*para*) spin state will pair with the odd rotational states ($J_{D_2} = 1, 3\ldots$). For D_2 these exist in a ratio of 2:1 *ortho*:*para* at room temperature. Again, it is not possible to interconvert between these two spin states through collisional excitation, hence the $\Delta J = 0, \pm 2$ rules governing rotational excitation. The rotational constant of D_2 is much smaller than that of H_2, i.e. $B_{D_2} = 30.443$ cm^{-1} vs. $B_{H_2} = 60.853$ cm^{-1}, hence the simultaneous rotational excitation of the D_2 has a higher probability because more states are energetically accessible, see Figure 4.1. The different coproduct rotational states accessible in the collisions could result in differences in the DCSs compared to those obtained for H_2.

This is the first work to detail the dynamics of NH_3 + D_2 collisions and as such provides a comparison to the CD_3 + D_2 experiments that were previously carried out on this apparatus and are described more fully elsewhere.[62] As in the previous chapter the comparison of these two will allow for qualitative conclusions to be made based on the open/closed shell nature of the symmetric top involved in the collisions. Just as with the corresponding ND_3 experiments, key findings from collisions involving the methyl radical with D_2/H_2 show that the scattering appears in more forward angles than observed with CD_3-He.[78] Backwards scatter of the CD_3 is observed in collisions with D_2, however it appears in higher J product states compared to its first appearance in collisions of CD_3 with He. The differences between collisions of CD_3 with D_2, H_2 and He result in a progression in terms of greater backwards scatter in the angular distribution of the CD_3. For example examining CD_3 $J = 5$ products, for these collision pairings, demonstrates this particularly well, for which the maxima of the DCSs are reported as 87°, 127° and 167° respectively.[62]

In contrast to the atomic nature of Ar described in the previous chapter, it is necessary to consider which internal energy levels are accessible within the diatomic D_2. As a molecular system there are now vibrational and rotational internal modes available for the dispersal of energy upon collision. The experiments in this chapter use a pure sample of D_2 with a stagnation pressure of 4 bar, the expansion of which provides sufficient cooling to achieve the lowest two rotational states $J_{D_2} = 0$ and 1, at their natural abundance of 2:1. The nature of the molecular beams and the collision energies involved mean that vibrational excitation of D_2 is unlikely after collision as the energy required to access the first vibrational level is 2992 cm^{-1}. Rotational excitation is possible at this collision energy, but the work with CD_3 does not appear to observe simultaneous excitation of the D_2.[62] However, as each image consists of a set of product k states, the breadth of the rings in the CD_3 images could disguise any evidence of this excitation. Contained within this chapter is a discussion of the D_2 rotational

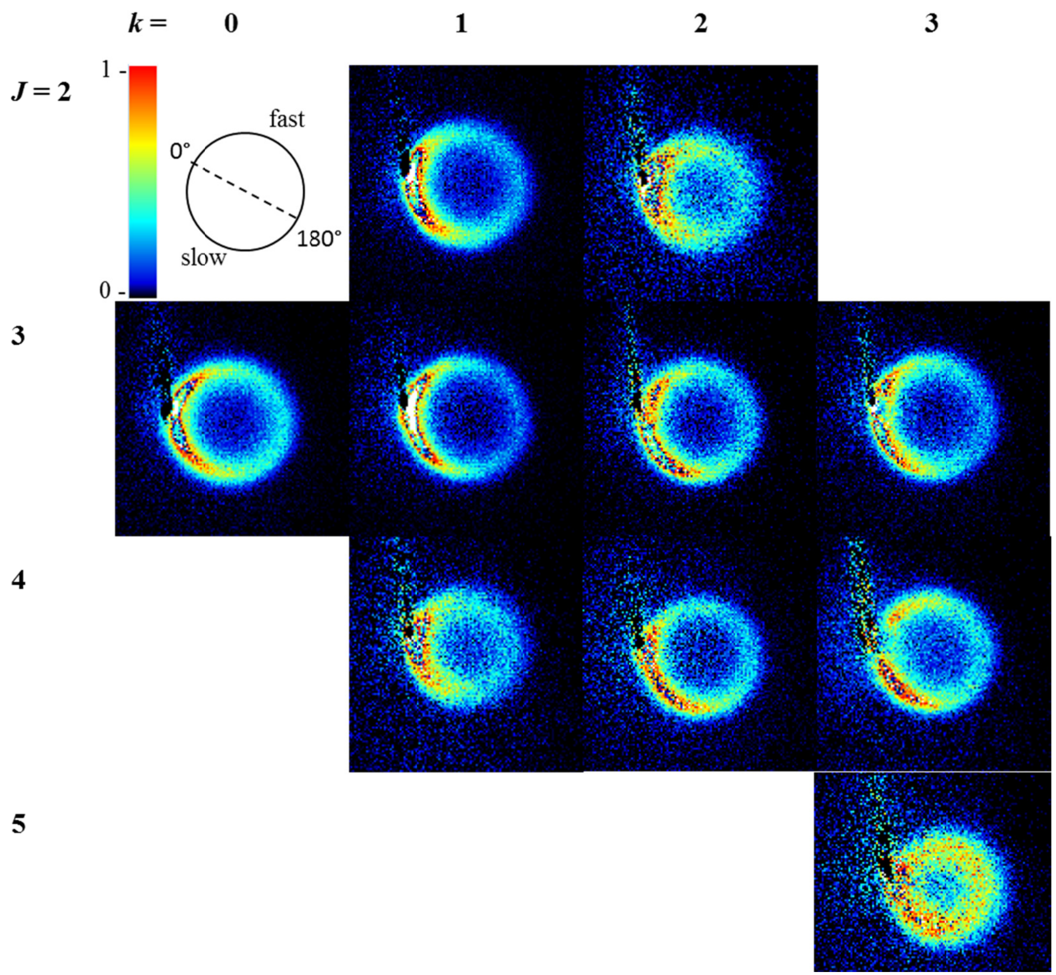

Figure 4.2 Experimental images for the inelastic scattering of NH_3-D_2 at a collision energy of 640 ± 60 cm^{-1}. The images are arranged according to J_k state, with k increasing across the rows and J increasing down the columns, as labelled. The orientation of the images is depicted in the top left corner. The dark spots on the images result from the removal of the beam spot of unscattered NH_3.

excitation that is observed in conjunction with NH_3 rotational excitation and the differences found in the NH_3 DCSs that correspond to the contributing D_2 channels. The experimental collision energy of NH_3 with D_2 (640 ± 60 cm^{-1}) discussed in this chapter is comparable to those used in the previous experiments of ND_3-H_2 [73] discussed above as well as the CD_3 work.[62, 72]

4.2 Results

4.2.1 Velocity Map Images

All of the experiments were conducted at a collision energy of 640 ± 60 cm^{-1}, which means that there is sufficient energy available for partitioning into the internal quantum states of both NH_3 and D_2, see Figure 3.1 and Figure 4.1 for the energies required to access the different states in both molecules. The experimental images shown in Figure 4.2 are for $NH_3 + D_2$ for $J_{NH_3} = 2$ to 5 with $k = 0 - 3$ as applicable. They demonstrate a visible increase in sideways and backwards scatter as J_{NH_3} of the product states imaged increases. The range of scattering angles is visibly greater than those observed in Chapter 3 for NH_3-Ar collisions; this is discussed in more detail in section 4.3.1. Once again the detection bias is visible in the asymmetry of the image intensities about v_{rel}, this is accounted for using a density-to-flux transformation. However, this is achieved using a different methodology to Chapter 3 and the methods used and reasons why this

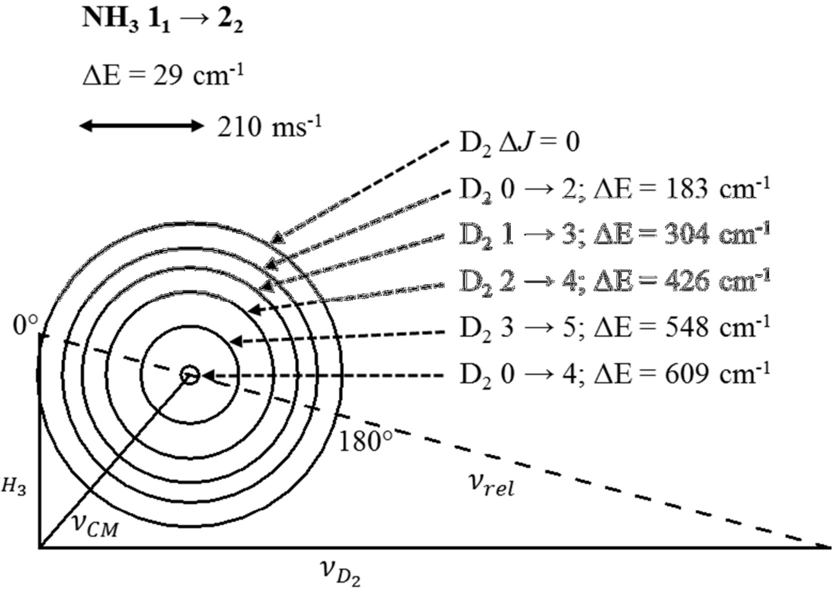

Figure 4.3 Newton diagram for inelastic scattering of NH_3-D_2. The Newton spheres correspond to the D_2 transitions that are energetically accessible, at 640 ± 60 cm^{-1}, when formed in conjunction with NH_3 $J_k = 1_1 \rightarrow 2_2$ excitation. The energy of each of these transitions is noted.

is necessary are discussed in section 4.2.2. What is also evident from extracting the raw angular distributions from the experimental images is that the maximum signal intensity appears at smaller radii than expected for the NH_3 J_k states if they were formed in conjunction with no excitation of the D_2, suggesting that there is simultaneous excitation of the D_2.

Figure 4.3 shows the Newton spheres for the D_2 transitions that are both energetically and symmetry allowed. The observable D_2 excitations at our experimental collision energy are $J_{D_2} = 0 \rightarrow 2$ ($\Delta E = 183$ cm^{-1}) and $J_{D_2} = 1 \rightarrow 3$ ($\Delta E = 304$ cm^{-1}). Although energetically accessible $J_{D_2} = 2 \rightarrow 4$ ($\Delta E = 426$ cm^{-1}) and $J_{D_2} = 3 \rightarrow 5$ ($\Delta E = 548$ cm^{-1}) are not expected to be observed as the D_2 initial states in the molecular beam are restricted to $J_{D_2} = 0$ and $J_{D_2} = 1$. There is no evidence for $J_{D_2} = 0 \rightarrow 4$ ($\Delta E = 609$ cm^{-1}) which is not entirely unexpected, the only NH_3 state that this is an energetically accessible pathway for, is $J_k = 2_2$ ($\Delta E = 29$ cm^{-1}) and the resultant scattering would be mapped onto the central few pixels of the image only. The D_2 can be in an excited initial rotational state such as $J_{D_2} = 1$, where the scattering is formed without collisional excitation of the D_2, i.e $\Delta J_{D_2} = 0$, the rotational angular momentum of the D_2 is conserved. The degree of initial rotational excitation is important to note as the amount of rotation that occurs during the collision may have an effect on the nature of the scattering.

The duration of a collision, $\Delta\tau$, can be calculated from equation 4.1:

$$\Delta\tau = \frac{\alpha}{v_{rel}} \qquad 4.1$$

Where α is the internuclear distance of the colliders at the point of the minimum van der Waals energy. The global minimum for NH_3-H_2 is 3.33 Å,[96] which can been used as an estimate for NH_3-D_2 interaction distance because the change in reduced mass would have only a minimal effect on this value, and v_{rel} is calculated to be 2175 ms^{-1}. This results in an overall collision duration of 153 fs which, for comparison, is less than half that of NH_3-Ar at $\Delta\tau = 478$ fs. From this value, it is possible to calculate the amount of rotation that occurs about the angular momentum vector in both colliders during this timeframe. The rotational period, T, for a diatomic is described by the relationship:[110]

$$T = \frac{2\pi I_B}{\hbar\sqrt{J(J+1)}} \qquad 4.2$$

which in turn can be adapted to describe the rotational period with respect to the primary molecular axis of a symmetric top through the inclusion of k and I_c:[110]

$$T = \frac{2\pi I_B}{\hbar\sqrt{J(J+1)}} + \frac{2\pi I_c}{k\hbar} \qquad 4.3$$

These give rotational time periods for D_2 in $J_{D_2} = 1$ of 387 fs and NH_3 in $J_k = 1_1$ of 3861 fs. The rotational periods of the lowest few states of both molecules are included in Table 4.1. This means that NH_3 can essentially be considered rotationally stationary as it only rotates through 14° during the collision. In contrast D_2 undergoes almost half of a rotation at 142°. The nature of the interaction will therefore vary as the D_2 rotates because the NH_3 will be presented with a changing proportion of the D_2 with which to interact.[108] Therefore the region of the PES on which the collision is occurring, with respect to the internuclear distance and the approach towards the NH_3, will affect the probability of co-excitation of the D_2.

Table 4.1 a) rotational periods of D_2 for $J = 1 – 3$ and number of degrees rotated during the collision of 153 fs b) same as applied to initial J_k states of NH_3, other than 0_0.

a)

J_{D_2}	**D_2 T (fs)**	**Rotation during collision (°)**
1	387	142
2	223	247
3	158	349

b)

J_k	**$NH_3$$T$ (fs)**	**Rotation during collision (°)**
1_0	1184	47
1_1	3861	14
2_2	2022	27

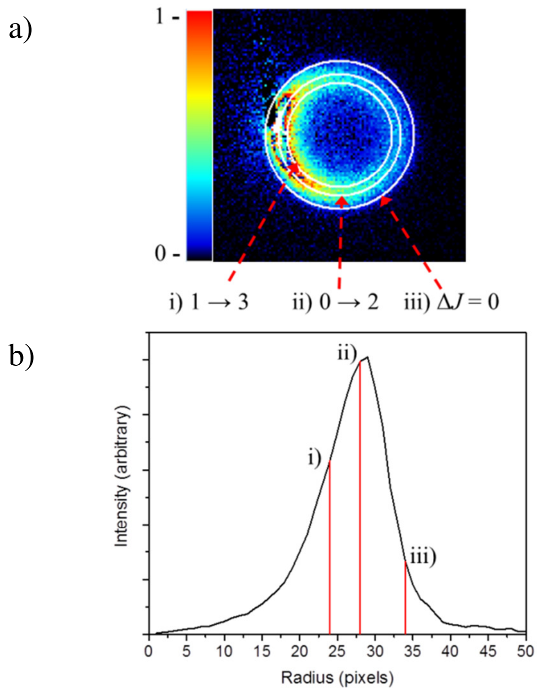

Figure 4.4 a) experimental image NH_3 $J_k = 2_1$, with white ring overlays marking the radii of the D_2 rotational excitation channels b) plot showing signal intensity vs pixel radii for the same experimental image. The red lines indicate the calculated radii of the scattering rings where D_2 excitation i) 1→3 ii) 0→2 iii) $\Delta J = 0$.

An example plot of speed distribution from the NH_3 $J_k = 2_1$ state, extracted from the raw image, is included in Figure 4.4b and includes markers at the calculated radii for this state when formed in conjunction with the different possible D_2 co-products. The plot demonstrates that this state is formed alongside all 3 of the possible D_2 states available, with $J_{D_2} = 0 \rightarrow 2$ as the dominant channel. The Newton spheres for the scattering formed in conjunction with each of these states would, in a perfect scenario, form a set of concentric spheres resulting in the imaging of a distinct ring for each collision channel. However, in actuality the experiment produces numerous Newton spheres for each channel as a result of the range in the molecular beam parameters such as speed and direction, resulting in the superposition of overlapping spheres that are not completely concentric. In addition to this the experiment does not have sufficient resolution for the D_2 excitation to appear as distinct rings. The calibration for the velocity mapping of the ions results in an expected maximum separation of the D_2 $\Delta J = 0$ ring and $J_{D_2} = 0 \rightarrow 2$ excitation ring of only ~8 pixels, this value is even smaller for the separation between the $J_{D_2} = 0 \rightarrow 2$ and $J_{D_2} = 1 \rightarrow 3$ radii at ~5 pixels. Relative to the total width of the scattering simulated for the three instrument functions, which individually are ~12-13 pixels wide over a total summed radius of ~22-25 pixels, it becomes clear that there is a great deal of overlap expected between the scattering into these channels. As a result of this small division between rings, alongside the ‘blurring’ of the experimental images caused by the molecular beam characteristics, the products detected from the different collision channels in the experimental images will be indistinguishable. Figure 4.4a includes the experimental image for $J_k = 2_1$ with circles overlaid at the expected peak pixel radii of the 3 D_2 excitation channels available. This NH_3 state is used as an example in Figure 4.4 as it is one of the few that has clearly discernible contributions from all 3 D_2 coproduct states.

Across the range of NH_3 product states differing propensities for collisional formation of the different D_2 co-products are observed. The $J_k = 2_2$ state is unique in that it appears to have strong contributions from the two excited states of the D_2 and almost nothing from the $\Delta J = 0$ channel. The majority of NH_3 states primarily appear to be formed in conjunction with no co-excitation of D_2 and $J_{\mathrm{D_2}} = 0 \rightarrow 2$ although from the images alone it is difficult to determine the ratios of these states. What is surprising from the images is that there is obviously a drop off in the amount of scatter from collision products formed in tandem with $J_{\mathrm{D_2}} = 1 \rightarrow 3$, despite there being sufficient collision energy for its formation in all of the NH_3 states that have been imaged. For the nature of the scattering within these states it is necessary to look at the DCSs.

4.2.2 Differential Cross Sections – extraction

As the experimental images demonstrate observable contributions from the three D_2 co-excitation channels, the scattering distribution cannot be assigned to a single DCS for each NH_3 product state. This means that the experimental images cannot be processed exclusively using the same methodology applied in Chapter 3 because the weighting of the contributions of the different collisional excitation pathways is unknown. It is instead necessary to forward simulate the DCSs for each NH_3-D_2 combination from the instrument functions of each state pairing. This allows for the assignment of the weighting of the collision channels whilst also taking into account the overlap between the D_2 state contributions.

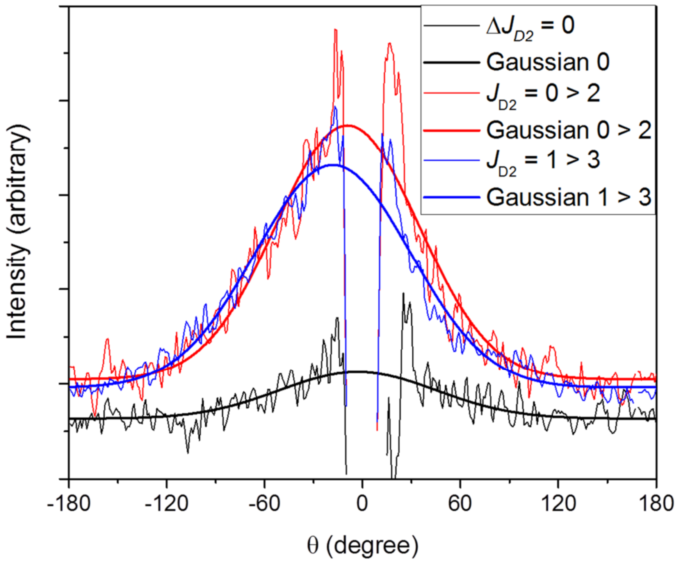

Figure 4.5 Raw angular distributions of the slices associated with the D_2 rotational excitation channels and their associated Gaussian fits. All taken from NH_3 product state image for $J_k = 2_1$.

An instrument function is generated for each collisional pathway using the same Monte Carlo simulation program described in Chapter 2.8.1. Each experimental image is then divided into 3 slices that are positioned in order to approximate the 'exclusive' scattering into each of the collision channels. From the slices, the raw angular distributions are extracted, examples of which are shown in Figure 4.5. These slice angular distributions are then fitted with a function in order to provide initial guess parameters for the DCSs in the subsequent fitting. As can be observed in Figure 4.5, the best description for this data is a single Gaussian curve centred near to 0°.

The fitting of the experimental data is done using a custom LabView program. It converts the instrument functions and the intensity normalised experimental image into triangular polar pixel arrays and then a simplexing subprogram is used to fit the 3 instrument functions, multiplied by each guess DCS, to a set radii range of the experimental data. This is achieved by iteratively adjusting the parameters of the Gaussians that describe the DCSs until a set tolerance threshold is reached. The resulting 3 Gaussians provide the $\theta = -180°$ to 180° DCSs for each collisional pathway. The parameters used for initialisation are x_0, y_0 and σ, with each channel given an initial magnitude of 1. To avoid any of the resulting DCSs being distorted by areas of low intensity from the beam spot subtraction and more importantly nearby pixels of high intensity, a wedge of ±10° is used to remove the beam spot region (see Chapter 2.9 for details).

The extracted $\theta = -180°$ to 180° DCSs are then processed to obtain an average of the multiple experimental datasets resulting in a final DCS describing $\theta = 0\text{-}180°$. However there are some minor alterations to the methodology used in Chapter 3 because of the techniques used to extract the DCSs and the additional co-product channels. The image intensity is normalised prior to fitting, detailed above, in order to allow for comparison between the individual datasets. Despite this the y-scale of the outputted fits are not normalised as the program weights the intensity according to the other fitting channels. In order to make the DCSs comparable within datasets and across product states, they are normalised according to the total area of the Gaussian outputs for the product channels required to fit the data. The resulting DCSs are still in relation to $\theta = -180°$ to 180° so are therefore converted into a DCS for $\theta = 0\text{-}180°$, as detailed in Chapter 3.2.2. The final DCSs for each of the NH_3 states imaged, for each of the D_2 coproduct channels, are presented in Figure 4.7, where the normalised fitting results are weighted by relative experimental intensities to produce an overall mean DCS.

One restriction of producing a fit based on a single Gaussian is that this can result in asymmetrical DCSs with respect to $\theta = 0°$. This has proven to be problematic for higher J_{NH_3} product states where the majority of scattering is into more sideways and backwards angles, such as $J_k = 4_3$ and 5_3. From the images for these two states, see

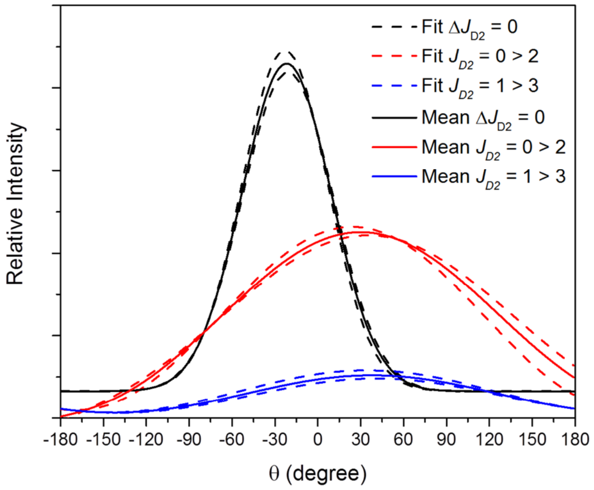

Figure 4.6 Demonstration of good agreement between the fitted DCSs of two experimental datasets for NH_3 product state $J_k = 4_3$ that also exhibit distinct asymmetry across the slow (0-180°) and fast (-180-0°) lab frame hemispheres in each of the D_2 co-excitation channels. Dashed lines are the experimental fits and the solid line is the weighted mean of each channel. Intensity normalized by total area of the 3 channels as described in text.

Figure 4.2, there is obvious scattering in the backwards direction, which should be unaffected by the instrument function and as such should be fitted by the DCSs. However, the resultant DCSs instead peak at a point that is offset considerably from $\theta = 0°$ causing them to be asymmetrical, Figure 4.6. In order to overcome this, altering the program to fit multiple Gaussians in order to maintain the symmetry may be necessary in future.

4.2.3 Differential Cross Sections - data

The general trends that are observed in the experimental images are highlighted by the extracted DCSs. The tendency towards a wider range of scattering angles as $J_{\mathrm{NH_3}}$ increases that has been observed with many other scattering systems is continued here and is discussed later in this section with respect to the D_2 co-product channels. There are no apparent trends across k within single $J_{\mathrm{NH_3}}$ states. However, as discussed more fully below, there are minor trends observed depending upon the nuclear spin state of the NH_3 product. A more detailed description of what is observed in the DCSs within the D_2 subsets is discussed in Section 4.3.1.

Commencing with the channel that results in simultaneous collisional excitation of the D_2 through $J_{\mathrm{D_2}} = 1 \rightarrow 3$, it can be seen from the plot that shows all of these DCSs in Figure 4.8c that the $J_{\mathrm{NH_3}} = 2$ states are the only NH_3 product states with any significant contribution to the scattering signal from this channel. The signal is strongest for $J_k = 2_2$ and is dominated by angles where $\theta \leq 90°$. In $J_k = 2_1$ this channel demonstrates a subtly broader angular distribution than $J_k = 2_2$ and it contributes much less to the overall scattering picture in terms of magnitude. In higher energy NH_3 states, there is some scatter within the inner radii of the scattering rings that have been fitted by the $J_{\mathrm{D_2}} = 1 \rightarrow 3$ channel. This results in a more isotropic DCS with very low intensity relative to other channels particularly for $J_{\mathrm{NH_3}} \geq 4$.

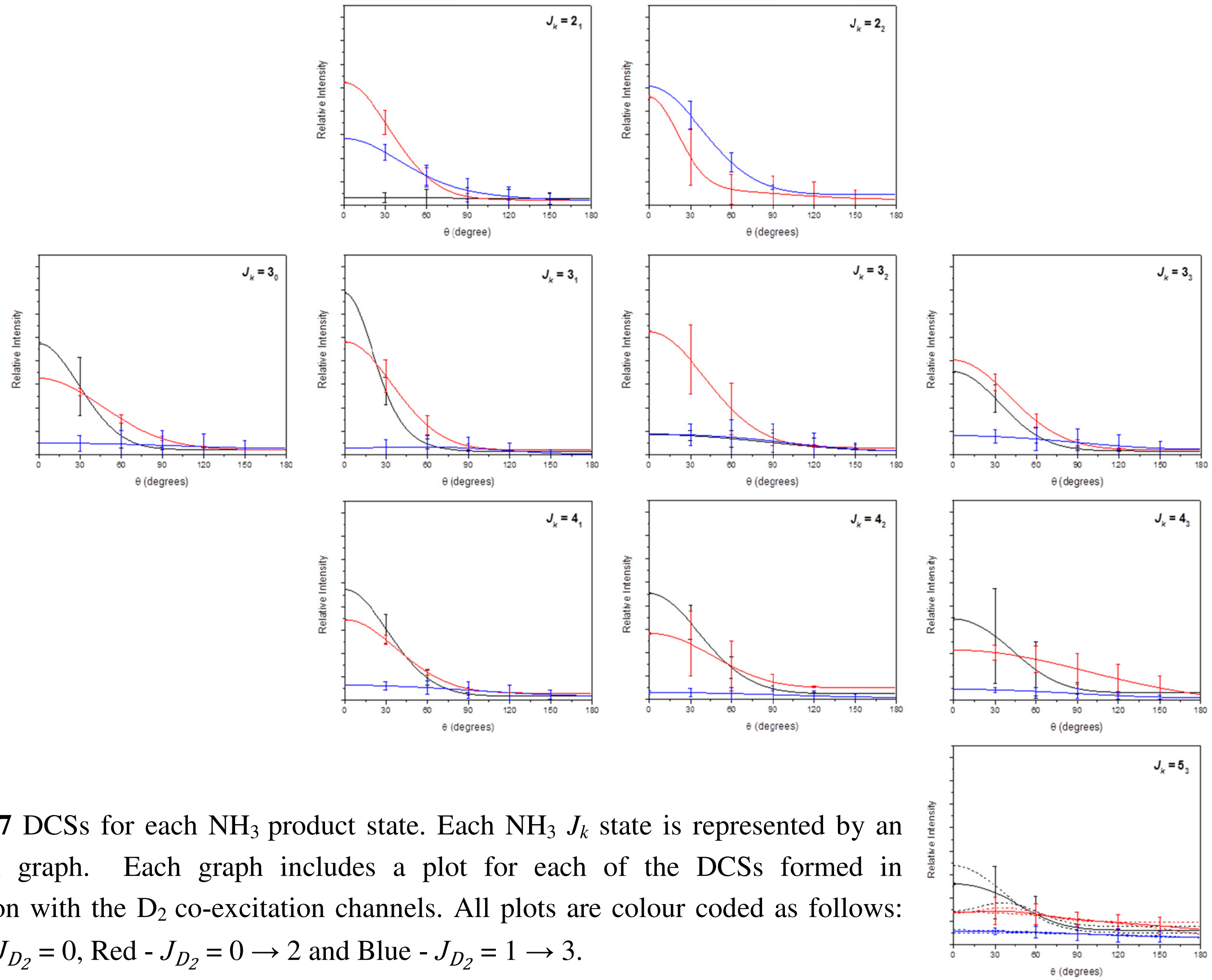

Figure 4.7 DCSs for each NH_3 product state. Each NH_3 J_k state is represented by an individual graph. Each graph includes a plot for each of the DCSs formed in conjunction with the D_2 co-excitation channels. All plots are colour coded as follows: Black - $\Delta J_{D_2} = 0$, Red - $J_{D_2} = 0 \rightarrow 2$ and Blue - $J_{D_2} = 1 \rightarrow 3$.

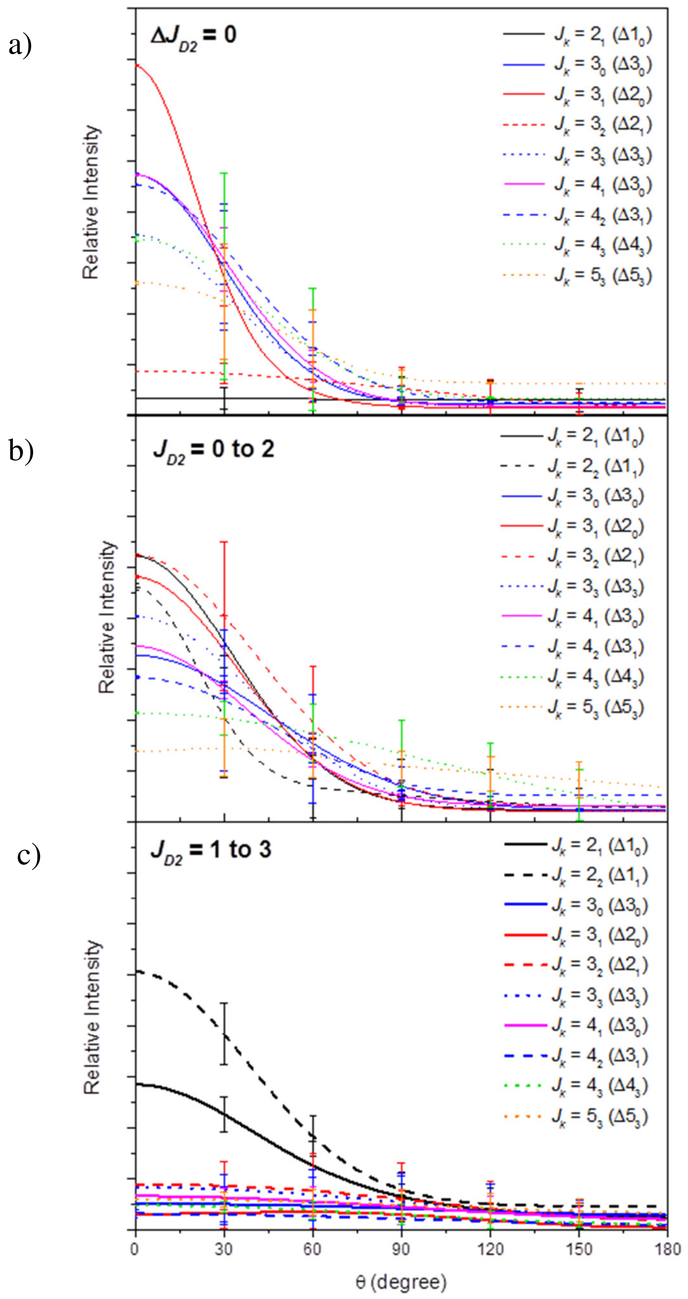

Figure 4.8 DCSs for each D_2 co-product channel. Each plot includes the DCSs for each NH_3 product state when formed alongside a) $\Delta J_{D_2} = 0$, b) $J_{D_2} = 0 \rightarrow 2$ and c) $J_{D_2} = 1 \rightarrow 3$. The nature of the transition is noted in brackets, the plots are colour coded according to ΔJ and line style according to Δk with the exception of $J_k = 4_1$ for clarity.

When the instrument function for $J_{\mathrm{D_2}} = 1\rightarrow3$ is not included in the forward simulation the fit either fails completely, or produces a much poorer fit, as defined by analysis of the fit residuals, than when it is included. It may be the case, that for these higher $J_{\mathrm{NH_3}}$ states, what signal there is for the $J_{\mathrm{D_2}} = 1\rightarrow3$ channel is overwhelmed by the overlapping $J_{D_2} = 0\rightarrow2$ transition as the expected radii of the scattering is only separated by only 4 or 5 pixels as discussed previously in section 4.2.1. This would then result in this data being fitted by the DCS of the $J_{\mathrm{D_2}} = 0\rightarrow2$ transition which could in turn mask some of the more subtle behaviour that may otherwise be observed in the more dominant transitions. This will also apply to the region of coincidence between the scattering of $\Delta J_{\mathrm{D_2}} = 0$ and the $J_{\mathrm{D_2}} = 0\rightarrow2$ excitation channel, although to a lesser degree as the separation is slightly larger at ~8 pixels.

The nature of the NH_3 scattering that is formed alongside the *ortho* excitation channel of D_2, $J_{\mathrm{D_2}} = 0\rightarrow2$, is more complex than that produced with the *para* excited D_2. As shown in Figure 4.7 and Figure 4.8b, this channel has some scattering in all imaged NH_3 states. The magnitude of the DCSs for this channel show an increase as k decreases in $J_{\mathrm{NH_3}} = 2$ with the scattering dominated by forward scattering into $\theta \leq 45°$ for $J_k = 2_2$ and $\theta \leq 60°$ $J_k = 2_1$. Within $J_{\mathrm{NH_3}} \geq 3$, there is less of an obvious pattern although in general the majority of scattering is into the same range of angles as $J_{\mathrm{NH_3}} = 2$ although the DCSs demonstrate broader profiles. The DCSs of $J_k = 4_3$ and 5_3 are much broader than the other states to the point of almost being isotropic. If the change in the NH_3 DCS is compared within a single k state, it is observed that as $J_{\mathrm{NH_3}}$ increases, the range of angles into which scattering occurs also increases. This is can be seen separately for $J_{\mathrm{NH_3}} = 2$ to 4 in $k = 1$ and 2 for which it is a very subtle shift, and for $J_{\mathrm{NH_3}} = 3$ to 5 in $k = 3$, a plot of which is shown in Figure 4.9, for which the progression to a more isotropic DCS is more pronounced.

For scattering of NH_3 that is formed with no co-excitation of the D_2, ie. $\Delta J_{\mathrm{D_2}} = 0$, a more conservative range of scattering behaviours are observed. The experimental set up does not distinguish which initial state of the D_2 the contributions to these DCSs are coming from although it is expected it to be dominated by the rotational ground state as this exists in a 2:1 ratio to the $J_{\mathrm{D_2}} = 1$ state. For the lowest lying $J_{\mathrm{NH_3}}$ state imaged, $\Delta J_{\mathrm{D_2}} = 0$ contributions to the total scattering are minimal. In $J_k = 2_2$ it was found that excluding this channel provided the best fit to the experimental data. For $J_k = 2_1$ the fit

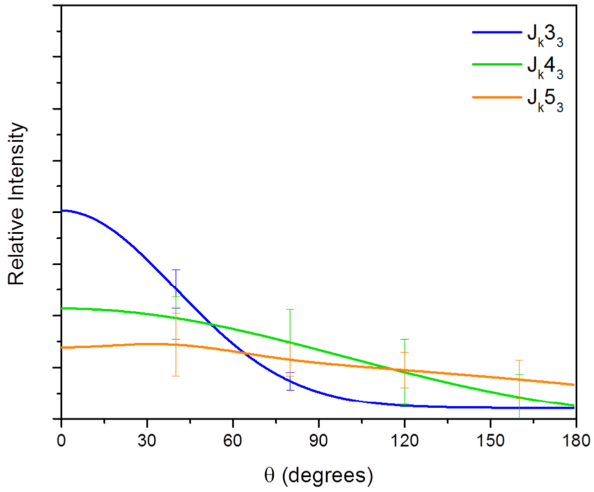

Figure 4.9 Single plot for the DCSs of k = 3 NH_3 product states formed in conjunction with the co-excitation channel $J_{D2} = 0 \rightarrow 2$. Colours as per Figure 4.8.

is almost completely isotropic and is reminiscent of what was discussed for the higher J_{NH_3} states formed in conjunction with $J_{D_2} = 1 \rightarrow 3$. In $J_{NH_3} = 3$ the DCSs are, for the most part, very similar in shape and intensity to the contributions from the $J_{D_2} = 0 \rightarrow 2$ channel. For $J_{NH_3} \geq 3$, there is a general trend of decreasing intensity and increasing angular range in the $\Delta J_{D_2} = 0$ channel as J_{NH_3} increases from 3 to 5, while simultaneously becoming the dominant scattering channel. Once again $k = 3$ exhibits this broadening effect most obviously in contrast to the more subtle changes observed in the NH_3 *para* states in $k = 1$. The $k = 2$ states exhibit very little scattering in this channel until $J_k = 4_2$ the reason for which is examined in section 4.3.1.

Below is a full discussion of these observed trends and a comparison to different collision systems. The analysis of the dynamics of the collisions are treated in classical terms as no quantum scattering information is currently available for this particular system although some assumptions can be made from information about the collisional behaviour of $NH_3(ND_3) + H_2$.

4.3 Discussion

4.3.1 Data trends and comparison to NH_3 + noble gases

The previous section has highlighted the various trends that are observed in the DCSs for different collision co-product excitation channels. In addition there are two NH_3

product states that demonstrate unique behaviour. The $J_k = 3_2$ state is formed almost exclusively alongside the *ortho* excitation channel of D_2 and is the only state to demonstrate this propensity for a single state. Meanwhile the $J_k = 2_2$ is the only state which presents scattering contributions from only two of the co-products channels. In addition, the $J_{D_2} = 1 \rightarrow 3$ and the $J_{D_2} = 0 \rightarrow 2$ channels are similar in magnitude. This is significant for the transition originating in the $J_{D_2} = 1$ state, as this has the lower population in the molecular beam due to the natural abundance of *ortho/para* D_2 states occurring in a 2:1 ratio. As a result, the *para* contribution to this DCS is exceeding that which is expected if this *para* transition was contributing as equally to the scattering as the *ortho* transition, suggesting this is in fact the dominant channel for formation of the $J_{k\,=}\,2_2$ state of NH_3 which, again, is unique to this state. As noted in section 4.2.1, energetically the $J_{D_2} = 1 \rightarrow 3$ excitation is accessible in conjunction with all of the NH_3 states imaged but it is clearly formed preferentially with this particular NH_3 state. It is also found that all collisions that result in the formation of the $J_{k\,=}\,2_2$ NH_3 product state, also cause complete co-excitation of the D_2 through either $J_{D_2} = 0 \rightarrow 2$ or $J_{D_2} = 1 \rightarrow 3$, i.e. there is no co-product scattering with $\Delta J = 0$.

In the lower energy J_{NH_3} states, such as $J_k = 2_2$, 2_1 and 3_2, the collisions are expected to be controlled by larger impact parameters, *b*, than for those NH_3 product states with a larger proportion of internal energy. As the DCSs are dominated by forward angles for the D_2 co-excitation channels, particularly for the excitation through $J_{D_2} = 1 \rightarrow 3$, these larger impact parameters are required to excite the D_2 through the $J_{D_2} = 1 \rightarrow 3$. This appears to be counterintuitive from the perspective of the D_2 as larger impact parameters result in more ‘glancing’ collisions, and are not expected to generate enough torque to cause a greater rotational excitation. Considering the topography of the PES of NH_3-H_2[102] which in terms of shape should be the same as that for NH_3-D_2, the relative gradient of the regions of interaction is controlled by so many factors, such as distance, orientation of the molecules and the angles of approach, that there are many regions away from the optimised geometries that can be described as shallow wells. Based on the data presented here, if the D_2 interacts with the attractive region of the PES, then the probability of additional rotational excitation is increased. A classical consideration of this interaction suggests that D_2 rotational excitation is inhibited by the steep gradient of the potential closer to the NH_3. Hence, the interaction with already rotating molecules, i.e. $J_{D_2} = 1$, only results in NH_3 rotational excitation at small impact parameters. In contrast interactions with larger cross sections that cause small changes in $J_{\mathrm{NH_3}}$, e.g. $J_{\mathrm{NH_3}} = 1 \rightarrow 2$, occur on the region of the PES with a gentler attractive gradient that is sufficient to allow excitation of both molecules. This co-excitation occurs at internuclear distances that result in very little deflection of either molecule resulting in the forwards scattered collision products that are observed.

The behaviour discussed above could in turn influence the trend observed across *para*-NH_3 product states where $J_{\mathrm{NH_3}} = 2$ and 3, $k = 1$ and 2. In order of increasing internal energy, i.e. $J_k = 2_2, 2_1, 3_2$ and 3_1, the progressions observed are:

a) Increasing contribution of the D_2 channel with no co-excitation
b) Increasing intensity and then drop off in contribution by $J_{\mathrm{D_2}} = 0 \rightarrow 2$
c) Decreasing intensity in the contribution from $J_{\mathrm{D_2}} = 1 \rightarrow 3$

More specifically a) exhibits no signal in this channel for $J_k = 2_2$, minimal contributions to the degree that the DCSs are almost isotropic for $J_k = 2_1$ and 3_2 and finally a very sharply forward peaking DCS for $J_k = 3_1$ with the maximum intensity. This intensity drops off in higher lying NH_3 products as scattering shifts into a wider range of angles. Pattern b) shows a gradual increase in intensity from $J_k = 2_2$ to 3_2 with a decrease in the contribution of the $J_{\mathrm{D_2}} = 0 \rightarrow 2$ into the $J_k = 3_1$ which coincides with the sharp increase in $\Delta J_{\mathrm{D_2}} = 0$ mentioned in a). The trend in c) demonstrates a sharp decrease in intensity of $J_{\mathrm{D_2}} = 1 \rightarrow 3$ channel which occurs in parallel to the increase in the channel that conserves the initial state of the D_2, $\Delta J = 0$. This coincidence occurs specifically in the $J_k = 2_1$ and 3_2 states and may be supposed to originate from collisions involving $J_{\mathrm{D_2}} = 1$ as this initial state undergoes decreasing excitation. The more subtle shifts in the characteristics of the $\Delta J_{\mathrm{D_2}} = 0$ DCSs in higher lying rotational states can then be attributed to changes to the ratio of D_2 molecules initially in the *ortho* state being excited. These 3 key observations are clearly intertwined and cannot be explained simply by energetics, as they appear to occur according to the nature of the NH_3 collisional transition, as shown in Table 3.2. This corresponds to $\Delta J_k = 1_1, 1_0, 2_1$ and 2_0 for the four states specifically discussed above. The effect of the collisional transition on the DCS then appears to be overwhelmed by other influences on the system such as the change in $J_{\mathrm{NH_3}}$.

As discussed in Chapter 3.3.2 with respect to the NH_3-Ar collisions, there are clear resemblances in the DCSs of $J_k = 3_0$ and 4_1. These similarities appear across all three D_2 excitation channels in the NH_3-D_2 datasets, suggesting once again that the collisional transition, which in this case is $\Delta J_k = 3_0$ for both states, plays a part in the scattering. However, once again this is the only pair of states with the same collisional transition for which data has been obtained, so corroborating evidence from a different ΔJ_k transition is still required. Nevertheless it does agree with the observations made regarding the effects of the collisional transition discussed for the *para*-NH_3 states.

The experimental images shown in Figure 4.2 exhibit a larger range of scattering angles in D_2 compared to the NH_3-Ar collisions discussed in Chapter 3 and less backwards scattering than for the same NH_3 product states resulting from collisions with He. Rather than a shift to a backwards dominated angular distribution, as seen for NH_3-He collisions as $J_{\mathrm{NH_3}}$ increases, there appears to be a shift towards a more isotropic DCS in the collisions of NH_3-D_2. It has not been possible to confirm if this behaviour continues beyond $J_{\mathrm{NH_3}} = 5$ due to the lack of isolated spectroscopic lines. Unfortunately the fitting of the DCSs fail in larger scattering angles so making more complete comparisons between the NH_3-noble gas systems and this data difficult.

4.3.2 Comparison to $ND_3 + H_2$

The rotational constant for molecular hydrogen is so large that simultaneous excitation of the diatomic is not observed. However, it is still possible to qualitatively contrast the ND_3-H_2 system with the scattering that is formed in conjunction with conservation of the initial state of D_2. The work by Tkáč et al.[73] has a good basis for comparison with data from these experiments, as the quantum scattering calculations for the work are based on the PES for NH_3-H_2.[96] Like the work discussed here, they expect the change in bond length from NH to ND to have a minimal effect. For these experiments, the change to a deuterated system is from H_2 to D_2 for which the bond lengths are calculated to be 0.741 Å and 0.742 Å, respectively[83] which will also have almost no effect on the two PES. Likewise only minor adjustments are required to account for the shift in the centre of mass coordinates. As such the basis is there for QM scattering calculations to be carried out for the NH_3-D_2 system.

As mentioned in Section 4.1.1, one conclusion that is noted in the ND_3-H_2 work is that some of the ND_3 product states present different theoretical DCSs depending on whether the H_2 is initially in the ground state, $J_{\mathrm{H_2}} = 0$, or rotationally excited, $J_{\mathrm{H_2}} = 1$ and 2. However, these DCSs are calculated on the assumption that $\Delta J_{\mathrm{H_2}} = 0$ is the only collision pathway available with only a difference in the degree of rotational excitation of the initial states. The added dimension of excitation of both colliders would be expected to at least subtly alter the DCSs of the co-excitation channels with respect to those of $\Delta J = 0$ due to the alteration in the partitioning of the energy. The resulting alteration to the scattering of the diatomic collider may deflect the scattered NH_3 products into a different angular distribution. The experimental data herein does appear to demonstrate that the DCSs from the $J_{D_2} = 0 \rightarrow 2$ channel are broader in nature with scattering extending into sideways ($\theta = 90°$) and backwards angles ($\theta = 180°$) for higher J_k products. In contrast the NH_3, DCSs formed in conjunction with no collisional excitation of the D_2 are dominated by scattering concentrated into more forwards angles, $\theta \leq 60°$.

Comparing the DCSs for the two systems in more than a qualitative sense is not possible because the only experimental DCSs available for the ND_3-H_2 system are obtained through the use of hexapole state selection hence there is only data for particular ND_3 spin isomers. However, the theoretical ND_3-H_2 DCSs are found to provide a very good fit to the experimental data where comparison is viable. The primary observation from these DCSs is that they are dominated by scattering into forwards angles, $\theta \leq 45°$, which agrees with the scattering observed in the NH_3 DCSs obtained with $\Delta J_{D_2} = 0$. The angular range of the data is somewhat wider, $\theta \leq 60°$; however, this is due to the NH_3 being slightly lighter in mass than ND_3.

4.3.3 Comparison to $CD_3 + D_2$

As in Chapter 3.3.3 comparing the NH_3 results with CD_3 is desirable as it allows comparison of the collision dynamics of symmetric tops that are closed-shell and open-shell in structure. This is difficult as the methyl radical experimental scattering results do not have *k* state resolution as previously discussed in Chapter 3.3.3. As a result it is not possible to be certain about what aspects of the DCSs are due to which *k* states. Furthermore, it becomes impossible to distinguish whether the spread in the imaged rings is resulting solely from the lack of *k* state resolution in combination with the spread caused by molecular beam characteristics or if the width of the rings has contributions from other sources, such as the D_2 co-excitation.

The computational work that was completed for comparison to the experimental data in the CD_3 work[62] found that the inclusion of $J_{D_2} = 0 \rightarrow 2$ altered the calculated DCSs by $\leq$ 10%. This does suggest that there is a minor contribution from this excitation channel from the perspective of the calculations, but as it is so small it is probable that it is being masked by other contributions in the experimental images and therefore the DCSs.

Tkáč et al. do briefly make comparisons between the theoretical DCSs for $J_{D_2} = 0 \rightarrow 2$ for CD_3-D_2 and CD_3-H_2 although unfortunately the DCSs themselves are not included in that paper. The comparisons are made between the D_2 and H_2 systems rather than drawing comparisons within the same system between the differing collision pathways. The differences that are observed are attributed by the authors to the energetics of the 0 → 2 transition for D_2 and H_2 and to mass variations because the PESs for both systems are essentially the same. As the theoretical DCSs are not included, one cannot make direct comparisons between these and the experimental data obtained for NH_3-D_2.

Looking at the range of angles in the CD_3-D_2 experimental DCSs compared to that observed in those obtained for NH_3-D_2, the scattering which occurs alongside D_2 excitation through $J_{D_2} = 0 \rightarrow 2$ is most similar to that observed for the methyl work. The greater dominance of forward scattering observed in the $\Delta J_{D_2} = 0$ channel is very different from what is presented for the CD_3-D_2 scattering. This suggests that this difference in propensities is down to the difference in the nature of the symmetric top. Based on the NH_3-D_2 data, there is a suggestion that the closed-shell nature of NH_3 results in a greater inclination for co-excitation of the D_2. Quantum scattering calculations are required to confirm this through the computation of the DCSs and the ICSs; and the corresponding CD_3-D_2 work suggests that studying the excitation channels of the D_2 collider should be computationally tractable.

4.4 Summary

This chapter has presented the first VMI images and experimental DCSs for the inelastic scattering of NH_3 with D_2. In doing so a novel method for extracting individual DCSs from systems that exhibit simultaneous excitation of the both colliders has been developed. However more work needs to be done to improve the methods used for forward simulation of the NH_3 DCSs, particularly for the regions that are not affected by the detection bias such as those angles where $\theta \geq 120°$ which the fits have a tendency to underestimate. As in Chapter 3, it has been demonstrated that the nature of the collisional transition affects the DCSs and the relative weightings of the different coproduct channels. More specific trends have been observed in the lowest lying *para* NH_3 product states. Increasing sideways and backwards scatter as J_{NH_3} increases is observed, closer to that previously seen in NH_3-He scattering than NH_3-Ar.

The scattering has also been contrasted qualitatively with ND_3-H_2 and CD_3-D_2,where there are considerable similarities exhibited by this work and the ND_3 work, with small variances attributable to mass differences. The scattering with molecular hydrogen is the first step in NH_3-molecule collisions. The next chapter will be continuing this theme by discussing the collisions of NH_3 with small hydrocarbons.

Chapter 5 - Ammonia + Primary hydrocarbons

5.1 Background

5.1.1 Hydrocarbons

Small hydrocarbons are common in the atmosphere and in other planetary atmospheres and therefore play key roles in their chemistry. The bulk of the literature that has investigated the scattering of collisions involving polyatomic molecules, particularly hydrocarbons and other small organic molecules, has focussed on bimolecular reactions for which there are numerous review articles which document the progress in experimental and theoretical techniques.[35, 111-114]

The reason for the focus on reactive collisions is due to the fact that, not only does hydrogen abstraction play an important part in atmospheric chemistry, it is also one of the 'simplest' reactions a hydrocarbon can undergo. The ongoing experimental and theoretical investigations into these reactions have shown that they are far from being as simple as they initially appear and can occur via a range of collisional trajectories according to the nature of the colliders.[45, 46, 115]

Chapter 1.4.1 gives examples of the work conducted by the Suits' group in this field particularly with Cl radicals. The work described in these papers[45, 46] uses crossed molecular beams (CMB) and velocity map imaging (VMI) to obtain the DCSs of the reaction products specifically the hydrocarbon molecules. Focussing on reactive scattering experiments that have used the hydrocarbons discussed in this chapter, methane (CH_4), ethane (C_2H_6) and neopentane ($C(CH_3)_4$), where the species probed is typically the neutral product i.e. HCl. There are many more examples studying the reactions of methane[116-118] and ethane[49, 50, 119-123] than neopentane.[124] These experiments use a range of experimental techniques including VMI[49, 117] and PHOTOLOC[124] imaging methods alongside quantum scattering calculations and trajectory studies.[121] The literature in this field dwarfs that investigating the inelastic collisions of hydrocarbons.

5.1.2 Inelastic scattering

Investigating inelastic scattering of hydrocarbons is key to understanding energy transfer processes in the atmosphere particularly interactions of aerosols.[125, 126] Aerosols often contain hydrocarbon molecules and so often present a hydrocarbon surface available for reactive and inelastic interactions. Due to the size of aerosols, bulk liquid phase dynamics do not always describe the dynamics of these systems adequately. The existing inelastic collision work has focussed on small alkanes such as CH_4[55, 56, 127] and C_2H_6 [8] with atomic colliders. The CH_4 experiments by Nesbitt and coworkers [55, 127] focus on collisions with rare gas atoms, He, Ar and Ne using infrared detection techniques to measure the total inelastic cross section of the CH_4 scattering. In contrast the Minton group use a rotatable quadrupole mass spectrometer to simultaneously measure the inelastic scattering and the range of reaction products for the collisions of high energy O (^{3}P) with C_2H_6.[8] The authors obtain information about the numerous reactive pathways as well as supplying information concerning the dynamics of the inelastic collisions. Information from time-of-flight distributions obtained at a number of collision angles can be extrapolated to provide angular distributions, which, in turn, provides details about the duration of the collisions and the energy exchange that occurs. For this example system, this results in significant forward scatter of the detected O and minimal variation in the post-collisional energy. This technique has been used to great effect to investigate the collisions of hyperthermal O (^{3}P) with saturated and unsaturated long chain hydrocarbon liquid surfaces as discussed in more detail in the section below.

The only VMI experiments that have so far investigated the inelastic scattering of a hydrocarbon were those conducted on the apparatus used herein focussing on the scattering of methyl radicals and the deuterated analogue.[57, 62, 77] As described in previous chapters the authors have investigated the scattering of the methyl radicals with a range of rare gas systems and small diatomics, H_2, D_2 and N_2. These simple molecular collisions have well defined spectroscopies and fewer experimental complexities than are introduced by colliding two polyatomic molecules.

5.1.3 Liquid mimics

Inelastic collisions using hydrocarbons have been studied primarily at the gas-liquid interface. Experimental techniques using liquid surfaces are typically restricted to samples with low or no vapour pressure to minimise evaporation and the creation of background signal from collisions with the vapour, as well as operating problems for vacuum pumps. This means that the molecules studied are long-chain alkanes or alkenes, such as squalane[10, 38, 128-130] and squalene [37, 128] Of particular interest to this work is the paper by Saecker et al.[131] who describe the collisions of small molecular gases including NH_3, D_2O and CH_4 with squalene and glycerol surfaces. They analysed the time-of-flight spectra, obtained with a fixed mass spectrometer, of scattered products from the collisions of a gas sample with a liquid surface on a wheel. The angle of incidence of the molecular beam can be adjusted to alter the collision energies and the probability of a given scattering translational energy product detected. The authors find that there are two modes of inelastic scattering – direct or impulsive scattering, i.e. the molecule recoils immediately from the surface, and trapping desorption where the molecule is "trapped" and undergoes multiple collisions prior to being ejected. These scattering mechanisms result in products with different scattering velocities and internal energies. The preference for each mechanism is dependent on the collider molecule, the liquid surface and the angle of incidence. In relation to the work described herein the direct processes are more akin to the interactions occurring in the collisions being investigated. As the direction of approach changes, the impact parameter is altered resulting in a change in the number of products being scattered towards the detector. Saecker et al. find that overall even "large" gas phase molecules such as NH_3 and CH_4 can almost be modelled as hard spheres with respect to the "soft" liquid surface, particularly for the impulsive scattering mechanism. Whether or not this carries over to gas phase scattering with bulky molecules such as neopentane is not known, or if a longer interaction is indicated by the DCSs will this aid in understanding if and where the differences between gas-phase and liquid surface may lie.

The Minton group have used their rotatable mass spectrometry apparatus, as previously described, to investigate $O(^3P)$ and Cl radical collisions with liquid surfaces.[8] They also use a wheel setup similar to that described previously by the Nathanson group[126, 127] to generate a liquid surface. A key finding from this work is that the effective surface mass of squalane has been calculated to be 76 amu. One of the hydrocarbons used in this work is neopentane which has a mass of 72 amu. This suggests that the neopentane may display scattering dynamics similar enough to the liquid surface that it could behave as a mimic. If this is found to be the case then it would allow gas-phase techniques to be used to investigate liquid surface dynamics and to differentiate behaviours that are due to the surface interaction or due to the phase, i.e. bulk interactions.

As mentioned in Section 5.1.1, the three hydrocarbons for which collisions with NH_3 are investigated within this chapter are CH_4, C_2H_6 and $C(CH_3)_4$. This selection of hydrocarbons is chosen for a number of reasons; firstly, they provide an increasing mass progression from the smallest hydrocarbon possible. The other key reason is the nature of their structures, as shown in Figure 5.1; all of the hydrogens in these molecules are primary, i.e. bonded to primary or terminal carbons. If the nature of the hydrocarbon influences the inelastic scattering, as it does with reactive scattering and scattering from liquid surfaces, restriction to one type of hydrogen environment allows straightforward comparison of these first results.

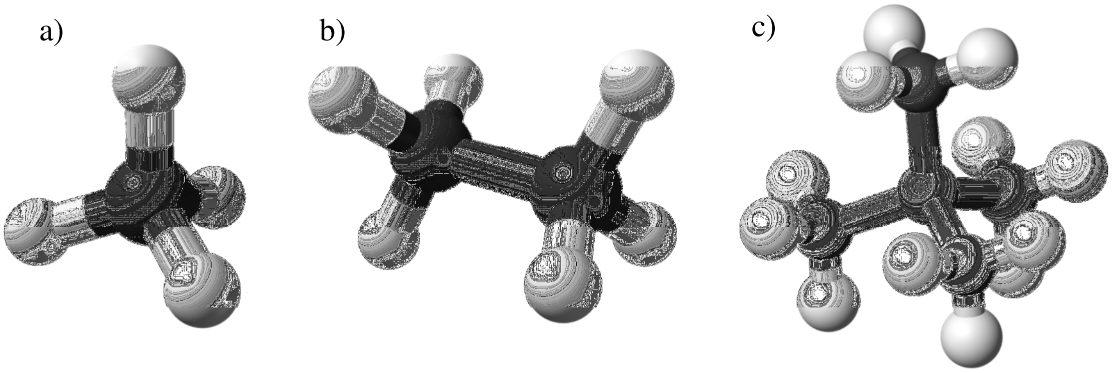

Figure 5.1 Molecular structures of the hydrocarbons colliders used as for collisions with NH_3 in this chapter: a) Methane (CH_4), b) Ethane (C_2H_6) and c) Neopentane (2,2-dimethylpropane, $C(CH_3)_4$.

5.2 Results

5.2.1 Velocity Map Imaging of Hydrocarbon Scattering

Imaging the inelastic scattering of two molecular systems presents additional challenges, as described in Chapter 4, compared to a molecule-atom collision system. The scattering of a polyatomic with a diatomic is the simplest molecule-molecule collision presented in this thesis. However, as discussed with respect to the NH_3-D_2 system in the previous chapter there was a great deal of difficulty in understanding the differences between collisions that result in different degrees of rotational excitation of the collider molecule. For polyatomic-polyatomic collisions the story becomes increasingly complex because the rovibrational energy levels for larger molecules are much closer together and there are more of them.

For the scattering of NH_3 with CH_4 the radii of the scattering rings imaged are smaller than expected for no coproduct excitation, given the collision parameters. This suggests that like the NH_3-D_2 case, the imaged NH_3 product states are being formed in conjunction with simultaneous rotational excitation of the CH_4 collider. However, unlike D_2, the different collisional excitations of CH_4 are separated by tens of wavenumbers instead of hundreds (see Figure 5.2).[55] As with all H containing molecules, the possible collisional excitations of CH_4 are determined according to the resulting nuclear spin states as these cannot interconvert. There are three possible symmetries, *A*, *E* and *F* which exist in a natural ratio of 5:2:9 respectively.[55] The lowest permissible state for each symmetry modification is $J_{CH_4} = 0$ (*A*), $J_{CH_4} = 1$ (*F*) and $J_{CH_4} = 2$ (*E*), however, the population of the molecular beam is likely to occupy up to $J_{CH_4} = 4$. There is added complexity to the available symmetry states, and therefore possible collisional excitation processes, because degenerate levels for $J_{CH_4} \geq 2$ can have different symmetries, as can be observed in the energy level diagram for CH_4 in Figure 5.2. The final CH_4 states that are expected to contribute based on the radii of the images are $J_{CH_4} \geq 6$, which coincides with the point at which nuclear spin statistics can be disregarded. This is because these J_{CH_4} states have contributions from all symmetry modifications which cannot be distinguished by these experiments. As a result the scattering rings for the different co-excitation channels are expected to have radii that are only a single pixel apart or even overlapping. In addition to the blurring in the image caused by the molecular beam parameters, the multitude of available transitions means that the rings are broader than for the other hydrocarbon systems and consequently it is not possible to assign exactly which CH_4 co-products are being formed in conjunction with the NH_3 products from the images.

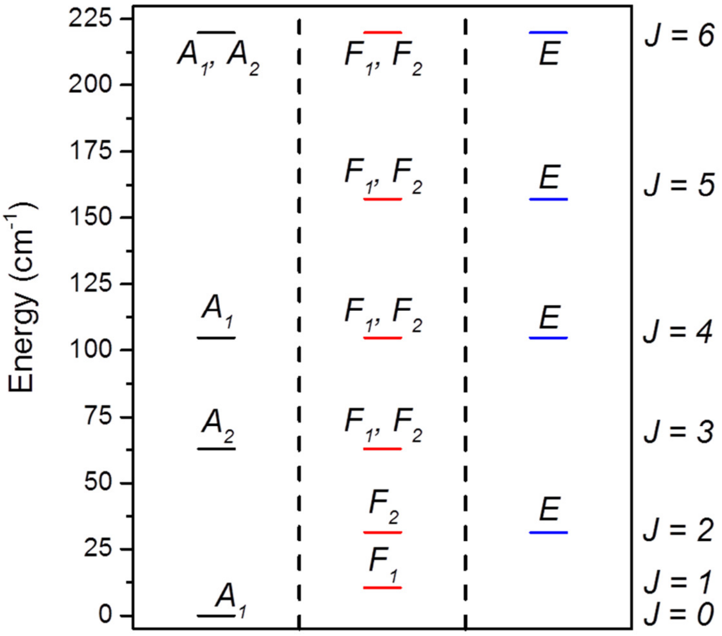

Figure 5.2 Methane rotational energy level diagram for up to $J_{CH_4} = 6$. The symmetries of the energy levels are labelled and correspond to *ortho* (*F*), *para* (*E*) and *meta* (*A*) nuclear spin states.

Based on ΔE of the CH_4 rotational energy levels and the corresponding size and spread of the imaged rings of the NH_3 product states, the range of possible co-excitations are included in Table 5.1. The initial states included are based on a rotational temperature of the molecular beam of 15 K which is determined using the method discussed in Chapter 2.4.2 using a negligible amount of NH_3 leaked into the collider gas mixture.

Table 5.1 Theoretical rotational excitation energies (cm^{-1}) of the CH_4 coproducts formed in conjunction with NH_3 $J_k = 2_1$ products. The energies given are for the transition from the initial state of the CH_4 given in the top row into the final state given by the first column. Slight variation in the observed collision energies for individual J_k product states means there may be slight differences in the actual co-excitation channels observed.

	Initial J state →				
Final J state ↓	0	1	2	3	4
5	n/a	146.6	-	-	-
6	219.9	209.4	188.5	157.0	-
7	293.1	282.7	261.7	230.3	188.4
8	376.8	366.3	345.3	313.9	272.0

Unlike the scattering of NH_3 with CH_4 and D_2, the inelastic scattering of NH_3 with C_2H_6 forms rings with the expected radii as calculated according to Chapter 2.9 This suggests that co-excitation is not occurring which is further supported by the narrower width of the scattering image ring. It is possible that, as the rotational energy levels of C_2H_6 lie so closely together (e.g. a few cm^{-1} apart), the majority of transitions the scattering rings would be expected to be the same radii in pixel terms. In contrast to all the systems described to this point, NH_3-$C(CH_3)_4$ images are larger than calculated. The reason behind this is the very low energy required for rovibrational excitation. The larger image radii indicates that the molecular beams have initial population in the vibrational states that lie 198 cm^{-1} and 203 cm^{-1} above the ground vibrational state.[132] The larger scattering radii of the images results from the vibrational de-excitation of the $C(CH_3)_4$. The specifics of the vibrational levels of $C(CH_3)_4$ and the other consequences observed in the images of the NH_3-$C(CH_3)_4$ scattering are discussed in Section 5.2.4.

Table 5.2 Molecular beam parameters for 25% of each hydrocarbon in 4 bar He including beam velocity and σ, energy of the NH_3 + Hydrocarbon (Hc) collision and the collision energy of NH_3 + He carrier gas atoms.

Collision	**v_2 (ms^{-1})**	**E_{coll} (cm^{-1}) NH_3 + Hc**	**E_{coll} (cm^{-1}) NH_3 + He**
$NH_3 + CH_4$	1398 ± 115	785 ± 115	308
$NH_3 + C_2H_6$	1141 ± 115	740 ± 125	220
$NH_3 + C(CH_3)_4$	807 ± 100	560 ± 100	132

As discussed in Chapter 2.4.5 due to the necessity of seeding the hydrocarbons in helium, the scattering of NH_3 with the He carrier gas is imaged alongside the scatter from the system of interest. All gas mixtures consist of 25% hydrocarbon in 4 bar of He, the reason for the selection of He is discussed in Chapter 2.4.5. This scattering can be observed in the images as the bright smaller inner ring, the relative intensity of which is due to He being the major component of the secondary beam. As the energy is partitioned according to the mass of the colliders (equation 2.13), for the molecular beam parameters produced by the mixture of the hydrocarbons and He, the collision energy available for NH_3-He collisions will result in fewer J_k states being accessible than have been imaged previously.[63, 64] The molecular beam parameters and collision energies available for the NH_3-He scatter for each of the hydrocarbon gas mixtures are included in Table 5.2. The highest energy NH_3 product state imaged for methane collisions is $J_k = 4_1$ and for ethane and neopentane collisions is $J_k = 4_2$. Both of which will exhibit some carrier gas scattering as these states are energetically accessible for NH_3-He within the collision energy spread.

5.2.2 Methane – Images

The images obtained for the inelastic scattering of NH_3 with CH_4 are shown in Figure 5.3. The collision energy for this system is 785 ± 113 cm^{-1}. The NH_3 product states that were successfully imaged are $J_{NH_3} = 2 – 4$, $k = 1 – 4$ where applicable. $J_k = 2_2$ was not imaged due to lack of scattering signal recorded for this product state. Although higher energy NH_3 products should be formed at this collision energy, as found in Chapter 4, the complex spectroscopy of NH_3 means that higher energy states are not sufficiently resolved to be able to image the quantum state specific scattering successfully.

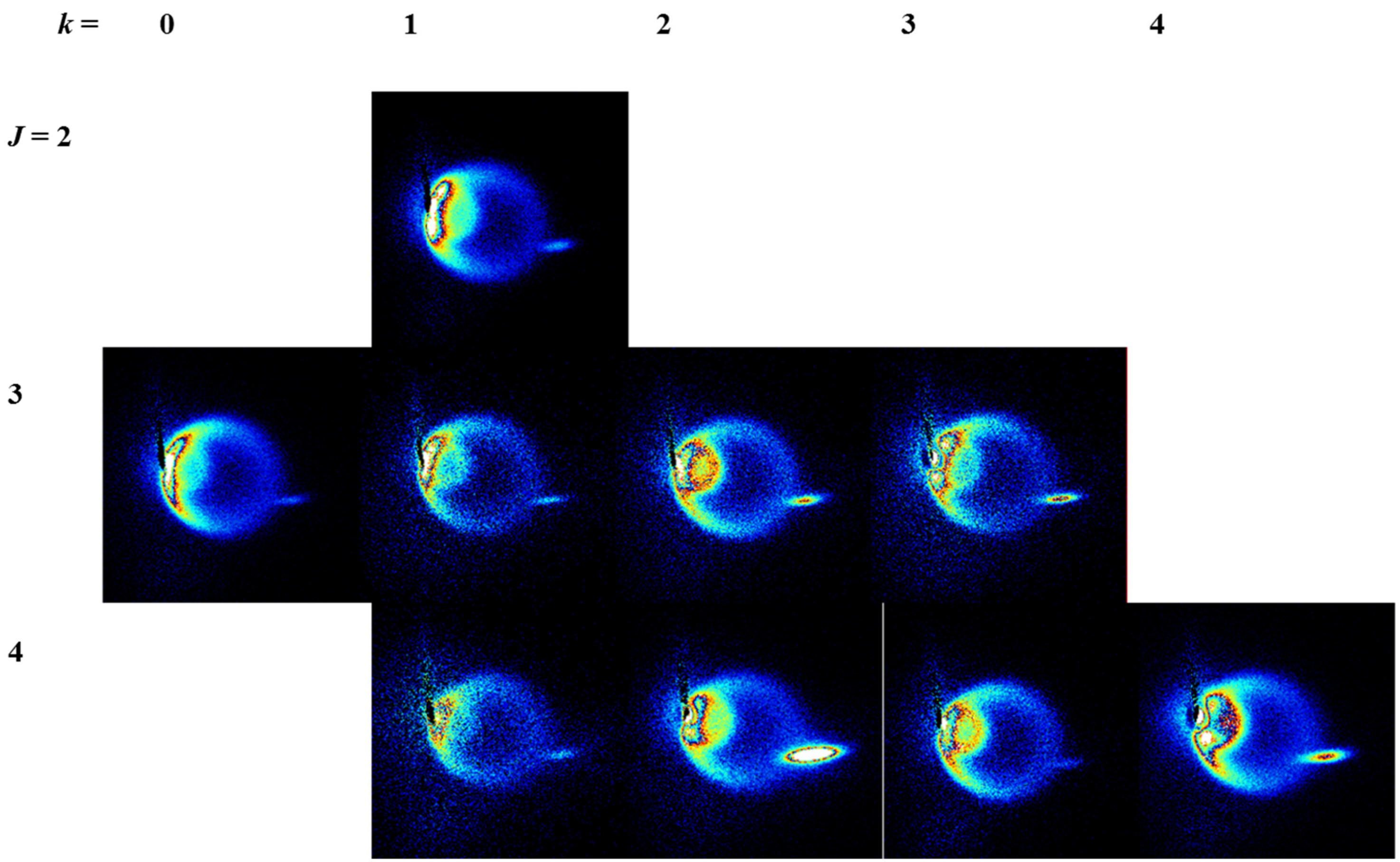

Figure 5.3 Velocity map images of the inelastic scattering of NH_3-CH_4 at a collision energy of 785 ± 115 cm^{-1}. The images are arranged according to *J* down the columns, and increasing *k* across the rows.

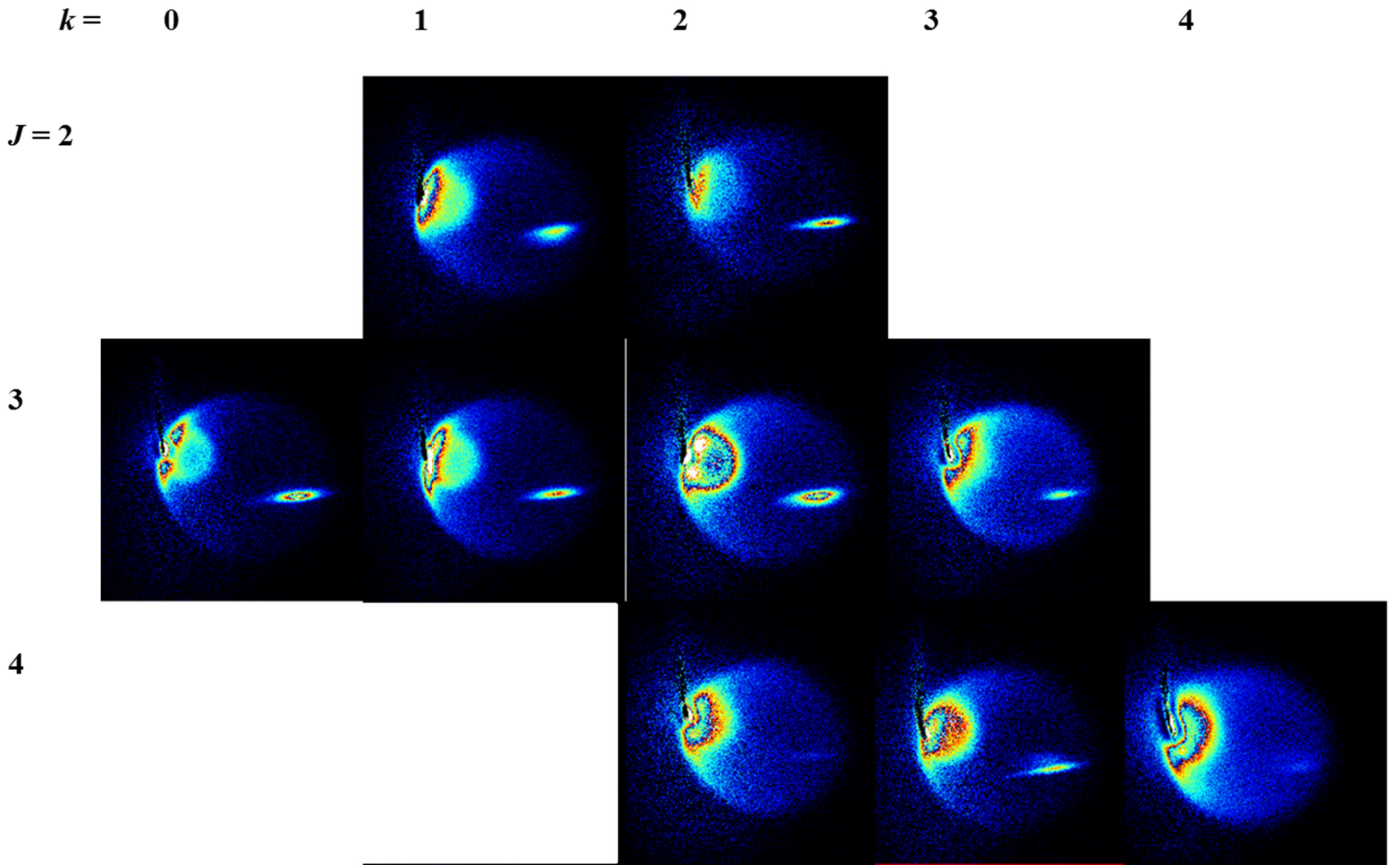

Figure 5.4 Velocity map images of the inelastic scattering of NH_3-C_2H_6 at a collision energy of 740 ± 125 cm^{-1}. The images are arranged according to *J* down the columns, and increasing *k* across the rows.

Much like the scattering observed for NH_3 with Ar and D_2 in Chapters 3 & 4, the images exhibit inelastic scattering into a complete 360° ring with areas of highest intensity in angles where $\theta < 90°$. There are beam spots of unscattered NH_3 that appear in the images for both molecular beams. The second spot is contamination of the secondary beam line resulting from ammonia's use to characterise the molecular beams. As the methane/He mixture has a higher rotational temperature than the NH_3/Ar mixture in the primary beam the secondary beam spot exhibits strong intensity even in the higher energy J_k state images.

5.2.3 Ethane – Images

The experimental images obtained for the inelastic scattering of NH_3 + C_2H_6 at a collision energy of 740 ± 125 cm^{-1} are presented in Figure 5.4. The same selection of J_k product states were imaged with a few changes compared to the NH_3-CH_4 collisions. It was possible to successfully image $J_k = 2_2$ for these collisions, however, the scattering signal into $J_k = 4_1$ was too poor to obtain a dataset viable enough for further analysis. The images are completely dominated by forward scattering. In addition, almost no scattering around the ring is visible beyond the regions where scattering is focussed. This contrasts with the systems previously described in this thesis, where it has been observed that some scattering is visible at all angles and so a complete ring is imaged, even if at times it appears to have regions of low intensity like CH_4. There is very little evidence of the detection bias in the experimental images. This is not entirely surprising as the detection bias is primarily expected to affect scattering into sideward angles ($\theta \approx 60$ - 120°). As with NH_3-CH_4 the primary beam spot is subtracted from the images during acquisition, however, the secondary beam spot not only remains, it overlaps the scattering across pixels that are included in the angular distribution extraction.

5.2.4 Neopentane – Images

Inelastic scattering images for NH_3 with $C(CH_3)_4$ are displayed in Figure 5.5. These have been obtained at a collision energy of 560 ± 100 cm^{-1}. The same set of product states were obtained as for NH_3-C_2H_6. As with the previous collisional pairing the scattering is completely dominated by that into forward angles. These images appear to have less interference from the scattering of NH_3 with the He carrier gas. This is due to the significant mass difference between the two systems in combination with the effect of the larger molecule on the parameters of the secondary molecular beam (see Table

5.2), resulting in a much lower collision energy for the NH_3-He collisions.

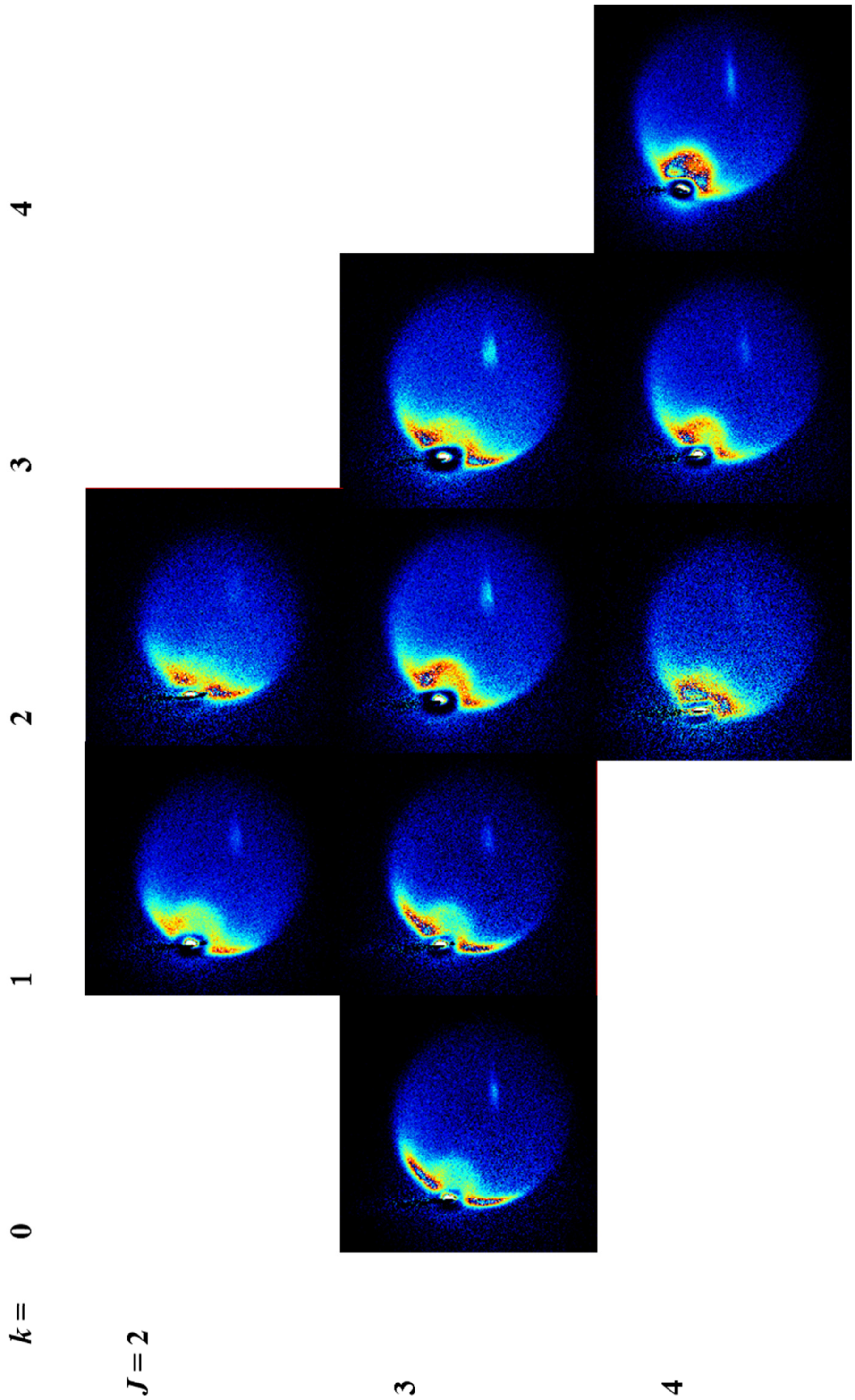

Figure 5.5 Velocity map images of the inelastic scattering of NH_3-$C(CH_3)_4$ at a collision energy of 560 ± 100 cm^{-1}. The images are arranged according to *J* down the columns, and increasing *k* across the rows.

This means the difference in the radii of the two scattering rings is greater relative to the smaller hydrocarbon systems. As mentioned in Section 5.2.1, the $C(CH_3)_4$ images are larger than calculated for collisions where no change in the internal energy of the collider molecules is expected. This is due to vibrational cooling of the ν_4 and ν_{12} modes down to the ground state, the energies of which are detailed in Table 5.3 with the other vibrational modes of $C(CH_3)_4$. The majority of the scattering appears at radius corresponding to this vibrational de-excitation.

Table 5.3 Vibrational states of $C(CH_3)_4$[132] including the vibrational mode number (ν_n), the energy of each state above ν_0 in cm^{-1} and its symmetry. The nature of the vibrations (i.e. bend, stretch etc.) have not been assigned in the literature.

$C(CH_3)_4$ ν_n	**Energy (cm^{-1})**	**Symmetry State**
1	2909	A_1
2	1381	A_1
3	733	A_1
4	198	A_2
5	2955	E
6	1451	E
7	999	E
8	335	E
9	2975	T_1
10	1461	T_1
11	932	T_1
12	203	T_1
13	2959	T_2
14	2876	T_2
15	1475	T_2
16	1372	T_2
17	1256	T_2
18	925	T_2
19	418	T_2

In addition the images appear to be more disc-like rather than consisting of a ring that is consistent with the central slice of a hollow sphere as observed for NH_3 scattering images obtained for collisions with Ar, D_2 and CH_4. The fact that the signal appears in such a defined area suggests that it is 'real' scatter rather than simply background noise. As included in Table 5.3, $C(CH_3)_4$ has a number of low lying vibrational states which are accessible at the experimental collision energy. These vibrational modes have associated rotational quantum states which will result in what could be described as a continuum of possible scattering energies (E_{scatt}) for the NH_3 products if all available internal modes of the $C(CH_3)_4$ have some post-collision population generated. The resulting nested Newton spheres would cause the products to be mapped to all pixels within the area defined by the largest sphere. The Newton diagram in Figure 5.6 illustrates this, although the rotational states are excluded. As the rotational energy levels are spaced <1cm^{-1} apart they would be very tightly packed within the areas between vibrational levels. The scattering radii that the DCSs have been produced for correspond to the NH_3 products formed alongside the vibrational de-excitation of the $C(CH_3)_4$. This region is selected because the remainder of the scattering at lower radii is very isotropic and exhibits only an even distribution in this area of the images.

5.2.5 Differential Cross Sections

Extraction of the DCSs for the scattering of NH_3 with this selection of hydrocarbons has been subject to different processes to those previously utilised. The methods used for each and reasons why are explained in more depth in the sections that relate to each collisional combination below. There are some aspects of this new analysis that apply to all of these systems. In particular it is necessary to subtract the scattering of the NH_3-He from the images before extraction of the experimental angular distributions because this scattering overlaps the ring of interest over a small angular range. This region coincides with the primary beam spot of unscattered NH_3 and the most forward

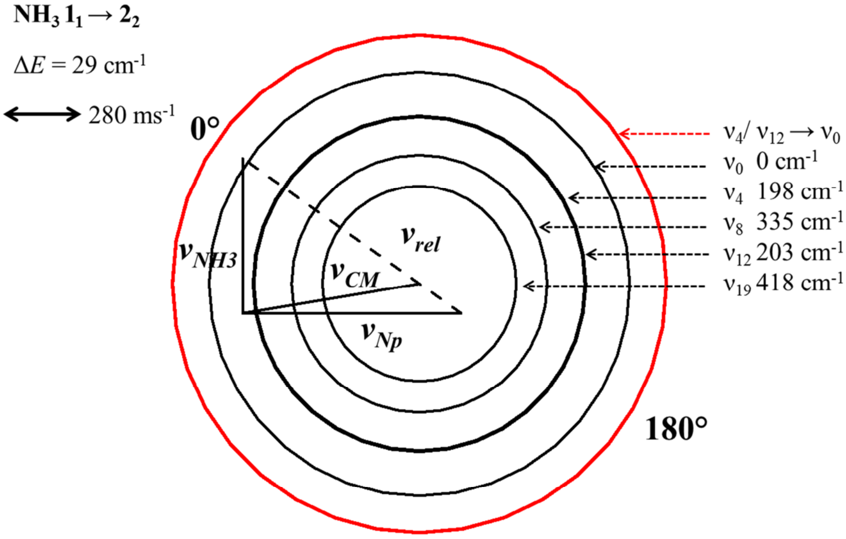

Figure 5.6 Newton diagram for the inelastic scattering of the $J_k = 2_2$ NH_3 product state from collisions with $C(CH_3)_4$. The scattering rings reflect the radii of co-excitation (black) and quenching (red) of vibrational modes of $C(CH_3)_4$ that are accessible at the collision energy of 560 ± 100 cm^{-1}. All excitations assume that the molecules start in ν_0.

scattering angles. The removal of this region is achieved using two methods; the first is to select the inner scattering ring itself and delete an area based on the molecular beam parameters and the expected size of the scattering ring. The next step is to remove a wedge from the triangular pixel array from which the angular distribution is extracted, in order to account for any spread in the NH_3-He scattering that is not accounted for by the initial step. This step is the same as that used in previous chapters to remove any of the beam spot that remains after subtraction in the acquisition process. The angular section that this affects varies according to the collider. The excluded angles are noted in the relevant sections below.

5.2.6 Methane - DCSs

Extracting the DCSs for this system using the forward convolution method used in Chapter 4 was not possible due to the number of rotational quantum states accessible to the CH_4 at the experimental collision energy. Figure 5.7 shows the Newton diagram for NH_3 $J_k = 2_1$ for which $\Delta E = 40$ cm^{-1} and the radii of the scattering rings for the possible co-excitation channels. Based on the width of the rings and taking into consideration the energetics of the collision and the primary initial states of CH_4, there are around 16 possible channels for co-excitation of the CH_4 for each NH_3 product state in these collisions, as discussed in more depth in Section 5.2.1 and shown in Table 5.3. The expected spacing between the rings representing NH_3 scattering with different co-products is calculated to be only 1 or 2 pixels at most, in some cases they overlay each other, see the Newton diagram in Figure 5.7. As a result individually extracting each DCS as done in Chapter 4 would be impossible due to the overlap and unknown weighting of each collisional pathway. Instead the DCSs are extracted using the method that corrects the experimental angular distribution with the instrument function as used in Chapter 3.

The instrument function generated for each NH_3 product state comprises of a sum of the individual simulations for pathways that include the CH_4 co-products formed from the $J_{CH_4} = 2$ state. In order maximise accuracy while minimising computational time only 4 CH_4 states out of the possible 16 in combination with only the most dominant NH_3 excitation for each product state, were used. A single CH_4 initial state was used for the 4 states in order to minimise errors resulting from not weighting the instrument functions when summed as there will be an equal proportion of the initial state available for all excitations. It is not possible to weight the CH_4 excitation channels according to

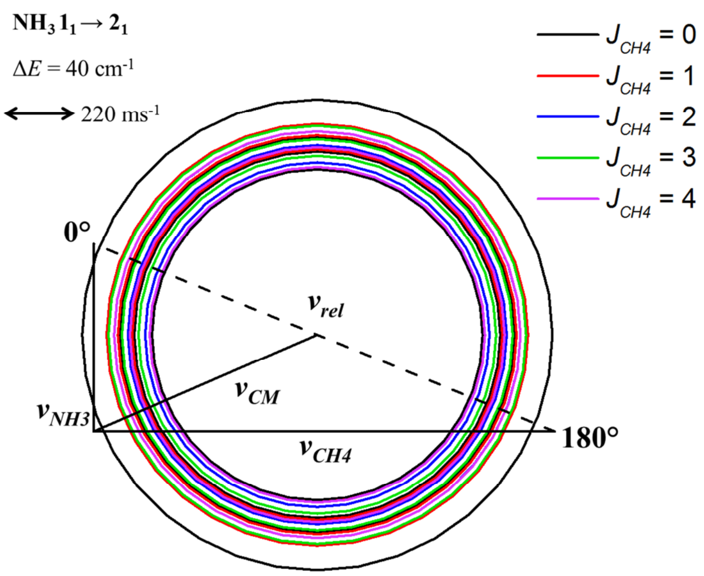

Figure 5.7 Newton diagram illustrating the inelastic scattering of $J_k = 2_1$ NH_3 products from the collisions with CH_4 at a collision energy of 785 ± 115 cm^{-1}. The individual scattering rings represent the scattering formed in conjunction with various CH_4 rotational excitation channels and are colour coded according to the J_{CH_4} initial state for the collisional transitions in Table 5.1. The outer ring is the scattering radius of the NH_3 product when formed with no ΔJ_{CH_4} for comparison.

their probability. As mentioned in Section 5.2.1, all nuclear spin states contribute to the final CH_4 states that scattering appears to be in, however, use of $J_{CH_4} = 2$ as the initial state means that *F* and *E* contributions are accounted for. The instrument functions have been generated using the method as described in Chapter 2.

The mean DCSs, presented in Figure 5.8 across the experimental datasets for all NH_3 product states from the collisions of NH_3-CH_4 are very forward scattered with the majority of signal appearing in angles where $\theta \leq 60°$. In contrast to observations in previous chapters, all the area normalised DCSs are almost identical in terms of shape and intensity within error bars. As mentioned in section 5.2.5, it is necessary to subtract some of the forward scattering region. For methane this results in the removal of $\theta = 0°$ to up to 32° from the final DCSs. Due to the secondary beam spot appearing in regions from which the angular distribution is extracted the removal of θ = 170 - 180° from the final DCSs is also required.

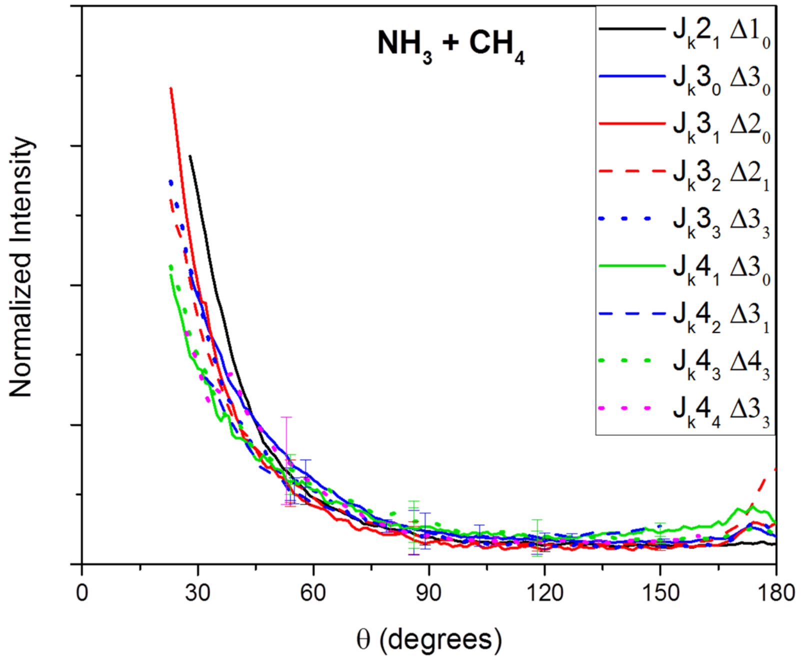

Figure 5.8 The inelastic scattering DCSs for all NH_3 J_k product states obtained for the collisions of NH_3+CH_4 at a collision energy of 785 ± 115 cm^{-1}.

5.2.7 *Ethane – DCSs*

The angular distributions extracted from the DCSs for NH_3-C_2H_6 are almost totally symmetrical about $\theta = 0°$ as demonstrated in Figure 5.9a. This means that correction for the lab frame detection bias that is described in Chapter 2 is unnecessary as it will only distort the slow side (see Figure 5.9b) and contribute additional sources of uncertainty. Note the aim of correcting the data with the instrument function is to achieve a symmetric function but it is not always required, as indicated by Joalland et al. [46] for the reactive scattering of Cl radicals with hydrocarbons. Confirmation that the expected detection bias is not having a strong effect on this data compared to that observed in Chapter 3 & 4 can be noted in the appearance of the scattering of the NH_3-He rings that are imaged simultaneously in Figure 5.4.

In order to produce the final DCSs for each product state of NH_3-C_2H_6 presented in Figure 5.10, unlike the more complex extraction used previously, the raw angular distribution for each experimental image is extracted. This is then normalized by area prior to the dataset being averaged over the lab frame halves. As mentioned in earlier chapters taking a mean is required to account for discrepancies across opposing pixels. These individual averages are then weighted according to image intensity and then the

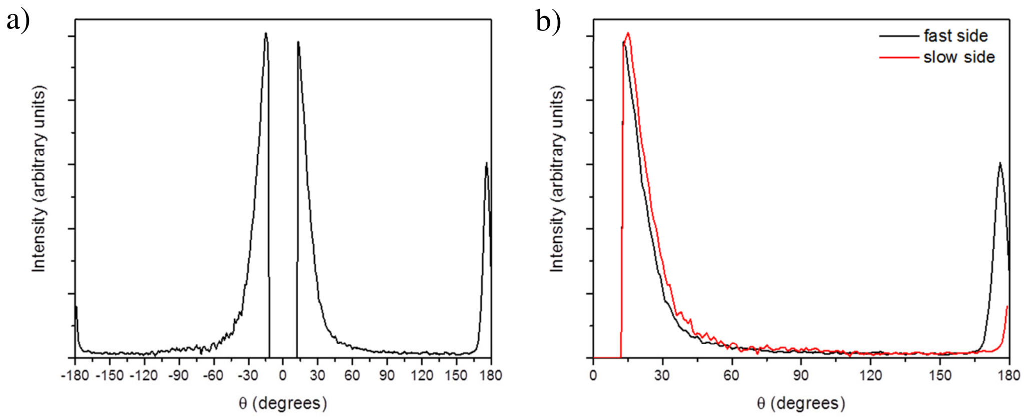

Figure 5.10 a) Raw angular distribution from the experimental image of NH_3 $J_k = 3_0$ product from collisions with C_2H_6 and b) the overlaid Lab frame 'slow' and 'fast' hemispheres. The peak in the angles between θ = 170 - 180° in b) is due to the secondary beam spot and can be disregarded.

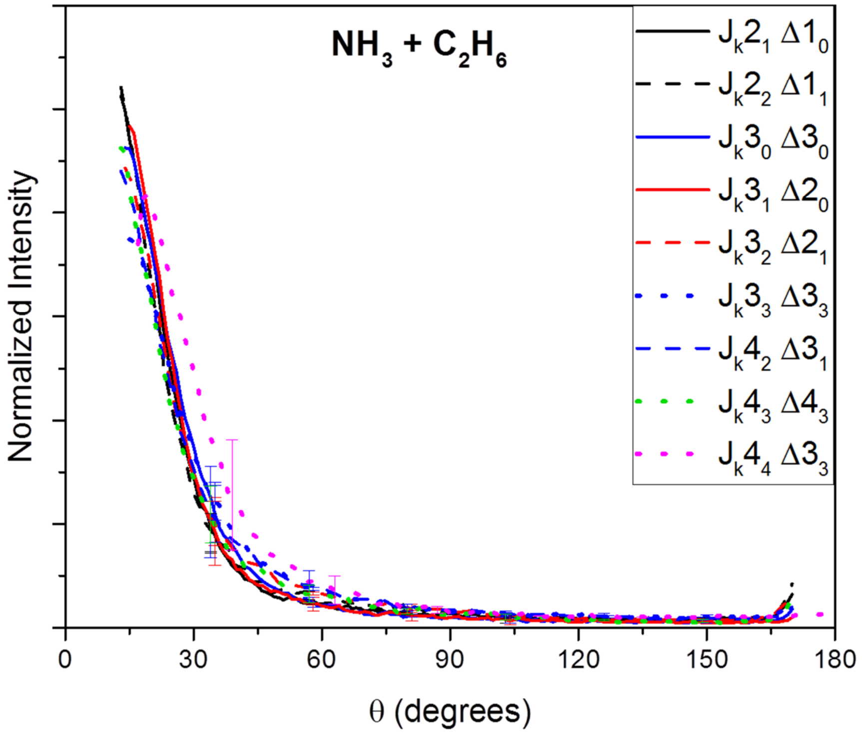

Figure 5.9 The inelastic scattering DCSs for all NH_3 J_k product states obtained for the collisions of NH_3+C_2H_6 at a collision energy of 740 ± 125 cm^{-1}.

mean is taken across the experimental datasets. This produces the set of final DCSs for each NH_3 product state plotted for $\theta = 0$ - 180°. However, due to the beam spot of unscattered NH_3 and the need for the subtraction of the He scatter, the initial point of the DCSs is between $\theta = 13$ - 17°. From its usage to characterise the secondary beam there is a second NH_3 beam spot that due to a coincidence in beam speed and scattering velocity contributes to the raw angular distribution. To remove the effect of this beam spot the angular range between $\theta = 170$ - 180° is excluded from most of the DCSs.

As observed for NH_3-CH_4, there is very little to differentiate between the DCSs of the various NH_3 product states within error bars, as is demonstrated by the single plot of all DCSs included in Figure 5.10. For all states the DCSs are dominated by scattering into $\theta \leq 45°$ with intensity continuing to decrease towards zero for larger angles.

5.2.8 Neopentane – DCSs

As found for the NH_3-C_2H_6 data described in Section 5.2.7, the extracted angular distributions for NH_3-$C(CH_3)_4$ are symmetrical about $\theta = 0°$ and as a result the raw data has been used again to describe the inelastic scattering of this system. The same methods of normalization and averaging of the experimental datasets, as described in the previous section, have been used. The region excluded due to the beam spot and NH_3-He scattering is from $\theta = 0°$ up to $\theta = 20$ - 22°. Unlike the other states the secondary beam spot does not appear within the scattering radii included in the angular distributions, as seen in Figure 5.5, so there is no need to remove any other regions from the DCSs for the NH_3-$C(CH_3)_4$ system.

Once again the DCSs in the single plot for NH_3-$C(CH_3)_4$ collisions in Figure 5.11, demonstrate very little diversity between the NH_3 product states. The scattering is also forward dominated with the bulk of scattering into $\theta \leq 60°$ with a very low signal plateau at higher angles that is higher in intensity than is observed for the NH_3-C_2H_6. This results from the disc-like nature of the scattering image. A more complete comparison between all the NH_3-hydrocarbon scattering results will be made in the next section along with a discussion of the lack of variation that is observed within each system.

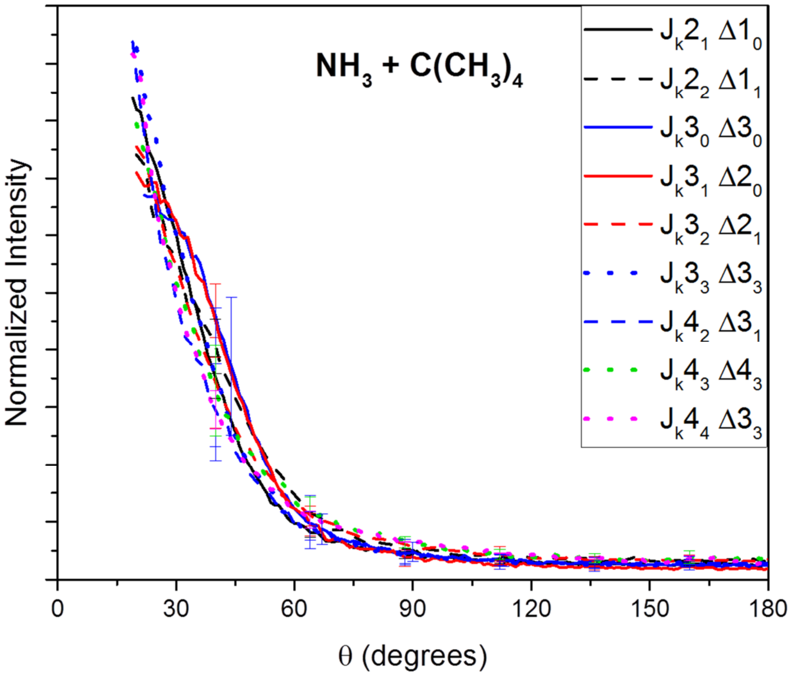

Figure 5.11 The inelastic scattering DCSs for all NH_3 J_k product states obtained for the collisions of NH_3+$C(CH_3)_4$ at a collision energy of 560 ± 100 cm^{-1}.

5.3 Discussion

5.3.1 Comparison of NH_3 + Hydrocarbons scattering

For all NH_3-hydrocarbon systems investigated herein it is observed that, unlike the other systems studied in this thesis, there is no increase in the range of scattering angles as *J* increases for the selection of *J* states imaged. This suggests that as observed when contrasting Ar with smaller noble gases, i.e. He and Ne, the shift to larger colliders that are “softer” due to the increased diffuseness of the electron density changes the nature of the collisions. In the case of Ar this is found to occur because the collision takes place in the more attractive parts of the potential energy surface (PES). Lack of information regarding the PES for the inelastic collisions of NH_3 with CH_4, C_2H_6 and $C(CH_3)_4$ means it is not possible to tell if the attractive forces are dominating in the same way or if the overall increase in steric bulk is the primary factor in the apparent disappearance of this trend. However, due to the long range nature of the van der Waals forces that would result from the increased size of these molecules, the attractive interactions are going to govern the nature of the surface that the collisions are occurring up on. It may be that much higher J states exhibit the increase in angular distribution, however, as there is not sufficient spectroscopic resolution for these experiments, product states where $J > 4$ have not been imaged successfully.

Much like the NH_3-D_2 system, discussed in Chapter 4.3.1, the forwards dominated scattering is counterintuitive with respect to the impact parameters that are expected to result in the rotational excitation of the NH_3. Once again the forwards scattering is indicative of a PES that favours long range attractive interactions. However, the very glancing interaction with the hydrocarbon is sufficient that enough torque is generated to rotationally excite the NH_3 with little alteration to the direction of propagation. Such behaviour has been observed previously on a much smaller scale for H + D_2 for the vibrational excitation of the D_2 and has been designated as a “tug-of-war” collision.[133]

In these types of interaction two (or in the case of NH_3 possibly more) of the atoms experience a strong attractive interaction resulting in the distortion of any chemical bonds they have. As the particles lack sufficient energy to break their respective bonds they eventually part, resulting in a recoil motion along the D_2 bond causing vibrational excitation.[133] In the case of NH_3 with the hydrocarbon colliders, the attractive interaction is not observed to alter the vibrational energy as there is insufficient energy to achieve this. However, as the molecules pass each other the interaction is sufficient to impart additional torque to the rotational motion while only slightly deflecting the direction of the translation.

An initial comparison of the DCSs from the three scattering combinations, as presented in Figure 5.12 for each NH_3 product state, reinforces the similarities that have previously been observed within each dataset. This resemblance is not entirely surprising because, though there is currently a lack of information about the PESs for these systems, the structure of the colliders suggests that during collision the NH_3 will predominately experience a comparable H environment. However, if the DCSs are considered more carefully it becomes apparent that there are a range of subtle differences between each hydrocarbons collision.

The clear difference that is observed is the range of scattering angles despite all systems being principally forward scattered. The NH_3-C_2H_6 system exhibits scattering into a narrower range of angles by ~15° than the other two systems. It can be suggested that the explanation for this difference is the shape of the collider molecules; C_2H_6 is a linear molecule whereas both CH_4 and $C(CH_3)_4$ are spherical. The molecular configuration

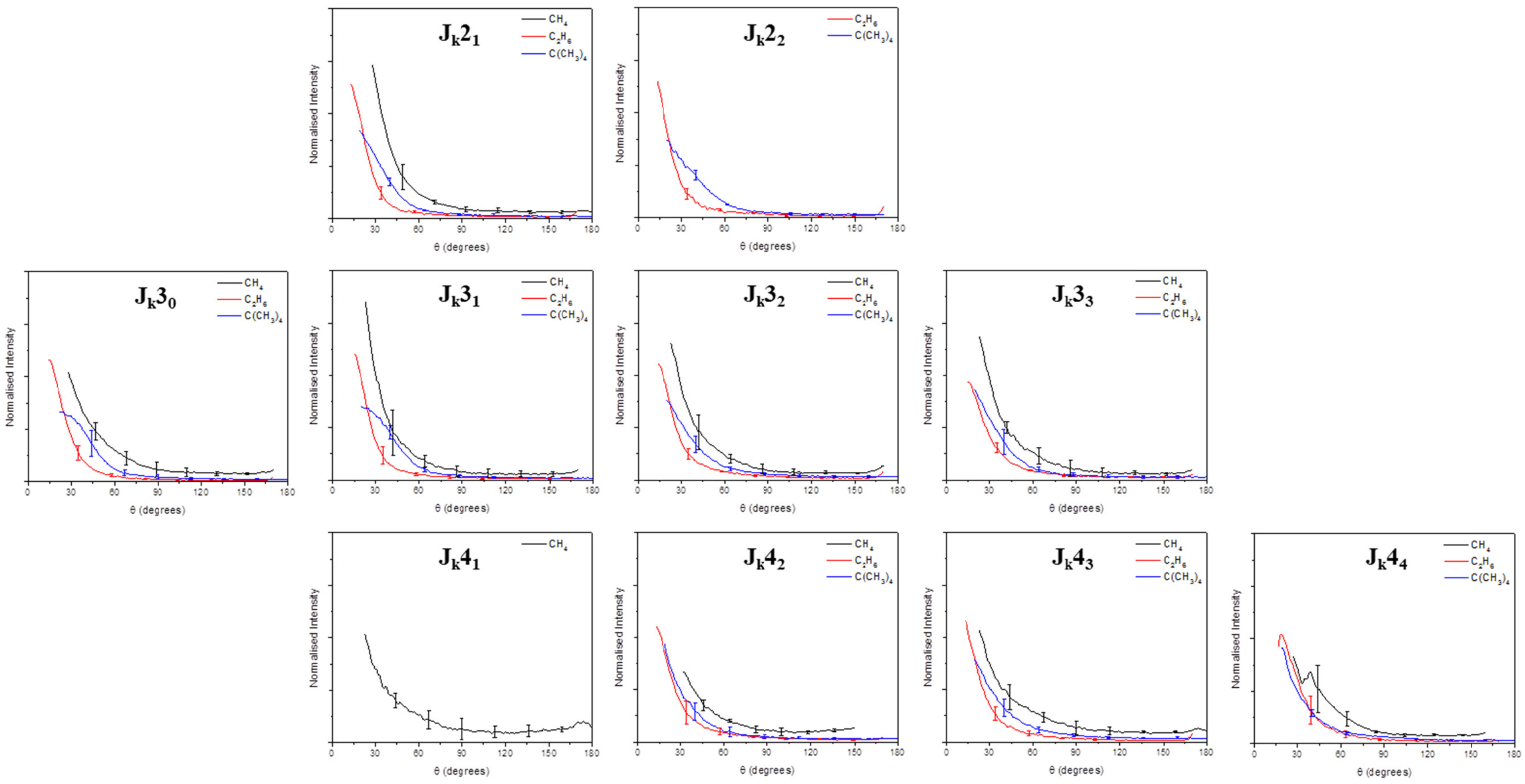

Figure 5.12 Experimentally obtained DCSs for the NH_3 product states for the collision of NH_3 with hydrocarbon colliders. Where the collider for black plots is CH_4, red plots is C_2H_6 and blue plots is $C(CH_3)_4$. The NH_3 product state represented by each graph is labelled.

results in the electron density distribution around the collider molecules being different, potentially resulting in a change in the interaction of the NH_3 with the linear molecule compared to the spherical ones. Given the similarities in the scattering angles for the spherical molecules, it is likely that their PESs share more similar characteristics.

Beyond the differentiation of the NH_3-C_2H_6 through its scattering angles, the DCSs of the NH_3-CH_4 can be distinguished through their shape. The curves of the DCSs for NH_3-CH_4 can be described as exponential in nature whereas those of the other two collision systems appear to be more bilinear in shape. The variance of shape is indicative of the difference in the nature of the collisions. As discussed in Section 5.2.1, the NH_3-CH_4 scattering rings suggest that this is the only one of the three hydrocarbon systems studied undergoing detectable co-excitation. As CH_4 and NH_3 are very similar in mass, 16 and 17 amu respectively, the collision energy is expected to be partitioned much more equally compared to the collisions with the larger ethane (30 amu) and neopentane (72 amu). The sizes of CH_4 and NH_3 are also more similar than the other collision pairs, this could result in a much closer interaction between the colliders than that of NH_3 with the larger hydrocarbons. This closer interaction could influence the characteristics of the scattering ring such as the low intensity plateau observed in higher θ for NH_3-CH_4 which does not appear in the other DCSs but does appear in the scattering of NH_3 with atomic and diatomic species.

5.3.2 Comparison to NH_3 + Ar

As ethane and neopentane lay either side of Ar in terms of mass the considerable differences in the nature of the scattering of NH_3 in collisions with these molecules compared to the atomic system is down to the more diffuse and soft nature of the molecules. When compared to the NH_3-Ar DCSs, from Chapter 3, the range of scattering is restricted to a significantly narrower angular range. A more valid comparison is if the NH_3-Ar collisions are assessed with respect to NH_3-CH_4, which is a much more comparable system in terms of the estimated collisional cross-section, with values of 9.3 and 13.8 $Å^2$, respectively, in contrast to cross sections of 25.9 and 42.2 $Å^2$ for NH_3-C_2H_6 and NH_3-$C(CH_3)_4$. These are calculated from equation 1.12, using the van der Waals radius to describe Ar and the sum of the bond lengths in a single plane to approximate the molecular the radius. The immediate observation is that the images are more alike, with at least some scattering intensity appearing at all angles. However, in comparing the DCSs, for which selected plots are included in Figure 5.13, it becomes obvious that the bimolecular collisions are much more forward scattered.

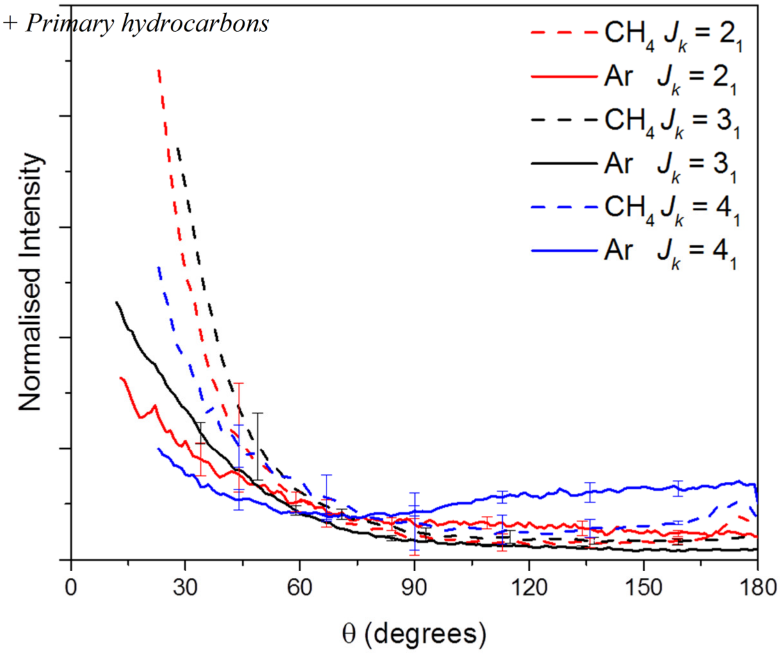

Figure 5.13 The DCSs for NH_3-CH_4 and NH_3-Ar comparison for $k = 1$ NH_3 product states

Elements that appear to influence the scattering of NH_3 with an atomic system like Ar, such as the angle of approach for the collider, will have a different effect when the collider is a polyatomic. The PES of a bimolecular collision is governed by a number of additional elements that arise from the additional degrees of freedom that are associated with molecular systems. Specifically, the orientation of both molecules upon collision with respect to their own symmetry axes as well as the dihedral angles describing the direction of approach. It would be expected that the orientation of the collider molecule, particularly in the case of linear systems such as C_2H_6, would be as influential as the orientation of the NH_3 upon collision. In cases where the collider molecule is much larger than NH_3, such as $C(CH_3)_4$, it is possible the collision interaction will instead be governed by the hydrocarbon instead of the NH_3.

Drawing comparisons with other systems is not currently possible as inelastic scattering of two such polyatomics has not previously been documented. The hydrocarbon collisions with NH_3 are currently beyond quantum scattering calculation capabilities as there are no existing PESs. There are very few examples of PESs for interactions for many atom systems. For inelastic scattering interactions, the largest systems consist of ~7 atoms,[59] however, larger systems have been modelled for reactive scattering.[115, 134]

5.4 Summary

Chapter 5 has presented the first inelastic scattering DCSs for the collisions of NH_3 with methane, ethane and neopentane. In addition, these are the first VMI images for the inelastic scattering of a completely polyatomic collision. Across the three scattering systems included, there is very little variation across the DCSs product J_k states for each collisional pairing. However, the images clearly exhibit rotational excitation of CH_4, vibrational quenching of the $C(CH_3)_4$ and no change to the excitation of the C_2H_6. Despite this range of co-excitation behaviour, the NH_3 product scattering is typically dominated by scattering that is forwards in direction. It is therefore suggested that the nature of these interactions as experienced by the NH_3 is very similar in all three environments and is therefore due to long range attractive interactions with the primary hydrogens that are found on all hydrocarbons investigated.

Additionally, in order to generate sufficient torque for the rotational excitation of the NH_3 whilst maintaining a forwards trajectory it is proposed that the PESs (which at present are unknown for all systems) produce an interaction similar to that observed for "tug-of-war" type collisions.[133] Information regarding the PES and quantum scattering calculations would only add to the understanding of why the scattering is so forward in nature. Theory would also clarify if the subtle variations within collision systems are correctly described through the more classical concepts presented in Section 5.3.1 or if quantum effects still play a role for the smaller bimolecular collisions.

Chapter 6 – Conclusions

This thesis has expanded existing literature of the inelastic scattering of NH_3. The inelastic collisions of NH_3-Ar and NH_3-D_2 have been compared to previous experiments carried out on the same apparatus studying CD_3 with the same colliders.[62, 77] Evaluating collisions with these two molecules allows the scattering of a closed-shell system, in NH_3, to be contrasted with an open-shell system, CD_3. In addition, it has presented, to the best of my knowledge, the first differential cross sections (DCSs) of polyatomic-polyatomic inelastic collisions in the form of the scattering of NH_3 with three hydrocarbons of increasing size.

As described in Chapter 2, the primary experimental technique used was crossed molecular beam velocity map imaging (CMB-VMI) in conjunction with resonance enhanced multiphoton ionization (REMPI) spectroscopy to state-selectively record the scattering velocities of the NH_3 collision products. DC slice imaging[17] is employed in order to record only the scattering products at the centre of the ion packet that are thus parallel to the detector. This allows for a DCS to be extracted directly from the raw angular distribution using a simple density-to-flux transformation instead of complex forward convolution methods.

6.1 NH_3 – atomic inelastic scattering

The first sets of VMI images and DCSs presented in this thesis were for the inelastic scattering of NH_3-Ar. There is existing literature on this system, although the DCSs presented are for nearly four times the collision energy[69] than the experiments conducted herein, and exhibit very different scattering as a result (see Chapters 1 and 3). The DCSs acquired in this work are very similar to existing DCSs of ND_3-Ar[66] that have been obtained at collision energies like those used herein. It was clear from the images that the scattering angle exhibits a tendency towards larger angles as J increased. This supports what has previously been observed for other rare gas molecules with ND_3.[63, 70] Despite this, the collisions of NH_3-Ar are typically more forwards scattered than with Ne and He. This has been found previously for ND_3-Ar[66] and is supported by the DCSs produced herein. The cause of this behaviour is the nature of the interactions and the region of the potential energy surface (PES) that they occur on. NH_3-Ar is dominated by long-range attractive interactions in an energy well that is considerably deeper than smaller rare gas systems such as He and Ne.[74] This is due to the increased mass of the Ar and the fact that it is easily polarized due to its more diffuse electronic structure.

The DCSs also show that the angular distribution of the scattering products has a dependency on k, where the range of scattering angles decreases as k increases; specifically the probability of scattering into sideways and backwards directions decreases. This can be clearly observed in quantum states where $J_{\mathrm{NH_3}} = 3$, and is also visible in the other $J_{\mathrm{NH_3}}$ states measured, it occurs across the datasets irrespective of the nuclear spin modification of the quantum state in question. This is the first discussion of this trend even though it can be observed in the DCSs previously reported for other systems (see for example references 66 and 70). A classical approach is taken in order to explain this trend, however, there are numerous influences in the NH_3-Ar scattering that could relate to this. None of the factors that were considered, such as the type of collisional excitation, the direction of approach and angle of interaction, can explain this trend by themselves. An approach that would, instead, consider all of these factors and other quantum effects is required.

6.2 NH_3 - diatomic inelastic scattering

Chapter 4 describes the first investigation of NH_3-D_2 collisions, however, DCSs have been published for the collisions of the isotopologues ND_3-H_2.[73] D_2 has several rotational excitations that are energetically accessible at the collision energy in use. Consequently, the rotational co-excitation of the D_2 into several channels is observed. This co-excitation appears as differences in the scattering radii of the NH_3 products with respect to the scattering centre. Rotational excitation of the D_2 into two different rotational states is observed in the NH_3 VMI images alongside scattering formed in conjunction with no change in the D_2 rotational state ($\Delta J_{\mathrm{D_2}} = 0$). However, image resolution results in the overlap of the individual product channel Newton spheres. D_2 has a large rotational constant[78] and therefore the energy levels lie hundreds of cm^{-1} apart, however, this is only a few pixels in the experimental images. It has been found that, by using a forward convolution approach to fit simulated instrument functions to the experimental data, it is possible to obtain individual DCSs for each collision channel.

Individual DCSs have been extracted for each NH_3 J_k state and its D_2 co-product channels. Except for $J_k = 4_3$ and $J_k = 5_3$, which are the *ortho*-NH_3 product states with the largest excitation energies that have been measured, the majority of scattering is into angles where $\theta < 90°$. For the two product states mentioned, the DCSs tend towards isotropic for the $J_{\mathrm{D}_2} = 0 \rightarrow 2$ co-excitation channel. However, comparison of the raw angular distributions and the DCSs suggest that the method of extracting the DCSs needs further refining in order to more successfully fit the data when the signal peak shifts away from $\theta = 0°$. As such these states may exhibit more backwards scattering than is indicated by the DCS.

It is found that excitation of the lowest *para* D_2 reagent rotational state, $J_{\mathrm{D}_2} = 1$, exhibits a surprising preference for large impact parameters. In addition to which, the scattering of the NH_3 product states, i.e. $J_{\mathrm{NH}_3} = 2$, that are formed in conjunction with this channel, is dominated by scattering into forwards angles. It is suggested that for the D_2 to undergo additional excitation, from an already rotating state, it must interact with the shallow gradient of an attractive region of the PES a long way from the NH_3 nuclei. Steeper gradients on the PES may inhibit rotational excitation of the D_2 so, as the impact parameter decreases, the probability of D_2 excitation through this channel also decreases to nearly zero.

Chapter 4 also introduced a new method for extracting the DCSs of all product co-excitation channels. This method of DCS extraction does not work for molecules where the co-excitation states lie much closer together, such as CH_4 (as discussed in Chapter 5) which has rotational level spacings of tens of cm^{-1}. On the scale of the images this results in a separation of ~1 pixel and therefore the exact transitions of the possible rotational states that are energetically accessible cannot be assigned with any certainty, particularly as there are a range of initial states available, resulting in some transitions having the same energy.

6.3 NH_3-polyatomic inelastic scattering

As presented in Chapter 5, the inelastic collisions of NH_3 with various hydrocarbons results in observable co-excitation of the CH_4, vibrational cooling of the $C(CH_3)_4$ and no measurable change to the C_2H_6. The hydrocarbons studied in collisions with NH_3 were selected because of the primary nature of their hydrogens. Despite the range of effects the NH_3 collisions have on the hydrocarbons, the DCSs presented for the NH_3 collisional products are incredibly similar for all three systems. It is suggested as the interactions are expected to be dominated by long range attractive forces that the similarities between the DCSs of collision systems is not as striking as it first appears because the NH_3 will experience comparable environments due to the similarity in the hydrogen environments. The DCSs are all the same within error bars cross the J_k product states for each collisional system, as well as the system-to-system similarity.

The nature of the scattering to this point can be directly tied to the computational PESs of the collisions proving how interdependent experimental and theoretical work is, particularly when describing and understanding the dynamics of a collision. As the PESs for the NH_3-hydrocarbon collision systems have not been calculated, the description of the behaviour is only speculative. Nonetheless, the DCSs acquired experimentally are indicative of the characteristics of the PESs. The scattering of NH_3 is dominated by forwards angle ($\theta \leq 60°$) for all three hydrocarbons, however rotational excitation of the NH_3 is still occurring. As such additional torque must be being generated through long range interactions that result in only minimal deflection to the direction of motion. The suggested mechanism for these collisions is that the collisional interaction is similar to the "tug-of-war" type inelastic collisions[133] that have been observed for collisions of H + D_2, which result in the vibrational excitation of the D_2. Future computational work may develop to allow for the PES for some of these bimolecular collisions to be modelled and for quantum scattering or quasi-classical trajectory calculations to be performed. This would allow for confirmation of the mechanism of the behaviour being observed.

One goal in studying the inelastic collisions of such large molecules is to test the ability of such molecules that could be considered liquid surface mimics in the gas phase. Using liquid surfaces in conjunction with VMI is not currently a viable option due to the problems with evaporation. $C(CH_3)_4$ is on the threshold of being large enough to be considered as a liquid surface mimic. In using such large molecules additional complexities arise with the other experimental techniques used, such as achieving suitable collisional cooling in the molecular beam as discussed within Chapter 2. With improvements in vacuum technology and pulsed nozzle techniques, achieving suitable molecular beam temperatures is not impossible. However, the experimental apparatus would need to be designed with the cooling of large molecules specifically in mind.

6.4 Outlook

The focus of these experiments has been to obtain an overview of bimolecular inelastic collisions of such a size. In contrast, the majority of current work investigating collisional dynamics has been to expand the existing knowledge of diatomic systems with noble gases. These systems have been used to test new experimental techniques and to measure additional parameters, as our understanding of the field has increased. One key technique that has evolved is Stark deceleration. Due to the length of the deceleration path, often several metres in length,[36] these have allowed experimentalists to gain additional control over the initial state of molecule of interest and to control the collision energy, therefore allowing access to very low energy collision regimes that have previously only been accessible through theoretical investigations.[103, 135] As these investigations are only in their infancy, the focus has been on diatomics and atomic systems much like early crossed molecular beam experiments. As has been noted, bimolecular collisions offer considerable scope for future investigation and no doubt this field will eventually result in the design of an experimental apparatus that allows for the deceleration of two molecular beams in order to achieve control over a bimolecular system. This would help immeasurably in deciphering the data, as seen in this thesis, the mix of initial states results in complex scattering images even for a polyatomic with a diatomic such as D_2.

More widely, the expansion of the bimolecular collisions studied is necessary. For those collisions that are inelastic in nature, their importance to solution based chemistry is poorly understood. Particularly, how the effect of interactions of a reactant with the solvent may later affect the reaction process and the dissipation of energy post-reaction, although some progress in this area is being made through the use of ultrafast transient absorption spectroscopy[136, 137] and new simulation methods.[138] This has only been possible with the development of faster laser systems and more powerful computers, ideally, as technology evolves so should this field and any that grow out of it.

I have focussed on types of collisions relevant to this work although there is considerable scope for molecular beam scattering using radicals, as seen in the CD_3 work that has been referred to in this work.[62] In addition, collisions of ions and the resulting charge transfer also has numerous possibilities and important implications to the field of astrochemistry. There are so many potential branches that could add to the collective knowledge around reaction dynamics, and this makes it a very exciting area of science to be involved with.

References

1. M. Brouard and C. Vallance, *Tutorials in molecular reaction dynamics*, Royal Society of Chemistry, Cambridge, 2010.

2. M. Born and R. Oppenheimer, *Annalen Der Physik*, 1927, **84**, 0457.

3. P. W. Atkins and R. Friedman, *Molecular quantum mechanics*, Oxford University Press, Oxford, 2011.

4. P. W. Atkins and J. De Paula, *Atkins' physical chemistry*, Oxford University Press, Oxford, 2010.

5. P. W. Atkins, *Quanta : a handbook of concepts*, Clarendon Press, Oxford, 1974.

6. M. Brouard, *Reaction dynamics*, Oxford University Press, Oxford, 1998.

7. Y. T. Lee, J. D. McDonald, P. R. Lebreton and Herschba.Dr, *Review of Scientific Instruments*, 1969, **40**, 1402.

8. D. J. Garton, T. K. Minton, W. F. Hu and G. C. Schatz, *Journal of Physical Chemistry A*, 2009, **113**, 4722.

9. J. M. Zhang, D. J. Garton and T. K. Minton, *Journal of Chemical Physics*, 2002, **117**, 6239.

10. D. J. Garton, T. K. Minton, M. Alagia, N. Balucani, P. Casavecchia and G. G. Volpi, *Journal of Chemical Physics*, 2000, **112**, 5975.

11. W. Gerlach and O. Stern, *Zeitschrift Fur Physik*, 1921, **8**, 110.

12. O. Stern, *Zeitschrift Fur Physik*, 1920, **2**, 49.

13. W. C. Wiley and I. H. McLaren, *Review of Scientific Instruments*, 1955, **26**, 1150.

14. D. W. Chandler and P. L. Houston, *Journal of Chemical Physics*, 1987, **87**, 1445.

15. D. H. Parker and A. Eppink, *Journal of Chemical Physics*, 1997, **107**, 2357.

16. B. J. Whitaker, *Imaging in molecular dynamics : technology and applications : (a user's guide)*, Cambridge University Press, Cambridge, 2003.

17. D. Townsend, M. P. Minitti and A. G. Suits, *Review of Scientific Instruments*, 2003, **74**, 2530.

18. C. R. Gebhardt, T. P. Rakitzis, P. C. Samartzis, V. Ladopoulos and T. N. Kitsopoulos, *Review of Scientific Instruments*, 2001, **72**, 3848.

19. J. J. Lin, J. G. Zhou, W. C. Shiu and K. P. Liu, *Review of Scientific Instruments*, 2003, **74**, 2495.

20. J. J. John, M. Brouard, A. Clark, J. Crooks, E. Halford, L. Hill, J. W. L. Lee, A. Nomerotski, R. Pisarczyk, I. Sedgwick, C. S. Slater, R. Turchetta, C. Vallance, E. Wilman, B. Winter and W. H. Yuen, *Journal of Instrumentation*, 2012, **7**, 14.

21. A. Nomerotski, M. Brouard, E. Campbell, A. Clark, J. Crooks, J. Fopma, J. J. John, A. J. Johnsen, C. Slater, R. Turchetta, C. Vallance, E. Wilman and W. H. Yuen, *Journal of Instrumentation*, 2010, **5**, 7.

22. G. Scoles, *Atomic and molecular beam methods*, OUP, New York, N.Y., 1988.

23. J. M. Hollas, *Modern spectroscopy*, John Wiley & Sons, Chichester, 2004.

24. F. J. Aoiz, M. Brouard, S. D. S. Gordon, B. Nichols, S. Stolte and V. Walpole, *Physical Chemistry Chemical Physics*, 2015, **17**, 30210.

25. M. S. Elioff and D. W. Chandler, *Journal of Chemical Physics*, 2002, **117**, 6455.

26. M. Brouard, H. Chadwick, S. D. S. Gordon, B. Hornung, B. Nichols, F. J. Aoiz and S. Stolte, *Journal of Chemical Physics*, 2016, **144**, 17.

27. M. Brouard, H. Chadwick, S. D. S. Gordon, B. Hornung, B. Nichols, F. J. Aoiz and S. Stolte, *Journal of Physical Chemistry A*, 2015, **119**, 12404.

28. J. Onvlee, A. van der Avoird, G. Groenenboom and S. Y. T. van de Meerakker, *Journal of Physical Chemistry A*, 2016, **120**, 4770.

29. J. Onvlee, S. N. Vogels, A. D. van der Avoird, G. C. Groenenboom and S. Y. T. van de Meerakker, *New Journal of Physics*, 2015, **17**, 16.

30. S. N. Vogels, J. Onvlee, S. Chefdeville, A. van der Avoird, G. C. Groenenboom and S. Y. T. van de Meerakker, *Science*, 2015, **350**, 787.

31. G. Sarma, A. K. Saha, J. J. ter Meulen, D. H. Parker and S. Marinakis, *Journal of Chemical Physics*, 2015, **142**, 7.

32. G. Sarma, S. Marinakis, J. J. ter Meulen, D. H. Parker and K. G. McKendrick, *Nature Chemistry*, 2012, **4**, 985.

33. H. C. Schewe, Q. L. Ma, N. Vanhaecke, X. A. Wang, J. Klos, M. H. Alexander, S. Y. T. van de Meerakker, G. Meijer, A. van der Avoird and P. J. Dagdigian, *Journal of Chemical Physics*, 2015, **142**, 13.

34. M. L. Costen, R. Livingstone, K. G. McKendrick, G. Paterson, M. Brouard, H. Chadwick, Y. P. Chang, C. J. Eyles, F. J. Aoiz and J. Klos, *Journal of Physical Chemistry A*, 2009, **113**, 15156.

35. D. H. Zhang and H. Guo, in *Annual Review of Physical Chemistry, Vol 67*, eds. M. A. Johnson and T. J. Martinez, Annual Reviews, 2016, 67, 135.

36. J. Onvlee, S. N. Vogels, A. von Zastrow, D. H. Parker and S. Y. T. van de Meerakker, *Physical Chemistry Chemical Physics*, 2014, **16**, 15768.

37. C. Waring, K. L. King, P. A. J. Bagot, M. L. Costen and K. G. McKendrick, *Physical Chemistry Chemical Physics*, 2011, **13**, 8457.

38. P. A. J. Bagot, C. Waring, M. L. Costen and K. G. McKendrick, *Journal of Physical Chemistry C*, 2008, **112**, 10868.

39. T. R. Sharples, T. F. M. Luxford, D. Townsend, K. G. McKendrick and M. L. Costen, *Journal of Chemical Physics*, 2015, **143**, 12.

40. J. D. Steill, J. J. Kay, G. Paterson, T. R. Sharples, J. Klos, M. L. Costen, K. E. Strecker, K. G. McKendrick, M. H. Alexander and D. W. Chandler, *Journal of Physical Chemistry A*, 2013, **117**, 8163.

41. J. J. Kay, J. D. Steill, J. Klos, G. Paterson, M. L. Costen, K. E. Strecker, K. G. McKendrick, M. H. Alexander and D. W. Chandler, *Molecular Physics*, 2012, **110**, 1693.

42. H. Chadwick, M. Brouard, Y. P. Chang, C. J. Eyles, G. McCrudden, T. Perkins, S. A. Seamons, J. Klos, M. H. Alexander, P. J. Dagdigian, D. Herraez-Aguilar and F. J. Aoiz, *Journal of Chemical Physics*, 2014, **140**, 14.

43. H. Chadwick, M. Brouard, Y. P. Chang, C. J. Eyles, T. Perkins, S. A. Seamons, J. Klos, M. H. Alexander and F. J. Aoiz, *Journal of Chemical Physics*, 2012, **137**, 14.

44. M. Brouard, H. Chadwick, Y. P. Chang, C. J. Eyles, F. J. Aoiz and J. Klos, *Journal of Chemical Physics*, 2011, **135**, 17.

45. B. Joalland, Y. Y. Shi, A. D. Estillore, A. Kamasah, A. M. Mebel and A. G. Suits, *Journal of Physical Chemistry A*, 2014, **118**, 9281.

46. B. Joalland, Y. Y. Shi, N. Patel, R. Van Camp and A. G. Suits, *Physical Chemistry Chemical Physics*, 2014, **16**, 414.

47. N. Herath and A. G. Suits, *Journal of Physical Chemistry Letters*, 2011, **2**, 642.

48. C. Huang, W. Li, A. D. Estillore and A. G. Suits, *Journal of Chemical Physics*, 2008, **129**, 6.

49. C. S. Huang, W. Li and A. G. Suits, *Journal of Chemical Physics*, 2006, **125**.

50. W. Li, C. S. Huang, M. Patel, D. Wilson and A. Suits, *Journal of Chemical Physics*, 2006, **124**.

51. J. M. Bowman and A. G. Suits, *Physics Today*, 2011, **64**, 33.

52. A. G. Suits, *Accounts of Chemical Research*, 2008, **41**, 873.

53. D. Townsend, S. A. Lahankar, S. K. Lee, S. D. Chambreau, A. G. Suits, X. Zhang, J. Rheinecker, L. B. Harding and J. M. Bowman, *Science*, 2004, **306**, 1158.

54. W. B. Chapman, A. Kulcke, B. W. Blackmon and D. J. Nesbitt, *Journal of Chemical Physics*, 1999, **110**, 8543.

55. W. B. Chapman, A. Schiffman, J. M. Hutson and D. J. Nesbitt, *Journal of Chemical Physics*, 1996, **105**, 3497.

56. B. H. Yang and P. C. Stancil, *European Physical Journal D*, 2008, **49**, 317.

57. O. Tkáč, A. J. Orr-Ewing, P. J. Dagdigian, M. H. Alexander, J. Onvlee and A. van der Avoird, *Journal of Chemical Physics*, 2014, **140**.

58. M. Kirste, X. A. Wang, H. C. Schewe, G. Meijer, K. P. Liu, A. van der Avoird, L. M. C. Janssen, K. B. Gubbels, G. C. Groenenboom and S. Y. T. van de Meerakker, *Science*, 2012, **338**, 1060.

59. E. A. Wade, K. T. Lorenz, J. L. Springfield and D. W. Chandler, *Journal of Physical Chemistry A*, 2003, **107**, 4976.

60. G. Sarma, C. H. Yang, A. K. Saha, D. H. Parker and L. Wiesenfeld, *Journal of Chemical Physics*, 2013, **138**, 9.

61. C. H. Yang, G. Sarma, D. H. Parker, J. J. ter Meulen and L. Wiesenfeld, *Journal of Chemical Physics*, 2011, **134**, 12.

62. O. Tkáč, Q. L. Ma, C. A. Rusher, S. J. Greaves, A. J. Orr-Ewing and P. J. Dagdigian, *Journal of Chemical Physics*, 2014, **140**.

63. O. Tkáč, A. K. Saha, J. Onvlee, C. H. Yang, G. Sarma, C. K. Bishwakarma, S. Y. T. van de Meerakker, A. van der Avoird, D. H. Parker and A. J. Orr-Ewing, *Physical Chemistry Chemical Physics*, 2014, **16**, 477.

64. H. Meyer, *Journal of Physical Chemistry*, 1995, **99**, 1101.

65. H. Meyer, U. Buck, R. Schinke and G. H. F. Diercksen, *Journal of Chemical Physics*, 1986, **84**, 4976.

66. O. Tkáč, A. K. Saha, J. Loreau, D. H. Parker, A. van der Avoird and A. J. Orr-Ewing, *Journal of Physical Chemistry A*, 2015, **119**, 5979.

67. J. Millan, N. Halberstadt, G. van der Sanden and A. van der Avoird, *Journal of Chemical Physics*, 1997, **106**, 9141.

68. H. Meyer, *Journal of Chemical Physics*, 1994, **101**, 6686.

69. H. Meyer, *Journal of Chemical Physics*, 1994, **101**, 6697.

70. J. J. Kay, S. Y. T. van de Meerakker, E. A. Wade, K. E. Strecker and D. W. Chandler, *Journal of Physical Chemistry A*, 2009, **113**, 14800.

71. G. C. M. W. van der Sanden, P. E. S.van der Avoird, A., *Journal of Chemical Physics*, 1996, **105**, 3079.

72. O. Tkáč, *PhD Thesis; Inelastic Scattering of Symmetric Top Molecules*, University of Bristol, 2013.

73. O. Tkáč, A. K. Saha, J. Loreau, Q. Ma, P. J. Dagdigian, D. H. Parker, A. van der Avoird and A. J. Orr-Ewing, *Molecular Physics*, 2015, **113**, 3925.

74. J. Loreau and A. van der Avoird, *Journal of Chemical Physics*, 2015, **143**.

75. M. H. M. Janssen, J. W. G. Mastenbroek and S. Stolte, *Journal of Physical Chemistry A*, 1997, **101**, 7605.

76. M. Kirste, X. Wang, H. C. Schewe, G. Meijer, K. Liu, A. van der Avoird, L. M. C. Janssen, K. B. Gubbels, G. C. Groenenboom and S. Y. T. van de Meerakker, *Science*, 2012, **338**, 1060.

77. O. Tkáč, Q. Ma, M. Stei, A. J. Orr-Ewing and P. J. Dagdigian, *Journal of Chemical Physics*, 2015, **142**.

78. O. Tkáč, A. G. Sage, S. J. Greaves, A. J. Orr-Ewing, P. J. Dagdigian, Q. L. Ma and M. H. Alexander, *Chemical Science*, 2013, **4**, 4199.

79. F. Qi, L. S. Sheng, Y. W. Zhang, S. Q. Yu and W. K. Li, *Chemical Physics Letters*, 1995, **234**, 450.

80. M. N. R. Ashfold, R. N. Dixon, R. J. Stickland and C. M. Western, *Chemical Physics Letters*, 1987, **138**, 201.

81. J. M. Hollas, *Modern spectroscopy*, J. Wiley, Chichester, 1996.

82. M. N. R. Ashfold, R. N. Dixon, N. Little, R. J. Stickland and C. M. Western, *Journal of Chemical Physics*, 1988, **89**, 1754.

83. G. Herzberg, J. W. T. Spinks and K.-P. Huber, *Molecular spectra and molecular structure, Vol.4, Constants of diatomic molecules ;* Van Nostrand Reinhold, New York, 1979.

84. G. Herzberg and J. W. T. Spinks, *Molecular spectra and molecular structure, Vol.3, Electronic spectra and electronic structure of polyatomic molecules*, Van Nostrand Reinhold, New York, 1966.

85. F. Lattanzi, C. Di Lauro, V. M. Horneman, M. Herman and J. Vander Auwera, *Molecular Physics*, 2007, **105**, 733.

86. Neopentane Rotational Constant, http://cccbdb.nist.gov/rotcalc2.asp, 2016

87. C. Leonard, S. Carter and N. C. Handy, *Chemical Physics Letters*, 2003, **370**, 360.

88. M. N. R. Ashfold, S. R. Langford, R. A. Morgan, A. J. Orr-Ewing, C. M. Western, C. R. Scheper and C. A. de Lange, *European Physical Journal D*, 1998, **4**, 189.

89. A. Faure, P. Hily-Blant, R. Le Gal, C. Rist and G. P. des Forets, *Astrophysical Journal Letters*, 2013, **770**, 5.

90. P. T. P. Ho and C. H. Townes, *Annual Review of Astronomy and Astrophysics*, 1983, **21**, 239.

91. C. M. Western, *PGOPHER, A Program for Simulating Rotational, Vibrational and Electronic Spectra*, University of Bristol, http://pgopher.chm.bris.ac.uk.

92. B. H. Yang and P. C. Stancil, *European Physical Journal D*, 2008, **47**, 351.

93. A. Bondi, *Journal of Physical Chemistry*, 1964, **68**, 441.

94. A. Eppink and D. H. Parker, *Journal of Chemical Physics*, 1998, **109**, 4758.

95. C. J. Eyles, *D.Phil Thesis; An Experimental and Theoretical Study of the Dynamics of Atom-Molecule Scattering*, University of Oxford, 2010.

96. S. Maret, A. Faure, E. Scifoni and L. Wiesenfeld, *Monthly Notices of the Royal Astronomical Society*, 2009, **399**, 425.

97. H. Kohguchi, T. Suzuki and M. H. Alexander, *Science*, 2001, **294**, 832.

98. J. Loreau, J. Lievin, Y. Scribano and A. van der Avoird, *Journal of Chemical Physics*, 2014, **141**, 10.

99. G. C. M. van der Sanden, P. E. S. Wormer, A. van der Avoird, J. Schleipen and J. J. ter Meulen, *Journal of Chemical Physics*, 1995, **103**, 10001.

100. J. Lequeux and SpringerLink (Online service), *The Interstellar Medium*, Springer Berlin Heidelberg, Berlin, Heidelberg, 2005.

101. D. R. Flower, *Molecular collisions in the interstellar medium*, Cambridge University Press, Cambridge, 1990.

102. U. Machin and E. Roueff, *Journal of Physics B-Atomic Molecular and Optical Physics*, 2005, **38**, 1519.

103. K. B. Gubbels, S. Y. T. van de Meerakker, G. C. Groenenboom, G. Meijer and A. van der Avoird, *Journal of Chemical Physics*, 2012, **136**.

104. M. Hernandez Vera, Y. Kalugina, O. Denis-Alpizar, T. Stoecklin and F. Lique, *Journal of Chemical Physics*, 2014, **140**.

105. J. Schleipen, J. J. Ter Meulen and A. R. Offer, *Chemical Physics*, 1993, **171**, 347.

106. D. R. Willey, R. E. Timlin, J. M. Merlin, M. M. Sowa and D. M. Wesolek, *Astrophysical Journal Supplement Series*, 2002, **139**, 191.

107. D. R. Willey, R. E. Timlin, M. Deramo, P. L. Pondillo, D. M. Wesolek and R. W. Wig, *Journal of Chemical Physics*, 2000, **113**, 611.

108. M. Mladenovic, M. Lewerenz, G. Cilpa, P. Rosmus and G. Chambaud, *Chemical Physics*, 2008, **346**, 237.

109. M. P. Hodges and R. J. Wheatley, *Journal of Chemical Physics*, 2001, **114**, 8836.

110. W. Demtröder, *Atoms, molecules and photons : an introduction to atomic-, molecular- and quantum-physics*, Springer, Heidelberg ; London, 2010.

111. K. P. Liu, *Journal of Chemical Physics*, 2006, **125**, 12.

112. X. M. Yang, in *Annual Review of Physical Chemistry*, Annual Reviews, 2007, **58**, 433.

113. S. J. Greaves, R. A. Rose and A. J. Orr-Ewing, *Physical Chemistry Chemical Physics*, 2010, **12**, 9129.

114. C. Vallance, *Philosophical Transactions of the Royal Society of London Series a-Mathematical Physical and Engineering Sciences*, 2004, **362**, 2591.

115. T. J. Preston, G. T. Dunning, A. J. Orr-Ewing and S. A. Vazquez, *Journal of Physical Chemistry A*, 2014, **118**, 5595.

116. H. L. Pan, J. Y. Yang, F. Y. Wang and K. P. Liu, *Journal of Physical Chemistry Letters*, 2014, **5**, 3878.

117. H. Kawamata and K. P. Liu, *Journal of Chemical Physics*, 2010, **133**.

118. B. Retail, J. K. Pearce, S. J. Greaves, R. A. Rose and A. J. Orr-Ewing, *Journal of Chemical Physics*, 2008, **128**, 8.

119. S. J. Greaves, A. J. Orr-Ewing and D. Troya, *Journal of Physical Chemistry A*, 2008, **112**, 9387.

120. Y. T. Wu and K. Liu, *Journal of Chemical Physics*, 2008, **129**, 10.

121. S. J. Greaves, J. Kim, A. J. Orr-Ewing and D. Troya, *Chemical Physics Letters*, 2007, **441**, 171.

122. M. J. Bass, M. Brouard, C. Vallance, T. N. Kitsopoulos, P. C. Samartzis and R. L. Toomes, *Journal of Chemical Physics*, 2003, **119**, 7168.

123. S. A. Kandel, T. P. Rakitzis, T. LevOn and R. N. Zare, *Journal of Chemical Physics*, 1996, **105**, 7550.

124. R. A. Rose, S. J. Greaves and A. J. Orr-Ewing, *Journal of Chemical Physics*, 2010, **132**.

125. B. J. Finlayson-Pitts, *Physical Chemistry Chemical Physics*, 2009, **11**, 7760.

126. S. G. Moussa, T. M. McIntire, M. Szori, M. Roeselova, D. J. Tobias, R. L. Grimm, J. C. Hemminger and B. J. Finlayson-Pitts, *Journal of Physical Chemistry A*, 2009, **113**, 2060.

127. D. J. Nesbitt, J. W. Nibler, A. Schiffman, W. B. Chapman and J. M. Hutson, *Journal of Chemical Physics*, 1993, **98**, 9513.

128. K. L. King, G. Paterson, G. E. Rossi, M. Iljina, R. E. Westacott, M. L. Costen and K. G. McKendrick, *Physical Chemistry Chemical Physics*, 2013, **15**, 12852.

129. C. Waring, K. L. King, M. L. Costen and K. G. McKendrick, *Journal of Physical Chemistry A*, 2011, **115**, 7210.

130. C. Waring, P. A. J. Bagot, J. M. Slattery, M. L. Costen and K. G. McKendrick, *Journal of Physical Chemistry A*, 2010, **114**, 4896.

131. M. E. Saecker and G. M. Nathanson, *Journal of Chemical Physics*, 1993, **99**, 7056.

132. L. M. Sverdlov, *Vibrational spectra of polyatomic molecules*, Wiley ; Jerusalem ; London : Israel Program for Scientific Translations, New York ; Toronto, 1974.

133. S. J. Greaves, E. Wrede, N. T. Goldberg, J. Y. Zhang, D. J. Miller and R. N. Zare, *Nature*, 2008, **454**, 88.

134. X. Shan and D. C. Clary, *Journal of Physical Chemistry A*, 2014, **118**, 10134.

135. K. B. Gubbels, Q. L. Ma, M. H. Alexander, P. J. Dagdigian, D. Tanis, G. C. Groenenboom, A. van der Avoird and S. Y. T. van de Meerakker, *Journal of Chemical Physics*, 2012, **136**, 13.

136. P. Coulter, M. P. Grubb, D. Koyama, I. V. Sazanovich, G. M. Greetham and A. J. Orr-Ewing, *Journal of Physical Chemistry A*, 2015, **119**, 12911.

137. D. R. Glowacki, A. J. Orr-Ewing and J. N. Harvey, *Journal of Chemical Physics*, 2011, **134**, 11.

138. D. R. Glowacki, R. A. Rose, S. J. Greaves, A. J. Orr-Ewing and J. N. Harvey, *Nature Chemistry*, 2011, **3**, 850.